

1 **Crust and uppermost mantle beneath the North China Craton, northeastern China, and**
2 **the Sea of Japan from ambient noise tomography**

3 Yong Zheng¹, Weisen Shen², Longquan Zhou⁴, Yingjie Yang^{1,3}, Zujun Xie¹, and Michael H. Ritzwoller²

- 4 1. State Key Laboratory of Geodesy and Earth's Dynamics, Institute of Geodesy and Geophysics, Chinese Academy of
5 Sciences, Wuhan, Hubei, 430077, China (zhengyong@whigg.ac.cn)
- 6 2. Center for Imaging the Earth's Interior, Department of Physics, University of Colorado at Boulder, Boulder, CO
7 80309-0390 (michael.ritzwoller@colorado.edu)
- 8 3. Department of Earth and Planetary Sciences, Macquarie University, 2109 Sydney, Australia (yingjie.yang@mq.edu.au)
- 9 4. China Earthquake Network Center, Beijing, 100045, China (lqzhou@seis.ac.cn)

10 **Abstract:**

11 A 3-D shear velocity model of the crust and uppermost mantle to a depth of 100 km is presented
12 beneath the North China Craton (NCC), northeastern China, the Korean Peninsula, and the Sea
13 of Japan. Ambient noise Rayleigh wave tomography is applied to data from more than 300
14 broad-band seismic stations from Chinese provincial networks (CEArray), the Japanese F-Net,
15 and the IRIS Global Seismic Network. Continuous data from 2007 to 2009 are used to produce
16 group and phase velocity maps from 8 sec to 45 sec period. The model is motivated to constrain
17 the distributed intra-plate volcanism, crustal extension, cratonic rejuvenation, and lithospheric
18 thinning that are hypothesized for the study region. Numerous robust features are observed that

19 impose new constraints on the geometry of these processes, but discussion concentrates only on
20 four. (1) The North-South Gravity Lineament follows the ~40 km contour in crustal thickness,
21 and crustal thickness is anti-correlated with water depth beneath the Sea of Japan, consistent with
22 crustal isostasy for a crust with laterally variable composition. (2) The lithosphere is thin (~70
23 km) beneath the Songliao-Bohai Graben, but seismically fast. (3) Even thinner more attenuated
24 lithosphere bounds three sides of the eastern NCC (in a horseshoe shape), identifying a region of
25 particularly intense tectonothermal modification where lithospheric rejuvenation may have
26 reached nearly to the base of the crust. (4) Low velocity anomalies reach upward (in a Y-shape)
27 in the mantle beneath the eastern and western borders of the Sea of Japan, extending well into
28 continental East Asia in the west, and are separated by a ~60 km thick lithosphere beneath the
29 central Sea of Japan. This anomaly may reflect relatively shallow slab dehydration in the east
30 and in the west deeper dehydration and convective circulation in the mantle wedge overlying the
31 stagnant slab.

32 **Keywords** Ambient noise, surface waves, Sea of Japan, North China Craton, Kyushu microseism

33

34

35

36

37

38 **1. Introduction**

39 The goal of this study and companion papers by *Yang et al.* [2010, 2011], *Zheng et al.*
40 [2010b], and *Zhou et al.* [2011] is to advance toward an integrated, highly resolved shear
41 velocity (V_s) model of the crust and uppermost mantle beneath China. *Zhou et al.* [2011] focus
42 on Southeast China and *Yang et al.* [2010, 2011] and *Zheng et al.* [2010b] on western China and
43 Tibet. The complementary focus of the current paper is the Sino-Korean Craton, northeastern
44 China, the Korean Peninsula, and the Sea of Japan. More than 320 seismic stations from Chinese
45 provincial networks in northeastern China and surrounding areas, Japanese F-Net stations
46 [Okada et al., 2004], and IRIS GSN stations are the basis for this study (Fig. 1). The resulting
47 station and path coverage that emerges is unprecedented in this region. In order to place strong
48 constraints on crustal structure, ambient noise tomography is employed. As described below,
49 ambient noise tomography has already been applied in other regions of China (e.g., Tibet), at
50 larger scales (e.g., across all of China) at a lower resolution, or in a part of the study region (e.g.,
51 North China Platform, Korean peninsula), but a resulting integrated, high-resolution model of the
52 crust and uppermost mantle of the entire region of study has never before been constructed. Such
53 a model is desired to illuminate a set of interconnected tectonic problems that make the
54 Sino-Korean Craton, northeastern China, and the Sea of Japan a particularly fertile area for
55 seismic tomography.

56 Northeastern China is composed of a mosaic of tectonic blocks and lineated orogenic belts

57 (Fig. 2) that have been arranged and modified by a long, complex, and in some cases enigmatic
58 history of subduction, accretion, and collision dating back to the Archean [e.g., *Sengor and*
59 *Natal'in*, 1996; *Yin and Nie*, 1996; *Yin*, 2010]. In the south, the Sino-Korean Craton (SKC),
60 delineated by solid red lines in Figure 2, is separated from the Yangtze Craton to the south by the
61 Qinling-Dabie-Sulu orogenic belt [*Yin and Nie*, 1993]. The SKC itself consists of the Ordos
62 Block, the North China Platform, Bohai Bay, the Korean Peninsula, as well as marginal and
63 intruding mountain ranges. The Chinese part of the SKC is usually referred to as the North
64 China Craton (NCC) and is divided here into western, central, and eastern parts delineated by
65 dashed red lines. North of the SKC, the Xing'an-East Mongolia block is separated from the
66 Songliao-Bohai graben by the North-South Gravity Lineament (NSGL). The NSGL extends
67 southward into the SKC near the boundary between the central and eastern parts of the North
68 China Craton. The Songliao-Bohai graben, stretching from the Songliao Basin to the Bohai Gulf,
69 is flanked to the east by the Tancheng-Lujiang (Tanlu) Fault that extends into the SKC and forms
70 the eastern boundary of the North China Craton. The Tanlu Fault also defines the western border
71 of the Northeast Asia Foldbelt [e.g., *Sengor and Natal'in*, 1996; *Yin and Nie*, 1996].

72 Much of northeastern China has undergone extensive tectonism during the late Mesozoic and
73 Cenozoic eras [e.g., *Yin*, 2010]. Northeastern China, bounded by the SKC to the south and the
74 Sea of Japan back-arc basin to the east, is part of eastern China's Cenozoic volcanic zone [e.g.,
75 *Ren et al.*, 2002]. Episodic volcanism has been particularly prominent along three volcanic

76 mountain chains: Great Xing'an Range (GXAR), Lesser Xing'an Range (LXAR), Changbai
77 Mountains (CBM). Rifting and extension are believed to have begun in the late Mesozoic [*Tian*
78 *et al.*, 1992] and have led to the development of the Songliao Basin, although the Songliao
79 basement is traced back to the Archean [*Rogers and Santosh*, 2006]. It has also been
80 hypothesized that there is a physical linkage between the sequential openings of the Songliao
81 graben [e.g., *Liu et al.*, 2001] and the Sea of Japan [*Tatsumi et al.*, 1989; *Jolivet et al.*, 1994]. The
82 SKC formed largely in the Archean, but it is a paradigm of an Archean craton that has lost its
83 lithospheric keel. Petrological and geochemical evidence [e.g., *Menzies et al.*, 1993; *Griffin et al.*,
84 1998] suggests that typical cratonic lithosphere existed beneath the entire SKC until at least the
85 Ordovician, after which the SKC was reactivated and lithospheric thinning occurred at the
86 minimum beneath the eastern part of the NCC.

87 The physical mechanisms that have produced the highly distributed volcanism, crustal
88 extension, cratonic rejuvenation and lithospheric thinning that have occurred across parts of
89 northeastern China remain poorly understood [e.g., *Deng et al.*, 2007; *Chen*, 2010]. These issues
90 can be illuminated with seismic images of velocity heterogeneities, internal discontinuities, and
91 crustal and mantle anisotropy, yet the vast majority of the studies to date have been geochemical
92 or petrological in nature. Increasingly, seismological studies are adding new information due in
93 part to the rapid expansion of seismic instrumentation in China over the past few years [e.g.,
94 *Zheng et al.*, 2010a]. These studies include body wave tomography of the mantle [e.g., *Lebedev*

95 *and Nolet, 2003; Huang and Zhao, 2006; Zhao, 2009; Tian et al., 2009; Xu and Zhao, 2009; Li*
96 *and van der Hilst, 2010; Santosh et al., 2010]* and of the crust [e.g., *Sun and Toksoz, 2006*]. Pn
97 tomography [*Li et al., 2011*], receiver functions analyses [*Zheng et al., 2006; Chen et al., 2009*],
98 and shear wave splitting studies have also been performed [*Zhao et al., 2008; Bai et al., 2010; Li*
99 *and Niu, 2010*]. Recent body wave results have focused mainly on the eastern part of the NCC,
100 including efforts to image its thin intact lithosphere as well as the potential remnants of the
101 delaminated lithosphere near 400 km depth [e.g., *Chen et al., 2009; Xu and Zhao, 2009*].

102 At least parts of northeast China have been imaged by larger scale teleseismic surface wave
103 dispersion studies [e.g., *Ritzwoller and Levshin, 1998; Ritzwoller et al., 1998; Villaseñor et al.,*
104 *2001; Yanovskaya and Kozhevnikov, 2003; Huang et al., 2003, 2004; Priestley et al., 2006*].
105 Recent regional scale teleseismic surface wave studies have also been conducted within North
106 China [e.g., *Tang and Chen, 2008; Huang et al., 2009; Zhou et al., 2009; He et al., 2009; Pan et*
107 *al., 2011*], in adjacent regions [e.g., *Yao et al., 2006, 2008*], and in the Sea of Japan [e.g.,
108 *Bourova et al., 2010; Yoshizawa et al., 2010*]. Some of these studies are discussed further in the
109 context of our 3D model in section 6.

110 Within the last few years a new method of surface wave tomography has emerged based on
111 using ambient seismic noise to extract surface wave empirical Green's functions (EGFs) and to
112 infer Rayleigh [e.g., *Sabra et al., 2005; Shapiro et al., 2005*] and Love wave [e.g., *Lin et al.,*
113 *2008*] group and phase speeds in continental areas. Compared with traditional earthquake

114 tomography methods, ambient noise tomography is relatively free of artifacts related to the
115 distribution of earthquakes as well as errors in earthquake locations and source mechanisms. The
116 dominant frequency band for ambient noise tomography lies between about 8 and 40 sec period.
117 Rayleigh waves in this band are sensitive to crustal and uppermost mantle structures. Ambient
118 noise tomography has produced phase and group velocity maps in various regions around the
119 world [e.g., *Moschetti et al.*, 2007; *Yang et al.*, 2007; *Villasenor et al.*, 2007; *Bensen et al.*, 2008]
120 and also is the basis for 3-D crustal and uppermost mantle models of isotropic shear velocity
121 structure [e.g., *Yang et al.*, 2008a, 2008b; *Bensen et al.*, 2009; *Moschetti et al.*, 2010b], radial
122 anisotropy [e.g., *Moschetti et al.*, 2010a], and azimuthal anisotropy [e.g., *Lin et al.*, 2011].
123 Ambient noise in east Asia has been shown to be sufficiently well distributed in azimuthal
124 content to be used for surface wave dispersion measurements [e.g., *Yang and Ritzwoller*, 2008]
125 and studies based on ambient noise have been conducted at large scales across all of China
126 [*Zheng et al.*, 2008; *Sun et al.*, 2010], in regions adjacent to northeastern China [e.g., *Yao et al.*,
127 2006, 2008; *Guo et al.*, 2009; *Li et al.*, 2009; *Huang et al.*, 2010; *Yang et al.*, 2010; *Zheng et al.*,
128 2010b; *Zhou et al.*, 2011], within the North China Craton [*Fang et al.*, 2010], on the Korean
129 Peninsula [*Kang and Shin*, 2006; *Cho et al.*, 2007], and in Japan [e.g., *Nishida et al.*, 2008].

130 Ambient noise tomography in northeastern China, the Korean Peninsula, the Sea of Japan,
131 however, is faced with an uncommon technical challenge – the existence of a persistent localized
132 microseismic source on Kyushu Island [*Zeng and Ni*, 2010] in the period band between about 8

133 and 14 sec, which has been explained to be caused by long period volcanic tremors beneath Aso
134 Volcano in the center of Kyushu [*Kawakatsu et al.*, 2011; *Zeng and Ni*, 2011]. This signal causes
135 a significant disturbance that is observable on cross-correlations of ambient noise, which, if left
136 uncorrected, would bias measurements of group and phase velocity in this period band of
137 considerable sensitivity to crustal structure. A principal focus of this paper, therefore, is to
138 identify this disturbance and minimize its effects on the estimated Rayleigh wave group and
139 phase velocity dispersion maps.

140 The present paper is based on Rayleigh wave group and phase velocity maps from 8 to 45 sec
141 period across the Sino-Korea Craton, northeastern China, Korea, and the Sea of Japan. Based on
142 these maps, a 3-D model of the crust and uppermost mantle is constructed by Monte-Carlo
143 inversion along with associated uncertainties. The resulting information complements existing
144 and emerging teleseismic body wave and surface studies by presenting new and much stronger
145 constraints on the structure of the crust and uppermost mantle. The data processing and quality
146 control procedures are described in section 2 and methods used to de-sensitize the data to
147 degradation caused by the persistent, localized Kyushu microseism are presented in section 3.
148 The Rayleigh wave group and phase velocity maps are described in section 4. Section 5 presents
149 a brief discussion of the Monte-Carlo inversion method. Section 6 describes the features of the
150 resulting model. In addition, there is a discussion of several key findings including the relation
151 between sea floor depth and crustal thickness beneath the Sea of Japan, the horseshoe-shape (in

152 map view) of the thinnest lithosphere that bounds the NCC, and the Y-shaped asthenosphere (on
153 vertical profiles) observed beneath the Sea of Japan and the Northeast Asian Foldbelt.

154 **2. Data Processing and Quality Control**

155 The data used in this study are continuous seismic waveforms recorded at broadband stations
156 that existed in and around northeast China and the Sea of Japan from August 2007 to July 2009.
157 Networks providing data include: (1) Chinese Provincial Networks in northeast China consisting
158 of 232 broadband seismic stations (referred to here as CEArray), (2) F-Net in Japan comprising
159 69 long period seismic stations, and (3) the IRIS GSN broadband network in northeast Asia
160 consisting of 22 stations. In total, two years of continuous waveform data have been acquired
161 that were recorded at the 323 stations denoted by solid triangles and squares in **Figure 1**. Only
162 vertical component data are processed, meaning only Rayleigh waves are studied.

163 The data processing procedures follow those of *Bensen et al.* [2007] and *Lin et al.* [2008].
164 After removing the instrument responses, all records are bandpass filtered between 5 and 150 sec
165 period. We apply both temporal normalization and spectral whitening. Temporal normalization is
166 applied in an 80 second moving window. Cross-correlations are performed daily between all
167 pairs of stations and then are stacked over the two-year time window. **Figure 3** presents example
168 cross-correlation record sections among Chinese stations, among F-Net stations, and inter-station
169 pairs between F-Net stations and Chinese stations.

170 Data quality control is discussed here and in section 3 and consists of five principal steps,
171 denoted A-E. Most of these steps are based on procedures summarized by *Bensen et al.* [2007]
172 and *Lin et al.* [2008], but because of the mixture of instrument types used in this study and the
173 existence of the Kyushu microseism we add extra steps to ensure the reliability of the resulting
174 dispersion measurements. Step A. A dispersion measurement is retained for a cross-correlation at
175 a given period only if signal-to-noise ratio (SNR) > 15 at that period, where SNR is defined by
176 *Bensen et al.* [2007]. Step B. We remove the effects of the Kyushu microseism, which we discuss
177 further in section 3. Step C. We retain an observation at a given period only if both the group and
178 phase velocities are measured by the automated frequency-time analysis method [*Bensen et al.*,
179 2007]. Group and phase velocity are separate measurements and are not constrained to agree
180 even though they are related theoretically [e.g., *Levshin et al.*, 1999]. Step D. We identify and
181 discard stations with bad instrument responses. Step E. This step is broken into two parts. First,
182 we only accept dispersion measurements with path lengths ≥ 3 wavelengths. Second, a
183 measurement is retained only if the misfit determined from the final dispersion map is less than
184 12 sec for group travel time and less than 5 sec for phase travel time, which is somewhat more
185 than twice the standard deviation of the final misfit. Group and phase velocity dispersion
186 measurements of Rayleigh waves are obtained on the symmetric component of inter-station
187 cross-correlations except for paths identified as affected by the Kyushu microseism, as discussed
188 further in section 3.

189 Because the seismic instruments used in this study differ in origin between China, Japan, and
190 the US, and instruments can vary within CEArray between provinces in China, it is important to
191 identify errors and inconsistencies in response files. For the IRIS network data, F-Net data and
192 most of the Chinese stations, full response (RESP) files including both analog and digital filter
193 stages are available. For a small number of Chinese stations we possess only pole-zero response
194 files missing the digital filtering stages. We find that for the CEArray instruments, the analog
195 pole-zero responses sometimes differ from the full responses computed from the RESP files for
196 stations that have both types of response files. Therefore, we discard the Chinese stations for
197 which we have not been able to acquire RESP files. This affected 36 stations, none of which are
198 included in the 232 Chinese stations shown in [Figure 1](#). Using these response files, all data are
199 converted to velocity prior to cross-correlation.

200 Two other procedures are applied to find other instrument response errors. First, we identify
201 polarity errors (π phase shift) that may represent a units error in the instrument by comparing
202 P-wave first motions observed across the array following deep, distant teleseisms. We also look
203 for half-period misfits based on the final tomography maps at each period. These procedures
204 identified seven stations with polarity errors that are discarded. Second, we compare the phase
205 and group times measured on the positive and negative lags of all cross-correlations, which
206 identifies timing errors as long as both lags have a high SNR [*Lin et al.*, 2007]. These procedures
207 identified and discarded three Chinese stations.

208 The 2π phase ambiguity inherent in phase velocity measurements is resolved iteratively, first
209 based on phase velocities predicted by the 3D model of *Shapiro et al.* [2002] and then later on
210 with increasingly refined phase velocity maps that are determined in this study.

211 With more than 300 stations, in principal about 50,000 inter-station cross-correlations could
212 be obtained. Quality control procedures reduce this number appreciably as **Table 1** illustrates.
213 After applying the selection criteria, we obtain between about 10,000 to 30,000 group and phase
214 velocity measurements for tomography at periods ranging from 10 to 45 sec, although the
215 number of paths drops sharply below 10 sec period.

216 **3. The Effect of the Localized Persistent Kyushu Microseism**

217 In northeast China, a strong disturbance appears on the cross-correlation waveforms. The
218 record sections shown in **Figures 3b and 3c** show this disturbance, which appears as precursory
219 signals (identified by white dots) in addition to the expected surface wave part of the empirical
220 Green's function. Another example is presented in **Figure 4a**, where the disturbance appears at
221 positive correlation lag between 100 and 150 sec, whereas the desired Rayleigh wave signal
222 arrives much later and is seen clearly only on the negative correlation lag. The arrival of these
223 disturbances near to the Rayleigh wave wavepackets interferes with the ability to measure
224 Rayleigh wave speeds accurately. In fact, the effect tends to bias Rayleigh waves fast,
225 particularly for Rayleigh wave group velocities.

226 These precursory signals are due to the persistent, localized Kyushu microseism that has been
227 identified and located by *Zeng and Ni* [2010] on the island of Kyushu, Japan, within our study
228 region. *Kawakatsu et al.* [2011] explain the signal as having originated from long period volcanic
229 tremor beneath Aso Volcano on Kyushu Island. The period band of this microseism is
230 dominantly between 8 and 14 sec, and it is somewhat reminiscent of the longer period persistent
231 26 sec microseism located in the Gulf of Guinea [e.g., *Shapiro et al.*, 2006]. We are interested in
232 minimizing its interference with surface wave dispersion measurements across the study region.
233 To do so, we have re-located it, confirming the location of *Zeng and Ni* [2010], and have
234 developed a data processing procedure that allows reliable dispersion curves to be obtained
235 across the Sino-Korean Craton, northeastern China, the Korean peninsula, and the Sea of Japan.
236 The effect of the procedure, however, is to reduce the number of measurements in the region
237 broadly surrounding Kyushu at periods between 10 and 18 sec.

238 **3.1 Re-location of the Kyushu microseism**

239 We use the envelope functions between periods of 10 and 12 sec for the Kyushu signal
240 observed on inter-station cross-correlations to locate the Kyushu microseism. An example
241 envelope function is shown in the bottom panel of **Figure 4a**. Based on an initial observed group
242 velocity map at 11 sec period, we predict the theoretical arrival time of the Kyushu signal for
243 each inter-station pair for each hypothetical source location on a broad map of the region. We
244 then take the observed amplitude of the envelope function at the predicted time and plot it at the

245 hypothetical source location. An example is shown in [Figure 4b](#), where the hyperbola identifies
246 the set of possible locations for the Kyushu microseism for a particular inter-station pair. We
247 refer to this figure as the migrated envelope function. Finally, we stack over all migrated
248 envelope functions for cross-correlations involving the GSN stations INCN (Inchon, South
249 Korea) and SSE (Shanghai, China), with the paths shown in [Figure 4c](#). The resulting stack of
250 migrated envelope functions is shown in [Figure 4d](#), demonstrating that the re-location of the
251 Kyushu microseism is close to the location from *Zeng and Ni* [2010] ([Fig. 4d](#)) on Kyushu Island.

252 **3.2 Eliminating the effect of the Kyushu microseism**

253 Assuming that the Kyushu microseism is a point source, for each inter-station
254 cross-correlation we calculate the expected arrival time of the Kyushu signal as well as the
255 theoretical arrival time of the Rayleigh wave between the two-stations. The relative arrival times
256 of the Kyushu signal (white dots in [Fig. 3](#)) and the inter-station Rayleigh waves are highly
257 variable but systematic. When the arrival times of the Kyushu signals are close to the desired
258 surface waves it becomes difficult to separate the signals between 8 and 14 sec period on the
259 symmetric component of the cross-correlations. However, the systematics of the relative arrival
260 times can be exploited to separate the two waves and obtain reliable Rayleigh wave group and
261 phase velocity measurements for most paths by focusing on a single correlation lag. [Figure 5](#)
262 illustrates this point by showing how the Kyushu signal biases group and phase velocity
263 measurements when the Rayleigh wave and the Kyushu signal arrive nearly simultaneously on

264 the negative lag component of the cross-correlation (Fig. 5a). Figure 5b shows the symmetric
265 component of the cross-correlation. Figure 5c is the positive component of the cross-correlation,
266 which is free from the Kyushu disturbance. On frequency-time diagrams [e.g., Ritzwoller and
267 Levshin, 1998], large differences between positive and negative correlation lag times are
268 observed at periods shorter than 18 sec, especially in the group velocity dispersion curves. This is
269 illustrated by Figure 5d,e, in which the Kyushu signal disturbs the dispersion curve in Figure 5d
270 but not Figure 5e. The Kyushu signal causes the measured group velocity to bias towards higher
271 velocities (Fig. 5f). At periods longer than 18 sec, however, differences are quite small.

272 Therefore, to separate the desired inter-station Rayleigh wave from the Kyushu signal we
273 must measure the Rayleigh wave dispersion on the correlation lag opposite from the arrival of
274 the Kyushu signal in the period band of disturbance. The symmetric component, the average of
275 the cross-correlation at positive and negative lag, cannot be used if the Kyushu signal arrives
276 near the inter-station Rayleigh wave at either positive or negative correlation lag time.

277 In practice, we take the following steps. At periods greater than 18 sec, we ignore the Kyushu
278 disturbance and use the symmetric component for dispersion measurement. At periods less than
279 or equal to 18 sec, the relative arrival time of the Kyushu signal and the surface wave signal at 12
280 sec period guides the measurement. If the expected apparent speed of the Kyushu signal is
281 greater than 4.5 km/s and the length of the inter-station path is longer than three wavelengths,
282 then the Kyushu signal is well enough separated from the surface wave that phase and group

283 velocities can be measured on the symmetric component. If the expected apparent speed of the
284 Kyushu signal is less than 4.5 km/s, then we make group and phase velocity measurements on
285 the correlation lag opposite from the Kyushu signal.

286 As [Figure 5a](#) exemplifies, the correlation lag on the opposite side of the Kyushu signal may
287 have a smaller amplitude than the lag containing the Kyushu signal and will have a significantly
288 lower SNR than the symmetric component. Thus, this data processing procedure tends to lower
289 the SNR for many inter-station cross-correlations between 8 and 16 sec period. Because
290 observations are discarded if $\text{SNR} < 15$, this reduces the data set appreciably, as [Table 1](#) shows.
291 We are still left with sufficient high quality measurements to perform tomography across much
292 of the study region, however.

293 If left untreated, the Kyushu signal would have vitiated our maps predominantly in South
294 Korea, the southern Sea of Japan, and in the Kyushu region from 8 to 14 sec period. Artifacts
295 would have been much stronger on the group velocity than the phase velocity maps. Above 16
296 sec period, however, even if left untreated, the Kyushu signal would have had only a weak effect
297 on the estimated maps.

298

299

300

301 **4. Rayleigh Wave Dispersion Maps**

302 **4.1 Construction of the dispersion maps**

303 Surface wave tomography is applied to the selected dispersion measurements to produce
304 Rayleigh wave group and phase speed maps on a $0.5^\circ \times 0.5^\circ$ grid using the ray-theoretic method
305 of *Barmin et al.* [2001]. Being mostly determined over regional (non-teleseismic) inter-station
306 distances, the dispersion measurements observed here will not be affected strongly by off-great
307 circle effects [e.g., *Lin et al.*, 2009] except for relatively long paths undergoing a continent-ocean
308 transition. This will primarily affect paths from Japanese F-Net to Chinese stations and the maps
309 of the Sea of Japan may be degraded somewhat by this effect. Finite frequency effects will also
310 be weak in the period band of study [*Lin et al.*, 2011]. The tomographic method of *Barmin et al.*
311 is based on minimizing a penalty functional composed of a linear combination of data misfit,
312 model smoothness, and model amplitude. The choice of the damping parameters is based on the
313 optimization of data misfit and the recovery of coherent model features. Due to a shortage of
314 measurements, we are unable to produce reliable maps below 8 sec period and above about 45
315 sec period. The resulting Rayleigh wave dispersion maps, therefore, are constructed between 8
316 and 45 sec on a 2 sec period grid.

317 During tomography, resolution is also estimated via the method described by *Barmin et al.*
318 [2001] with modifications presented by *Levshin et al.* [2005]. Resolution is defined as twice the

319 standard deviation of a 2-D Gaussian fit to the resolution surface at each geographic node.
320 Examples of resolution maps are plotted in [Figure 6](#) for the 16 sec and 35 sec period
321 measurements. Resolution is estimated to be about 100 km across most of the region of study but
322 degrades to 200-400 km near the boundary of our studied area where station coverage is sparse.

323 Histograms of data misfit using the dispersion maps at periods of 14 sec, 20 sec, 30 sec, and
324 40 sec are plotted in [Figure 7](#) for phase and group velocity. Group travel time misfits are
325 typically 3-4 times larger than phase travel time misfits because phase velocity measurements are
326 more accurate [*Bensen et al.* 2007; *Lin et al.*, 2008] and group velocity sensitivity kernels have a
327 larger amplitude. The range of standard deviations of the group travel time misfits runs between
328 about 4 and 5 sec and that of phase travel time between about 1 and 1.5 sec. Phase travel time
329 misfits of ~1 sec between 14 and 30 sec period are indicative of the quality of the data set, being
330 similar to misfits that result from USArray data [e.g., *Lin et al.*, 2008].

331 **4.2 Description of the dispersion maps**

332 Group and phase velocity maps at periods of 12, 20, 30, and 40 sec are plotted in [Figures 8](#)
333 and [9](#). Only those areas where the spatial resolution is better than 400 km are shown. The 100 km
334 spatial resolution contour is also plotted as a continuous white line. Because the 3-D model is
335 discussed in considerable detail in section 6, discussion of the dispersion maps here is brief but is
336 illuminated by the sensitivity kernels shown in [Figure 10](#). Both phase (solid lines) and group

337 velocity (dashed lines) kernels are shown, computed for 10 and 40 sec period at two locations in
338 the final model constructed here: (a) Sea of Japan and (b) North China Craton.

339 As **Figure 10** illustrates, at each period the group velocity measurements are sensitive to
340 shallower structures than the phase velocities. Phase velocity maps, therefore, generally should
341 be compared with somewhat shorter period group velocity maps. Thus, comparison between
342 **Figures 8 and 9** reveals that the phase velocity map at 12 sec is similar to the group velocity map
343 at 20 sec and the phase velocity map at 20 sec is quite like the group velocity pattern at 30 sec.
344 Because of the lower uncertainty in the phase velocity measurements, however, the phase
345 velocity maps generally are more accurate than the maps of group velocity.

346 The dispersion maps are sensitive to quite different structures between short and long periods
347 and between continental and oceanic regions even at the same period as **Figure 10** illustrates. The
348 short period dispersion maps (12 sec group and phase velocity in Fig. 8 and 9) are primarily
349 sensitive to upper crustal velocities in continental areas, which are dominated by the presence or
350 lack of sediments. In regions with oceanic crust, sensitivity is predominantly to uppermost
351 mantle structure. At intermediate periods (20 sec phase velocity, 20-40 sec group velocity), the
352 maps are mostly sensitive to mid- to lower-crustal velocities beneath continents and
353 continent-ocean crustal thickness variations. At long periods (30-40 sec phase velocity), the maps
354 predominantly reflect crustal thickness variations on the continent and uppermost mantle
355 conditions beneath oceans.

356 At short periods (12 sec), the dispersion maps in **Figures 8-9** exhibit low velocity anomalies
357 where sediments are present [*Bassin et al.*, 2000]; e.g., the Songliao Basin (SLB), Huabei Basin
358 (HB), Bohai Bay (BH), North China Platform (NC), the Yellow Sea (ESYS), and the Tsushima
359 Basin (TB) in the southern Sea of Japan. The younger, Cenozoic age sediments of Bohai Bay and
360 the Huabei Basin of the North China Craton are much slower than the older, largely Mesozoic
361 age sediments of the Songliao Basin. Higher velocities are imaged in the mountains surrounding
362 the basins; e.g, the Great Xing'an Range (GXAR), Lesser Xing'an Range (LXAR), the Changbai
363 Mountains (CBM), the Yinshan Mountains (YSM), and the Taihang Mountains (THM), which is
364 consistent with the presence of crystalline rocks near the surface. Weak positive anomalies are
365 observed in the Korean Peninsula.

366 At intermediate periods (20 sec phase velocity, 20-30 sec group velocity), relatively low
367 wave speeds are still observed for the deeper basins: Songliao, Huabei, Bohai Bay, and Yellow
368 Sea. Group and phase velocity are very high in the Sea of Japan reflecting oceanic mantle
369 lithospheric shear wave speeds that clearly outline the continental boundary of the oceanic crust.
370 It should be noted that off-great-circle effects that may exist are not severe enough to distort the
371 borders of the oceanic crust badly. A significant low velocity anomaly appears in Xing'an-East
372 Mongolia. The anomaly does not develop along the Tancheng-Lujiang Fault, however, but rather
373 to the west of the Songliao Basin, encompassing the Great Xing'an Range and the Yinshan
374 Mountains north of the Ordos Block. To the east of the North-South Gravity Lineament the crust

375 is much thinner than to its west [e.g., *Xu*, 2007].

376 For group velocity at 40 sec and phase velocity at periods of 30-40 sec, four principal
377 observations are worth noting. First, the high wave speed anomalies of the Sea of Japan diminish
378 from 30 sec to 40 sec period on the phase velocity maps. This reflects relatively thin lithosphere
379 beneath the Sea of Japan and increased sensitivity to the underlying asthenosphere by the longer
380 period waves. Second, the Songliao, Huabei, and Bohai basins are situated within the
381 Songliao-Bohai Graben, which is believed to have formed by back-arc extension and potential
382 rifting [*Liu et al.*, 2001]. This graben, extending from the Songliao Basin into Bohai Bay, is
383 associated with a continuous high velocity anomaly, which is clearly observable on the 30 and 40
384 sec phase velocity maps. Third, on the longest period phase velocity maps, low wave speeds are
385 found along the entire length of the Northeast Asia Foldbelt, extending into the Korean Peninsula.
386 Such clear continuous low wave speeds are not apparent on the 40 sec group velocity map
387 because of the shallower sensitivity of group velocities than phase velocities. Apparent
388 discrepancies between phase and group velocities such as this one are reconciled by the 3-D V_{sv}
389 model, as discussed in section 5. Finally, a belt of low velocities is present on the longest period
390 phase velocity maps in the far eastern Sea of Japan bordering Hokkaido and northern and central
391 Honshu, extinguishing in southern Honshu, and then re-initiating along Kyushu and the Ryukyu
392 Islands.

393

394 5. Construction of the 3-D Model

395 This study is based exclusively on Rayleigh waves, which are primarily sensitive to vertically
396 polarized shear wave speeds (V_{sv}) that may be slower than horizontally polarized wave speeds
397 (V_{sh}) in regions where anisotropic minerals are preferentially aligned in the horizontal plane.
398 The velocity difference between V_{sv} and V_{sh} is referred to as radial anisotropy. Thus, the model
399 we produce is a V_{sv} model. In the presence of substantial radial anisotropy, V_{sv} can be several
400 percent lower than the effective isotropic shear wave speed, V_s . Radial anisotropy is common in
401 both the mantle [e.g., *Ekstrom and Dziewonski, 1997; Shapiro and Ritzwoller, 2002*] and the
402 crust [e.g., *Shapiro et al., 2004; Moschetti et al., 2010a,b*], and is geographically variable. We
403 will generally refer to our 3D model as being a V_{sv} model, but for simplicity will also refer to it
404 as a shear wave speed or V_s model.

405 The 3D V_{sv} model is based on the Rayleigh wave phase and group speed maps from 8 to 45
406 sec period on a $0.5^\circ \times 0.5^\circ$ grid across the study region. Periods at which resolution is greater than
407 200 km are not included in the inversion. This determines the outline of the model and in oceanic
408 regions local dispersion curves typically begin at 12 sec period. Local dispersion curves from the
409 eight locations identified with red dots in [Figure 2](#) are shown in [Figure 11](#) with error bars. The
410 group velocity and phase velocity curves shown in [Figure 11](#) are mostly smoothly varying and
411 are able to be fit by a vertically simple V_s model at each point within observational error. In
412 particular, the group and phase velocity curves are reconcilable at each point. Local misfit is

413 presented for each point in **Figure 11**, where “RMS misfit” means the square root of the reduced
414 chi-square value:

$$415 \quad \text{RMS misfit} = \left[\frac{1}{N} \sum_i \frac{(d_i - p_i)^2}{\sigma_i^2} \right]^{\frac{1}{2}} \quad (1)$$

416 where d_i is the observed group or phase velocity value, p_i is the value predicted from the model,
417 σ_i is the uncertainty for the observation, and N is the total number of phase plus group velocity
418 values along the dispersion curves.

419 Uncertainties in phase and group velocity curves are notoriously difficult to determine
420 reliably, as they are typically underestimated by most tomographic codes based on standard error
421 propagation [e.g., Barmin et al., 2001]. They can be estimated reliably by using the eikonal
422 tomography method [Lin et al., 2009], but the method requires more uniform array spacing than
423 exists in the study region. Therefore, the uncertainties shown in **Figure 11** are not from the data
424 set presented here, but, as discussed in section 2, misfit statistics in the present study are similar
425 to those that emerge in the western US based on the regularly spaced USArray Transportable
426 Array. For this reason, we take the average uncertainties estimated by eikonal tomography using
427 USArray in the western US, but to be conservative we double them [Lin et al., 2009; Moschetti
428 et al., 2010a, 2010b].

429 The 3D model is constructed via a Monte-Carlo method that is similar to the methods of

430 *Shapiro and Ritzwoller* [2002] and *Yang et al.* [2008]. The starting model for the Monte-Carlo
431 search derives from the V_{sv} values of the global model of *Shapiro and Ritzwoller* [2002] with
432 two principal modifications. First, we simplify the starting crustal model considerably: the two
433 sedimentary layers and three crystalline crustal layers of the model of *Shapiro and Ritzwoller* are
434 averaged separately to define only two constant velocity layers (not including a possible water
435 layer). Second, crustal thickness is not allowed to be less than 20 km in the Sea of Japan, as
436 discussed in section 6.1. Uniformly distributed perturbations in V_{sv} are considered using a single
437 sedimentary layer with variable thickness and shear velocity, four B-splines for V_{sv} in the
438 crystalline crust, and five B-splines in the mantle to a depth of 150 km, below which the model is
439 a constant velocity half-space. The resulting model is vertically smooth in both the crystalline
440 crust and mantle. Moho depth is allowed to vary in a uniform interval of ± 10 km relative to the
441 starting model. V_{sv} is constrained to increase monotonically in the crystalline crust and the depth
442 derivative of velocity directly below Moho is constrained to be positive (i.e., velocity increases
443 with depth right below Moho, but can decrease deeper into the mantle). Both constraints are
444 introduced to reduce the model space, in particular the magnitude of the trade-off between Moho
445 depth with structures at depths adjacent to Moho. The positivity constraint on the depth
446 derivative of velocity in the uppermost mantle typically introduces a thin low velocity “sill” right
447 below Moho, which is an artifact of the constraint.

448 The model has no radial anisotropy, thus $V_s = V_{sh} = V_{sv}$. Also, we assume that the

449 crystalline crust and mantle is a Poisson solid and set $V_p = 1.73V_s$, in the sediments we use $V_p =$
450 $2.0V_s$, and for density we use the scaling relation advocated by *Christensen and Mooney* [1995]:
451 $\rho = 0.541 + 0.3601V_p$, where ρ is in g/cm^3 and V_p is in km/s . We apply a physical dispersion
452 correction [*Kanamori and Anderson, 1977*] using the Q model from PREM [*Dziewonski &*
453 *Anderson 1981*], and the resulting model is reduced to 1 sec period. Offshore, the water depth is
454 re-calculated based on a $0.2^\circ \times 0.2^\circ$ average of bathymetry at each point.

455 Models are chosen randomly guided by a Metropolis algorithm [e.g., *Mosegaard and*
456 *Tarantola, 1995*] and are accepted if the reduced χ^2 misfit to the dispersion curves is less than
457 twice the minimum misfit, χ_{\min}^2 , at each location. Reduced χ^2 misfit is the square of RMS misfit
458 defined by equation (1). RMS misfit averages less than 1.0 across the region of study. Much of
459 this misfit results from group velocities at short periods.

460 As examples, the procedure yields the eight ensembles of models presented in **Figure 12**
461 derived from the eight pairs of Rayleigh wave dispersion curves shown in **Figure 11**. The
462 ensemble is represented by the grey shaded region, which presents two standard deviations (2σ)
463 around the mean at each depth in each direction. The dispersion curves predicted by the
464 best-fitting model are shown in **Figure 11** as the blue (group velocity) and red (phase velocity)
465 lines. At each depth, the V_{sv} model that we plot in subsequent figures and its uncertainty are
466 defined by the middle and one standard deviation of the ensemble, respectively. The
467 quarter-width of the ensemble is approximately one standard deviation (1σ). The uncertainties

468 in the model are largest where shear wave speeds trade-off effectively with boundary topography,
469 which occurs near free boundaries in the model: Moho and the base of the sedimentary layer.
470 Thus, uncertainties typically grow near the top of the crystalline crust and both above and below
471 Moho.

472 The eight examples of dispersion curves and the ensembles of models that fit them, presented
473 in [Figures 11 and 12](#), demonstrate how vertically smooth models with two discontinuities can fit
474 the data well across the study region. A closer inspection of the model profiles, however, reveals
475 the limitations of inversion methods based exclusively on surface waves. In particular, the model
476 is affected by the starting model around which the Monte-Carlo method samples, particularly
477 sedimentary thickness and crustal thickness.

478 On the continent, input model-dependence is most important beneath sedimentary basins
479 where our simple parameterization of sedimentary velocities may not faithfully represent local
480 structure. A potential example of this is shown in [Figure 12e](#), beneath the Songliao Basin. Model
481 velocities beneath the basin are very low (~ 3.2 km/s) in the crystalline upper crust, which causes
482 a large vertical crustal velocity gradient that may not be realistic. Thus, errors in the input model
483 and the simplicity of parameterization of sedimentary structure may bias V_s low in the upper
484 crystalline crust. For this reason, we do not interpret the resulting 3D model at depths above the
485 lower crust. Imposition of constraints from receiver functions would help to resolve this issue,
486 but is beyond the scope of this work.

487 In the ocean, in contrast, crustal thickness in the starting model is more poorly known than on
488 the continent. Surprisingly, however, the resulting model is fairly independent of the starting
489 model. This is illustrated by [Figure 13](#), which shows the resulting ensemble of models for a point
490 in the Sea of Japan with two different starting models in which Moho is at 8 km ([Fig. 13a](#)) or 20
491 km ([Fig. 13b](#)), respectively. In both cases the surface wave data are fit admirably and nearly
492 identically (e.g., [Fig. 12h](#)). With different starting Moho depths of 8 km and 20 km, estimated
493 mantle velocities at 20 km depth are nearly identical in the two ensembles. Crustal velocities and
494 crustal thicknesses differ somewhat (average = 13 km and 15 km, respectively), but are within
495 estimated error. Although crustal thickness may vary from 10 km [*Sato et al.*, 2004] to more than
496 20 km [*Kurashimo et al.*, 1996] across the Sea of Japan, by setting the starting Moho depth to 20
497 km we are able to estimate mantle velocities reliably and recover crustal velocities and
498 thicknesses to within estimated errors. Further discussion of crustal thickness beneath the Sea of
499 Japan is presented in section 6.2, which describes the observed anti-correlation between crustal
500 thickness and sea floor depth and provides further support for the argument that crustal thickness
501 is relatively well determined beneath the area.

502 A terminological issue may require clarification. By “crustal thickness” we mean the
503 thickness of the crust including surface topography and a water layer if it exists. By “Moho
504 depth”, we mean the depth to Moho below the geoid. By “solid crustal thickness” we refer to the
505 thickness of the crust not including a water layer.

506 Results from the individual vertical profiles are aggregated into the 3-D model: the middle of
507 the ensemble of accepted models defines the model profile at each point and the spread at each
508 depth yields the uncertainty. **Figure 14** shows the V_{sv} model at four depths: (a) in the lower crust
509 at 80% of the depth to Moho, (b) 40 km, (c) 60 km, and (d) 80 km beneath the surface. Because
510 the dispersion curves extend only up to 45 sec period, the model is not reliable beyond a depth of
511 ~100 km. Estimated Moho depth and its uncertainty are shown in **Figure 15**. **Figure 15** also
512 presents the estimated velocity jump across Moho and its uncertainty. Uncertainties in shear
513 wave speed at the four depths shown in **Figure 14** are presented in **Figure 16**. Five vertical slices
514 of the model are presented in **Figure 17** along the profiles identified in **Figure 15a**: A-A'
515 extending northwest-southeast through the Songliao Basin and the Sea of Japan, B-B' running
516 northeast-southwest through the Songliao Basin and the eastern North China Craton, C-C'
517 extending roughly west-east from the Ordos Block through the North China Craton, the Bohai
518 Gulf, Korean Peninsula, and the southern Sea of Japan, D-D' running northwest-southeast from
519 Xing'an-East Mongolia through the Yellow Sea to the East China Sea, and E-E' extending
520 northwest-southeast from the Ordos Block, through the eastern NCC, to the East China Sea. The
521 model is discussed in detail in section 6.

522 Model uncertainties are presented in **Figure 15b** for Moho and in **Figure 16** corresponding to
523 the horizontal depth slices in **Figure 14**. Model uncertainties are largest near Moho, i.e., in the
524 lower crust and uppermost mantle as **Figure 16a,b** reflect. At 40 km depth, large uncertainties

525 follow the North- South Gravity Lineament, which marks the point at which Moho depth
526 approximately crosses 40 km. Uncertainties at 40 km are smallest in the Sea of Japan because the
527 crust is thinnest and this depth is most distant from Moho. Uncertainties diminish as one moves
528 deeper beneath Moho, but grow again in the deeper parts of the model as data constraints weaken
529 (Fig. 16c,d). Uncertainties in crustal thickness are nearly homogeneous across the study region,
530 but diminish somewhat beneath the Sea of Japan. Conversely, uncertainties in the velocity jump
531 across Moho are largest beneath the Sea of Japan.

532 **6. Discussion**

533 **6.1 Structural features of the 3D model**

534 As discussed in section 5, the trade-off between sedimentary thickness and shear velocities in
535 the upper crust is strong beneath the Songliao and Huabei Basins; thus, we do not present or
536 discuss upper crustal velocities here. Lower crustal velocities are much more robust, however,
537 and they are shown in Figure 14a, which is a profile taken at 80% of the Moho depth. On the
538 continent, lower crustal velocities average about 3.75 km/s, but bifurcate. Velocities are higher,
539 averaging about 3.90 km/s, beneath the Korean peninsula, the Northeast Asian Fold Belt and the
540 Songliao Basin but are slower elsewhere, including the North China Craton, the Xing'an-East
541 Mongolia, and the Yellow Sea, averaging about 3.80 km/s. The high velocity lower crust beneath
542 far eastern Asia and the Songliao Basin may represent compositional differences between these

543 regions and the tectonically distinct North China Craton and Xing'an-East Mongolia. The
544 slowest lower crustal velocities are observed beneath the Sea of Japan, running between about
545 3.50 to 3.60 km/s. The largest uncertainties in lower crustal velocities are for the Sea of Japan,
546 however (Fig. 16a).

547 We use the term “mantle lithosphere” here qualitatively and relatively, and it may be
548 substituted with the term “seismic lid”. We take it to mean the high velocity zone in the
549 uppermost mantle more or less directly below Moho. Thus, in our usage, the base of the
550 lithosphere is the depth at which velocities begin to decrease beneath a higher velocity overriding
551 mantle. With this definition, on the vertical profiles in Figure 17 the base of the lithosphere
552 occurs at the depth at which blue colors give way to green colors (~4.5 km/s) if the highest
553 velocities are blues. If the highest velocities are greens (e.g., beneath the Sea of Japan), the base
554 of the lithosphere occurs where the greens give way to white (~4.4 km/s). The term
555 “asthenosphere” is defined more quantitatively, as the region of the mantle where $V_s < 4.25$ km/s,
556 or where red colors are found in Figure 17. With these definitions, for example, the lithosphere is
557 70-80 km thick beneath the Songliao Basin (Fig. 17, B-B') and is 50-60 km thick beneath the
558 Sea of Japan (Fig. 17, A-A'). The asthenosphere exists on the vertical profiles only beneath some
559 of the North China Craton (Fig. 17, B-B', C-C'), the regions bordering the Sea of Japan (Fig. 17,
560 A-A', C-C'), and the East China Sea (Fig. 17, D-D', E-E'). Thus, with these definitions, across
561 most of the region the asthenosphere is not reached by 100 km depth. Across most of the region

562 the lithosphere is underlain by a zone that is transitional between lithospheric and asthenospheric,
563 which appears mainly as green and yellow colors on the vertical profiles.

564 In terms of deeper structures, we describe four principal features: (1) crustal thickness
565 variations across the region, (2) the lithospheric structure of the Songliao – Bohai graben, (3) the
566 uppermost mantle beneath the Sea of Japan and the East China Sea, and (4) the uppermost
567 mantle beneath the North China Craton.

568 (1) Crustal thickness is presented in [Figure 15a](#). Although internal boundaries such as Moho
569 are notoriously difficult to estimate reliably from surface waves, particularly beneath continents,
570 crustal thickness is about 40 km along the North-South Gravity Lineament (NSGL). The region
571 west of the North-South Gravity Lineament is in the crust at 40 km depth, whereas 40 km lies in
572 the mantle beneath the rest of the region. Thus, the lowest velocities near the western edge of the
573 map in [Figure 14b](#) simply reflect crustal wave speeds.

574 Beneath the Sea of Japan, as [Figure 13](#) illustrates, the ability to estimate crustal thickness
575 improves relative to the continent. A blow up of the crustal thickness is presented in [Figure 18a](#).
576 As expected, the crust is thinnest where the sea is deepest, principally in the Japan Basin, which
577 defines the northern and western parts of the Sea of Japan. The crust thickens, for example,
578 beneath the Yamato Rise, the topographic rise in the central Sea of Japan. Crustal thickness
579 beneath the Sea of Japan is discussed further in section 6.2, where the anti-correlation observed

580 between crustal thickness and water depth is used to support the reliability of the crustal
581 thickness estimates in oceanic regions.

582 (2) At 40 km depth east of the North-South Gravity Lineament relatively high wave speeds
583 (>4.4 km/s) lie beneath the Songliao Basin and run to the Bohai Sea, as [Figure 14b](#) shows. The
584 high velocities beneath the Songliao Basin form a lid that extends to 60-70 km but then
585 terminates, being underlain by more normal continental uppermost mantle wave speeds beneath
586 the Basin by 80 km depth. This can be seen clearly on vertical profiles A-A' and B-B' of [Figure](#)
587 [17](#), in which the relatively thick fast lithosphere beneath the Songliao graben is contrasted with
588 the thinner slower lithosphere of the North China Craton and the Sea of Japan. The mantle
589 lithosphere, however, beneath the Songliao Basin is not cratonic in nature, contrasting with the
590 much thicker lithosphere beneath the Ordos Block (e.g., [Fig. 14d](#)). Although the Ordos Block is
591 only partially imaged in this study, high velocities are seen to underlie it in the uppermost mantle
592 extending at least to 100 km depth (and presumably deeper) as vertical profile C-C' in [Figure 17](#)
593 illustrates. Although the lithosphere underlying the Songliao Basin is not as thin as beneath the
594 North China Craton, it is thin for a region believed to have a basement of Archean age.

595 (3) At 40 km depth, relatively high wave speeds (>4.4 km/s) also underlie the Yellow and
596 Japan Seas. Although similar in the uppermost mantle, below 40 km the mantle structures
597 beneath these seas lose their similarity. The uppermost mantle beneath the Yellow Sea is
598 continental in character as profile D-D' in [Figure 17](#) shows. Much lower wave speeds exist in the

599 back-arc spreading region beneath the Sea of Japan, as can be seen on [Figure 14c,d](#). Starting at
600 about 60 km depth, low velocities bound the eastern margin of the Sea of Japan and also to a
601 somewhat lesser extent the western margin, extending onto the continent. Low velocities also
602 bound the eastern edge of the East China Sea, east and southeast of the Yellow Sea near the
603 Ryuku Islands. By 80 km depth, the bifurcated low velocity zone across the Sea of Japan has
604 largely merged into a more homogeneous low velocity asthenosphere beneath the entire sea, and
605 the western edge of the anomaly has spread further inland to underlie the Northeast Asia Foldbelt,
606 including the volcanic region of the Changbai Mountains. This is presented most clearly in
607 [Figure 19](#), which displays two low velocity contours at 80 km depth: $V_s < 4.25$ km/s and 4.25
608 $\text{km/s} \leq V_s < 4.35$ km/s. This also can be seen clearly in profile A-A' of [Figure 17](#), which extends
609 across the center of the Sea of Japan, but is also visible in profile C-C' which run through the sea
610 farther south. We refer to the low velocities bounding the Sea of Japan as a “Y-shaped” anomaly
611 on vertical profiles, which is apparent on profile A-A'. A relatively high velocity 50-60 km thick
612 lithosphere is observed beneath the central Sea of Japan, as profiles A-A' and C-C' illustrate. This
613 relatively thin lithosphere should be contrasted with the thicker faster lithosphere beneath the
614 Songliao Basin, which is clearly seen on profile A-A'. The bordering Y-shaped asthenospheric
615 anomaly and the thin lithosphere underlying the Sea of Japan are discussed further in section 6.3.

616 The East China Sea lies near the southeastern corner of our study region, but like the Sea of
617 Japan its eastern margin near the Ryuku Islands is underlain by low velocities in the uppermost

618 mantle. This is apparent in [Figure 19](#), [Figure 14d](#) and vertical profile D-D' in [Figure 17](#). Unlike
619 the Sea of Japan, however, there is no “Y-shaped” anomaly beneath the East China Sea as the
620 western part of the sea merges with fast continental lithosphere beneath the Yellow Sea with no
621 low velocity feature in the uppermost mantle.

622 (4) The North China Craton deviates from most of the rest of continental northern and
623 northeastern China by possessing much slower wave speeds at depths greater than about 60 km.
624 This can be seen clearly on profile B-B' of [Figure 17](#), which shows that the mantle lithosphere
625 beneath the North China craton is thinner and slower than beneath the Songliao Basin. Profile
626 C-C' illustrates, however, that the lithosphere extends deeper than beneath the Sea of Japan, with
627 underlying asthenosphere that is not as slow. However, asthenospheric wave speeds do underlie
628 the lithosphere beneath the North China Craton below about 80 km depth. These low wave
629 speeds in the uppermost mantle are horseshoe in shape on horizontal cross-sections across the
630 eastern North China Craton as seen in [Figure 19](#), in which the low velocities follow the western
631 and eastern flanks of the eastern part of the North China Craton. The middle of the eastern part of
632 the North China Craton is not slow, however. The seismic structure of the North China Craton is
633 discussed further in section 6.4.

634

635 **6.2 Seafloor depth and crustal thickness beneath the Sea of Japan**

636 The crustal structure beneath the Sea of Japan is highly heterogeneous [e.g., *Taira, 2001*].
637 The Japan Basin is principally oceanic crust, while most of the Yamamoto and Tsushima basins
638 are extended continental crust, the Korean Plateau and Yamamoto Rise are composed mainly of
639 continental crust, and the eastern and southern boundaries of the Sea are rifted continental crust
640 [*Tamaki et al., 1992*]. Thus, crustal thickness varies appreciably across the basin in a way that we
641 expect to be related to seafloor depth, assuming isostatic compensation. **Figure 18b** presents
642 seafloor depth (bathymetry) across the Sea of Japan plotted versus solid crustal thickness from
643 our 3-D model. Seafloor depth and our estimate of crustal thickness (**Fig. 18a**) are correlated,
644 although there is substantial scatter. Assuming that water depth, H_W , is the dependent variable
645 and solid crustal thickness, H_C , is the independent variable, the least-squares linear fit, shown as
646 the solid red line in **Figure 18b**, is $H_W = -0.22 H_C + 6.07$, where H_W , H_C , and the constant term
647 are in km. The linear fit provides a variance reduction of 57%.

648 The observed derivative $dH_W/dH_C = -0.22$ provides information about the nature of isostatic
649 compensation in the region. For crustal Airy isostasy, with mantle density equal to 3.32 g/cm^3
650 and a water density of 1.05 g/cm^3 , dH_W/dH_C can be computed for different crustal densities. For
651 an average continental crustal density of $\rho_{\text{cont}} = 2.75 \text{ g/cm}^3$, $dH_W/dH_C \approx -0.25$, and for an average
652 oceanic crustal density of $\rho_{\text{oc}} = 2.9 \text{ g/cm}^3$, $dH_W/dH_C \approx -0.19$. Thus, the estimated value of
653 $dH_W/dH_C = -0.22$ is understood to be an average of the values expected if the Sea of Japan were
654 composed homogeneously of either oceanic or continental crust. In fact, much of the scatter

655 around the linear fit seen in **Figure 18b** is due to crustal heterogeneity across the sea. However,
656 local isostasy may not be dominated by the crystalline crust alone, but may also be affected
657 strongly by sediments and thermal buoyancy from the mantle, both of which have been ignored
658 in the analysis here.

659 Many different lines could, in fact, fit the data in **Figure 18b** nearly as well as the linear fit
660 discussed above, which is presented with the solid red line. For example, if we assume that water
661 depth, H_W , is the independent variable and solid crustal thickness, H_C , is the dependent variable,
662 the least-squares linear fit, shown with the dashed red line in **Figure 18b**, would be $H_W = -0.41$
663 $H_C + 9.07$. Thus, a more careful analysis that considers lateral crustal heterogeneity, thermal
664 buoyancy from the mantle, the effects of sediments, and uncertainties in the crustal thickness
665 estimates is needed, but is beyond the scope of this paper. The results presented here demonstrate
666 the reliability of the crustal thickness estimates across the Sea of Japan and also provide evidence
667 that further analysis of the relation between seafloor depth and crustal thickness is warranted.

668 **6.3 Lithospheric and asthenospheric structure beneath the Sea of Japan**

669 Our 3-D model images what we refer to as a “Y-shaped” anomaly on vertical profiles with
670 low velocity arms reaching upward beneath the eastern and western borders of the Sea of Japan
671 extending well into continental East Asia on the west side (e.g., **Fig. 17**, A-A’), with an overlying
672 ~60 km thick lithosphere beneath the Sea of Japan. The location of the lowest wave speeds at 80

673 km depth can be seen in **Figure 19**. In recent years, several other tomographic studies have been
674 performed that are complementary to the ambient noise tomography presented here, which have
675 imaged the mantle beneath the Sea of Japan. These studies possess greater depth penetration
676 although lower resolution than our study and provide validation and assist with interpreting our
677 results.

678 Based on Rayleigh and Love wave phase velocities obtained from teleseismic earthquakes
679 using the two-station method, *Yoshizawa et al.* [2010] present a 3-D model of shear wave speeds
680 from 40 to 200 km depth. Although their resolution is best beneath Japan and fades by the central
681 Sea of Japan, their results in regions of good data coverage are similar to ours in several respects.
682 First, they report an average lithospheric thickness beneath the Yamato Rise and the Japan Basin
683 of 60 ± 10 km, which is similar to what we observe (e.g., **Fig. 17**, A-A', C'C'). Second, they also
684 observe low velocity anomalies at 75 km depth bordering Honshu beneath the eastern Sea of
685 Japan and the East China Sea, west of the Ryuku Islands. Thus, they also image the eastern arm
686 of the Y-shaped anomaly that we report here and, like our model, observe it to migrate westward
687 with depth. Their data coverage does not extend into East Asia. However, the teleseismic body
688 wave study of *Zhao et al.* [2007] presented a large-scale image of the upper mantle beneath east
689 Asia, which shows the stagnation of the subducted Pacific Plate beneath the Sea of Japan and
690 clear low velocity anomalies in the back-arc region. This study concentrates interpretation on the
691 release of volatiles from the slab at several depths to produce the low velocity anomalies

692 observed in the back-arc region.

693 Thus, *Yoshizawa et al.* [2010] serves to validate our model and *Zhao et al.* [2007] provides a
694 means to interpret the Y-shaped anomaly based on what they call the “Big Mantle Wedge” model
695 of the Japanese back-arc and the devolatilization of the subducted slab. In their interpretation, the
696 western arm of the Y-shaped anomaly beneath the western Sea of Japan and the East Asian Fold
697 Belt would be caused by dehydration reactions of the stagnant slab in the mantle boundary layer
698 (410-660 km). These warm hydrated upwellings are the cause of volcanism in East Asia (e.g.,
699 Changbai volcano) and may have precipitated the crustal rifting that led to the opening of the Sea
700 of Japan. Presumably, the stagnant slab would generate hydrated plumes across the entire Sea of
701 Japan, but the stretched and thinned continental lithosphere remains intact beneath the central
702 Sea of Japan, as **Figure 17** A-A’, C-C’ demonstrate, impeding upward migration of the hydrated
703 plumes. These plumes would then become part of a westward directed convecting system that
704 would amplify mantle hydration in the western Sea of Japan, near the rift margin. The eastern
705 arm of the Y-shaped anomaly would be caused by slab dehydration at shallower depths, possibly
706 caused by antigorite-related reactions. Thus, the Y-shaped anomaly reflects the details of shallow
707 and deep slab dehydration and convective circulation in the mantle wedge above a stagnant slab.

708

709 **6.4 Lithospheric Rejuvenation of the North China Craton**

710 The Chinese part of the Sino-Korean Craton, called the North China Craton (NCC), is
711 composed of two Archean blocks, the eastern and the western NCC, which are separated by the
712 central NCC. The central NCC is a Paleoproterozoic orogen called the Trans-North China
713 Orogen. The three parts of the NCC are separated by dashed red lines in **Figure 2**. The NCC is
714 believed to have cratonized by about 1.85 Ga, but the eastern NCC has undergone significant
715 tectonothermal rejuvenation from the Ordovician to Cenozoic [*Menzies et al., 1993, 2007;*
716 *Griffin et al., 1998; Gao et al., 2002, 2004; Zhao et al., 2005, 2008*]. These conclusions have
717 been based on basalt-borne xenoliths and geophysical evidence for thin lithosphere (< 100 km)
718 with high heat flow in this region from the early Cenozoic to the present [e.g., *Menzies et al.,*
719 *1993; Griffin et al., 1998; Fan et al., 2000; Xu, 2001; Wu et al., 2005; Chen et al., 2006, 2008,*
720 *2009*]. Most studies agree that the central and western parts of the NCC have evolved differently
721 than the eastern NCC during Phanerozoic time [e.g., *Xu et al., 2004; Xu, 2007*], although some
722 recent seismic studies point to localized lithospheric thinning in the central and even western
723 NCC [e.g., *Huang et al., 2009; Chen et al., 2009*] and the generally high lateral heterogeneity of
724 the lithosphere underlying the NCC. The mechanism of Phanerozoic lithospheric rejuvenation
725 and its variability across the NCC remain intensely debated [e.g., *Chen, 2010* for a recent
726 summary]. Understanding of the Phanerozoic lithospheric tectonics would be improved with
727 clearer images of the current structure of the crust, mantle lithosphere, and asthenosphere across
728 the NCC.

729 To this debate our 3-D model presents new relatively high-resolution images of the crust and
730 uppermost mantle beneath most of the NCC. Crustal velocities beneath the eastern NCC are not
731 particularly distinct from surrounding regions (e.g., Fig. 14a), although the crust may be slightly
732 thinner, on average (Fig. 15a). More significantly, the eastern NCC hosts a “horseshoe” shaped
733 anomaly in map view in the uppermost mantle, which is identified at 80 km depth in Figure 14d
734 and, perhaps more clearly, by the blue contour in Figure 19. The velocities are lowest in the
735 northern part of the North China Platform near the intersection of the North-South Gravity
736 Lineament (NSGL) with the boundary between the central and eastern NCC. The low velocities
737 continue southward, flanking the eastern NCC along the NSGL in the west and the TLF in the
738 east. Low velocities also extend into small parts of the central NCC and the western NCC near
739 the Datong Volcanoes. The south central part of the NCC is not particularly slow in the
740 uppermost mantle as Figure 17 profile E-E’ illustrates, which reveals the considerable variability
741 of lithospheric structure even within the eastern NCC.

742 Within the “horseshoe” shaped anomaly bounding three sides of the eastern NCC (Fig. 19),
743 the lithosphere can be seen to be about 60 km thick on vertical profiles B-B’ and C-C’ of Figure
744 17. The flanks of the eastern NCC are underlain by asthenospheric low velocity anomalies below
745 70 km depth as can be seen on profiles B-B’, C-C’, and E-E’. Profile B-B’ illustrates that the
746 lithosphere is not simply thin; the velocities are lower than beneath the Songliao Basin to the
747 north and the Ordos Block to the west. Thus, we hypothesize that the low velocity anomalies that

748 bound three sides of the eastern NCC identify a region of more intense tectonothermal activity
749 than in south-central part of the eastern NCC. Indeed, lithospheric rejuvenation may have
750 reached nearly to the base of the crust in the most intensely altered zones.

751 **7. Conclusions**

752 This paper presents a high-resolution 3-D shear velocity model of the crust and uppermost
753 mantle with associated uncertainties across the North China Craton, northeastern China, the
754 Korean Peninsula, and the Sea of Japan constructed from the dispersion characteristics of
755 Rayleigh waves obtained from ambient noise cross-correlations. Broadband stations from
756 Chinese Provincial Networks, the Japanese F-Net, and the IRIS GSN have produced two-year
757 continuous time series from 2007 into 2009 that form the basis for these results. Phase and group
758 velocity maps from 8 sec to 45 sec period are first constructed, which constrain earth structures
759 in the crust and uppermost mantle to a depth of about 100 km. The dispersion maps are
760 geologically coherent, displaying the signatures of sedimentary basins, mountain roots,
761 ocean-continent variations, and anomalies due to rifting and volcanism. The maps at different
762 periods and between phase and group velocities are consistent with one another, and vertically
763 relatively smooth V_{sv} models fit the observations.

764 To generate the dispersion maps presented here, the effects of the persistent localized
765 Kyushu microseism had to be eliminated in the dispersion measurements. We present a method
766 based on locating the microseism (thereby confirming the location of *Zeng and Ni* [2010]),

767 predicting the arrival of the disturbing signal on the ambient noise cross-correlations, and
768 obtaining the dispersion measurements by using the Green's functions at the opposite
769 cross-correlation lag times for the station pairs in which the apparent speed of the Kyushu signal
770 is less than 4.5km/s.

771 Ambient noise tomography places unique constraints on the structure of the crust and
772 uppermost mantle, providing information complementary to body wave travel times, receiver
773 functions, longer period teleseismic surface waves, gravity, and other types of data. The
774 motivation for the 3-D model is to produce new constraints on the volcanism, crustal extension,
775 cratonic rejuvenation, and lithospheric thinning that are hypothesized for the region of study. The
776 model presented here provides new information about these processes, particularly about the
777 geometry (the geographic distribution and depth extent) of the observed features in the top 100
778 km. A detailed interpretation of the model is inconsistent with the scope of this paper, but we
779 focus discussion on four principal model features: crustal thickness variations, particularly those
780 associated with the North-South Gravity Lineament (NSGL) and beneath the Sea of Japan, the
781 prominent but thin lithosphere underlying the Songliao-Bohai Graben, the “Y-shaped” mantle
782 low velocity anomaly (on vertical profiles) bordering the Sea of Japan, and a “horse-shoe”
783 shaped asthenospheric anomaly (in map view) bounding three sides of the eastern North China
784 Craton.

785 (1) The North-South Gravity Lineament is observed to follow approximately the 40 km

786 crustal thickness contour. Beneath the Sea of Japan, crustal thickness is anti-correlated with
787 water depth, and the relationship is consistent with expectations based on crustal isostasy for a
788 laterally compositionally variable crust. (2) The Songliao-Bohai Graben is underlain by a high
789 velocity lower crust and a fast mantle lithosphere that extends to about 70 km depth. The
790 lithosphere is not attenuated, that is seismic velocities are high, but it is thinner than expected for
791 a region in which parts are traceable back to the Archean. (3) Low velocity anomalies reach
792 upward beneath the eastern and western borders of the Sea of Japan, extending well into
793 continental East Asia on the west side. The arms of this Y-shaped anomaly are separated by the
794 intervening overlying lithosphere, which is ~60 km thick and may represent stretched continental
795 lithosphere. We argue that the Y-shaped structure in the east reflects relatively shallow slab
796 dehydration and in the west deeper dehydration and convective circulation in the mantle wedge
797 overlying the stagnant slab. (4) Very thin, attenuated lithosphere bounds three sides of the eastern
798 North China Craton (NCC), but somewhat thicker faster lithosphere underlies the central and
799 southern parts of the eastern NCC. These low velocity anomalies identify a region of intense
800 tectonothermal modification where lithospheric rejuvenation may have reached nearly to the
801 base of the crust.

802 In the future, assimilating similar results from a companion paper for southern China [*Zhou*
803 *et al.*, 2011] will allow the 3-D model to extend across all of eastern China. The geometry of the
804 observing array makes the application of differential travel time methods for earthquakes

805 difficult, such as eikonal tomography [*Lin et al.*, 2009], Helmholtz tomography [*Lin and*
806 *Ritzwoller*, 2011], or two-plane wave tomography [e.g., *Yang et al.*, 2008b]. However, the
807 success of such methods would allow dispersion maps to be extended to longer periods and,
808 therefore, for the model to reach greater depths in the mantle. In addition to the production of a
809 3-D Vs model of the crust and uppermost mantle, other research envisioned includes the
810 estimation of azimuthal anisotropy, which would place complementary constraints on the
811 physical processes that motivate this study. In addition, future understanding of the dispersion
812 characteristics of Love waves would allow estimation of radial anisotropy, which reflects
813 deformation undergone by the crust and uppermost mantle.

814

815

816

817

818

819

820

821

822 **Acknowledgement.** The authors wish to thank An Yin and an anonymous reviewer for
823 constructive criticism of an early draft and the AE for particularly insightful comments on a late
824 draft of this paper. We are grateful to Anatoli Levshin, Fan-Chi Lin, and Shijie Zhong for
825 valuable conversations. This work was performed while the first author visited the University of
826 Colorado at Boulder over a period of one year. The work was supported by NSFC grant
827 40974034, CAS grant kzcx2-yw-142 and Y009021002, NSFC 41174086, CEA grant 201008007,
828 US NSF-EAR award 0944022, and US NSF-OISE sub-award 0730154. Most of the waveform
829 data for this study were provided by the Data Management Centre of the China National Seismic
830 Network at the Institute of Geophysics, China Earthquake Administration and F-Net in Japan. In
831 addition, the facilities of the IRIS Data Management System were used to access data required in
832 this study. The IRIS DMS is funded through the US National Science Foundation under
833 Cooperative Agreement EAR-0552316.

834

835

836

837

838

839 **References**

840 Bai, L., H. Kawakatsu, and Y. Morita (2010), Two anisotropic layers in central orogenic belt of the North
841 China Craton, *Tectonophysics*, 494:138-148.

842 Barmin, M. P., M. H. Ritzwoller, and A. L. Levshin (2001), A fast and reliable method for surface wave
843 tomography, *Pure Appl. Geophys.*, 158:1351-1375.

844 Bassin, C., G. Laske, and G. Masters (2000), The current limits of resolution for surface wave tomography
845 in North America. *EOS Trans AGU 81*, F897.

846 Bensen, G. D., M. H. Ritzwoller, M. P. Barmin, A. L. Levshin, F. Lin, M. P. Moschetti, N. M. Shapiro, and
847 Y. Yang (2007), Processing seismic ambient noise data to obtain reliable broad-band surface wave
848 dispersion measurements, *Geophys. J. Int.*, 169: 1239-1260.

849 Bensen, G.D., M.H. Ritzwoller, and N.M. Shapiro (2008), Broad-band ambient noise surface wave
850 tomography across the United States, *J. Geophys. Res.*, 113, B05306, 21 pages,
851 doi:10.1029/2007JB005248, 2008.

852 Bensen, G. D., M. H. Ritzwoller and Y. Yang (2009), A 3-D shear velocity model of the crust and
853 uppermost mantle beneath the United States from ambient seismic noise, *Geophys. J. Int.*, 177:
854 1177-1196.

855 Bourova, E., K. Yoshizawa, and K. Yomogida (2010). Upper mantle structure of marginal seas and
856 subduction zones in northeastern Eurasia from Rayleigh wave tomography, *Phys. Earth. Planet.*
857 *Int.*, 183: 20-32.

858 Chen, L. (2010). Concordant structural variations from the surface to the base of the upper mantle in the
859 North China Craton and its tectonic implications, *Lithos*, 120: 96-115.

860 Chen, L., T. Zheng, W. Xu (2006). Athinned lithospheric image of the Tanlu Fault Zone, eastern China:
861 constructed from wave equation based receiver function migration, *J. Geophys. Res.*, 111, B09312.
862 doi:10.1029/2005JB003974.

863 Chen, L., T. Wang, L. Zhao, T. Zheng (2008). Distinct lateral variation of lithospheric thickness in the
864 Northeastern North China Craton, *Earth Planet. Sci. Lett.*, 267: 56–68.

865 Chen, L., C. Cheng, and Z. Wei (2009), Seismic evidence for significant lateral variations in lithospheric
866 thickness beneath the central and western North China Craton, *Earth Planet. Sci. Lett.*, 286:
867 171-183.

868 Cho, K.H., Herrmann, R.B., Ammon, C.J., Lee, K. (2007), Imaging the upper crust of the Korean
869 Peninsula by surface-wave tomography. *Bull. Seism. Soc. Am.*, **97** (1): 198-207 Part B Sp. Iss. S.

870 Christensen, N.I. & Mooney, W.D. (1995), Seismic velocity structure and composition of the continental
871 crust: A global view, *J. Geophys. Res.*, 100(B6): 9761–9788.

872 Deng, J., S. Su, Y. Niu, C. Liu, G. Zhao, X. Zhao, S. Zhou, and Z. Wu (2007), A possible model for the
873 lithospheric thinning of the North China Craton: Evidence from the Yanshanian (Jura-Cretaceous)
874 magmatism and tectonism, *Lithos*, 96: 22-35.

875 Dziewonski, A. and D. Anderson (1981), Preliminary reference Earth model, *Phys. Earth Planet. Int.*, 25(4):
876 297–356.

877 Ekstrom, G., and A. M. Dziewonski (1997), Three-dimensional velocity structure of the Earth's upper
878 mantle, in *Upper Mantle Heterogeneities From Active and Passive Seismology*, edited by K. Fuchs,
879 pp. 187–198, Kluwer Acad., Norwell, Mass.

880 Fan, W., H. Zhang, J. Baker, K. Jarvis, P.R.D. Mason, M. Menzies (2000). On and off the North China
881 Craton: where is the Archaean keel?, *Journal of Petrology*, 41(7):933–950.

882 Fang L., J. Wu, Z. Ding, G. Panza (2010), High resolution Rayleigh wave group velocity tomography in
883 North-China from ambient seismic noise, *Geophys. J. Int.*, 181(2): 1171-1182.

884 Gao, S., R. Rudnick, R. Carlson, W. McDonough, Y. Liu (2002), Re–Os evidence for replacement of
885 ancient mantle lithosphere beneath the North China Craton, *Earth Planet. Sci. Lett.*, 198: 307–322.

886 Gao, S. R.L. Rudnick, H. Yuan, X. Liu, Y. Liu, W. Xu, W. Ling, J. Ayers, X. Wang, and Q. Wang (2004),
887 Recycling lower continental crust in the North China craton, *Nature*, 432:892-897.

888 Gao, S. R.L. Rudnick, W. Xu, H. Yuan, Y. Liu, R. Walker, I. Puchtel, X. Liu, H. Huang, X. Wang, J. Yang
889 (2008), Recycling deep cratonic lithosphere and generation of intraplate magmatism in the North
890 China Craton, *Earth Planet. Sci. Lett.*, 270: 41-53.

891 Griffin, W.L., A. Zhang, S.Y. O'Reilly, C. Ryan (1998), Phanerozoic evolution of the lithosphere beneath
892 the Sino-Korean Craton. In: Flower, M., S. Chung, C. Lo, T. Lee (Eds.), *Mantle dynamics and plate*

893 *interactions in East Asia*, AGU Geodynamics Series, Vol. 27: 107-126.

894 Guo, Z., X. Gao, H. Yao, J. Li, W. Wang (2009), Mid-crustal low velocity layer beneath the central
895 Himalaya and southern Tibet revealed by ambient noise array tomography, *Geochem. Geophys.*
896 *Geosyst.*, 10(5), Q05007, doi:10.1029/2009GC002458.

897 He, Z., T. Ye, and Z. Ding (2009), Surface wave tomography for the phase velocity in the northeastern
898 part of North China, *Chinese J. Geophys.*, 52(5): 1233-1242.

899 Huang, H., H. Yao, and R.D. van der Hilst (2010), Radial anisotropy in the crust of SE Tibet and SW
900 China from ambient noise interferometry, *Geophys. Res. Lett.*, 37, L21310, 5 pp.,
901 doi:10.1029/2010GL044981.

902 Huang, J. and D. Zhao (2006), High-resolution mantle tomography of China and surrounding regions, *J.*
903 *Geophys. Res.*, 111, doi:10.1029/2005JB004066.

904 Huang, Z., H. Li, Y. Zheng, and Y. Peng (2009), The lithosphere of North China Craton from surface
905 wave tomography, *Earth Planet. Sci. Lett.*, 288:164-173.

906 Huang, Z., Y. Peng, Y. Luo, Y. Zheng, W. Su (2004), Azimuthal anisotropy of Rayleigh waves in East Asia.
907 *Geophys. Res. Lett.* 31, L15617. doi:10.1029/2004GL020399.

908 Huang, Z., W. Su, Y. Peng, Y. Zheng, and H. Li (2003), Rayleigh wave tomography of China and adjacent
909 regions, *J. Geophys. Res.*, 108, doi:10.1029/2001JB001696.

910 Jolivet, L. K., K. Tamaki, M. Fournier (1994), Japan Sea, opening history and mechanism: a synthesis. *J.*
911 *Geophys. Res.* 99:22237-22259.

912 Kang, T.S. and Shin, J.S. (2006), Surface-wave tomography from ambient seismic noise of accelerograph
913 networks in southern Korea. *Geophys. Res. Lett.* **33** (17), L17303.

914 Kanamori, H. and D. Anderson (1977), Importance of physical dispersion in surface wave and free
915 oscillation problems : Review, *Revs. Geophys. Space Phys.*, 15(1):105-112.

916 Kawakatsu, H., M. Yamamoto, S. Kaneshima, and T. Ohkura (2011), Comment on “A persistent localized
917 microseismic source near the Kyushu Island, Japan” by Xiangfang Zeng and Sidao Ni, *Geophys.*
918 *Res. Lett.*, 38, L17307, doi:10.1029/2011GL048584 .

919 Kurashimo, E., Shinohara, M., Suyehiro, K., Kasahara, J., Hirata, N. (1996), Seismic evidence for
920 stretched continental crust in the Japan Sea. *Geophys. Res. Lett.* 23:3067-3070.

921 Lebedev, S., and G. Nolet (2003), Upper mantle beneath Southeast Asia from S velocity tomography, *J.*
922 *Geophys. Res.*, 108, doi:10.1029/2000JB000073.

923 Levshin, A., M.H. Ritzwoller, and J. Resovsky (1999), Source effects on surface wave group travel times
924 and group velocity maps, *Phys. Earth Planet. Int.*, 115:293 - 312.

925 Levshin, A., M. Barmin, M.H. Ritzwoller, and J. Trampert (2005), Minor-arc and major-arc global surface
926 wave diffraction tomography, *Phys. Earth Planet. Ints.*, 149:205-223.

- 927 Li, C. and R.D. van der Hilst (2010), Structure of the upper mantle and transition zone beneath Southeast
928 Asia from travelttime tomography, *J. Geophys. Res.*, 115, B07308, doi:1029/2009JB006882.
- 929 Li, H.Y., W. Su, , C.Y.Wang, , Z. X. Huang (2009), Ambient noise Rayleigh wave tomography in western
930 Sichuan and eastern Tibet. *Earth Planet. Sci. Lett.* 282 (1-4): 201-211.
- 931 Li, J. and F. Niu (2010), Seismic anisotropy and mantle flow beneath northeast China inferred from
932 regional seismic networks, *J. Geophys. Res.*, 115, B12327, doi:10.1029/2010JB007470.
- 933 Li, Z., T. Hao, and Y. Xu (2011), Uppermost mantle structure of the North China Craton: Constraints from
934 interstation Pn travel time diference tomography, *Chin. Sci. Bull.*, 56:1691-1699.
- 935 Lin, F.C., M.P. Moschetti, and M.H. Ritzwoller (2008), Surface wave tomography of the western United
936 States from ambient seismic noise: Rayleigh and Love wave phase velocity maps, *Geophys. J. Int.*,
937 doi:10.1111/j1365-246X.2008.03720.x.
- 938 Lin, F.C. and M.H. Ritzwoller (2011), Helmholtz surface wave tomography for isotropic and azimuthally
939 anisotropic structure, *Geophys. J. Int.*, 186, 1104-1120, doi: 10.1111/j.1365-246X.2011.05070.x.
- 940 Lin, F., M.H. Ritzwoller, J. Townend, M. Savage, S. Bannister (2007). Ambient noise Rayleigh wave
941 tomography of New Zealand, *Geophys. J. Int.*, 170(2): 649-666,
942 doi:10.1111/j.1365-246X.2007.03414.x,
- 943 Lin, F., M.H. Ritzwoller, and R. Snieder (2009), Eikonal tomography: Surface wave tomography by
944 phase-front tracking across a regional broad-band seismic array, *Geophys. J. Int.*, 177(3):

945 1091-1110.

946 Lin, F., M.H. Ritzwoller, Y. Yang, M. Moschetti, and M. Fouch (2011), Complex and variable crustal and
947 uppermost mantle seismic anisotropy in the western United States, *Nature Geoscience*, 4(1): 55-61.

948 Liu, J., J. Han, and W. Fyfe (2001), Cenozoic episodic volcanism and continental rifting in Northeast
949 China and possible link to Japan Sea development as revealed from K-Ar geochronology,
950 *Tectonophysics*, 339:385-401.

951 Menzies, M.A., W. Fan, and M. Zhang (1993), Paleozoic and Cenozoic lithoprobes and the loss of >120
952 km of Archean lithosphere, Sino-Korean craton, *China. Geol. Soc. Long. Spec. Pub.*, 76:71-81.

953 Menzies, M., Y. Xu, H. Zhang, and W. Fan (2007), An integration of geology, geophysics, and
954 geochemistry: A key to understanding the North China Craton, *Lithos*, 96: 1-21.

955 Moschetti, M., M.H. Ritzwoller, and F. Lin (2010a), Seismic evidence for widespread crustal deformation
956 caused by extension in the western USA, *Nature*, 464(7290): 885-889.

957 Moschetti, M., M.H. Ritzwoller, F. Lin, and Y. Yang (2010b), Crustal shear velocity structure of the
958 western US inferred from ambient noise and earthquake data, *J. Geophys. Res.*, 115, B10306,
959 doi:10.1029/2010JB007448.

960 Moschetti, M., M. Ritzwoller, and N. Shapiro (2007), Surface wave tomography of the western United
961 States from ambient seismic noise: Rayleigh wave group velocity maps, *Geochem. Geophys.*
962 *Geosyst.*, 8, Q08010, doi:10.1029/2007GC001655.

963 Mosegaard, K., and A. Tarantola (1995) , Monte Carlo Sampling of Solutions to Inverse Problems, *J.*
964 *Geophys. Res.*, 100(B7): 12431-12447.

965 Nishida, K., Kawakatsu, H., Obara, K. (2008), Three-dimensional crustal S wave velocity structure in
966 Japan using microseismic data recorded by Hi-net tiltmeters. *J. Geophys. Res.-Solid Earth*, **113**
967 (B10):B10302.

968 Okada, Y., K. Kasahara, S. Hori, K. Obara, S. Sekiguchi, H. Fujiwara, and A. Yamamoto (2004), Recent
969 progress of seismic observation networks in Japan – Hi-net, F-net, K-Net and KiK-net, *Earth*
970 *Planets Space*, 56, xv-xxviii.

971 Pan, J., Q. Wu, Y. Li, F. Zhang, G. Zhang (2011), Rayleigh wave tomography of the phase velocity in
972 North China, *Chinese J. Geophys.*, 54(1): 67-76.

973 Priestley, K., E. Debayle, D. McKenzie, S. Pilidou (2006), Upper mantle structure of eastern Asia from
974 multimode surface waveform tomography. *J. Geophys. Res.* 111, B10304.
975 doi:10.1029/2005JB004082.

976 Ren, J. K. Tamaki, S. Li, and J. Zhang (2002). Late Mesozoic and Cenozoic rifting and its dynamic
977 setting in eastern China and adjacent seas, *Tectonophysics*, 344: 175-205.

978 Ritzwoller, M.H. and A. Levshin (1998), Eurasian surface wave tomography: Group velocities, *J.*
979 *Geophys. Res.*, 103: 4839-4878.

980 Ritzwoller, M.H., A. Levshin, L. Ratnikova, and A. Egorkin (1998), Intermediate period group velocity

981 maps across Central Asia, Western China, and parts of the Middle East, *Geophys. J. Int.*, 134:
982 315-328.

983 Rogers, J.J.W. and M. Santosh (2006), The Sino-Korean Craton and supercontinent history: Problems and
984 perspectives, *Gondwana Res.*, 9:21-23.

985 Sabra, K. G., P. Gerstoft, P. Roux, W. A. Kuperman, and M. C. Fehler (2005), Surface wave tomography
986 from microseisms in Southern California, *Geophys. Res. Lett.* 32, L14311.

987 Santosh, M., D. Zhao, and T. Kusky (2010), Mantle dynamics of the Paleoproterozoic North China Craton:
988 A perspective based on seismic tomography, *J. Geodyn.* 49: 39-53.

989 Sato, T., Shinohara, M., Karp, B.Y., Kulinich, R.G., Isezaki, N. (2004), P-wave velocity structure in the
990 northern part of the central Japan Basin, Japan Sea with ocean bottom seismometers and airguns.
991 *Earth Planets Space*, 56: 501–510.

992 Sengor, A.M. C., B. A. Natal'in (1996), Paleotectonics of Asia: fragments of a synthesis. In *The tectonic*
993 *evolution of Asia*, edited by Yin, A. and Harrison, T. M., Cambridge University Press, pp. 486-640.

994 Shapiro, N.M. and M.H. Ritzwoller (2002), Monte-Carlo inversion for a global shear velocity model of
995 the crust and upper mantle, *Geophys. J. Int.*, 151: 88-105.

996 Shapiro, N.M., M. Campillo, L. Stehly, and M.H. Ritzwoller(2005), High-resolution surface wave
997 tomography from ambient seismic noise. *Science* 307, 1615-1618.

998 Shapiro, N.M., M.H. Ritzwoller, and G.D. Bensen (2006), Source location of the 26 sec microseism from
999 cross correlations of ambient seismic noise, *Geophys. Res. Lett.*, 33, L18310,
1000 doi:10.1029/2006GL027010.

1001 Shapiro, N.M., M.H. Ritzwoller, P. Molnar, and V. Levin (2004). Thinning and flow of Tibetan crust
1002 constrained by seismic anisotropy, *Science*, 305: 233-236.

1003 Sun, Y. and N. Toksoz (2006), Crustal structure of China and surrounding regions from P wave travetime
1004 tomography, *J. Geophys. Res.*, 111, B03310, doi:10.1029/2005JB003962.

1005 Sun, X., X. Song, S. Zheng, Y. Yang, M. Ritzwoller (2010), Three dimensional shear velocity structure of
1006 crust and upper mantle in China from ambient noise surface wave tomography, *Earthquake Science*,
1007 23:449-463, doi:10.1007/s11589-010-0744-3.

1008 Taira, A. (2001), Tectonic evolution of the Japanese island arc system. *Annu. Rev. Earth Planet. Sci.*,
1009 29:109-134.

1010 Tamaki, K., K. Suychiro, J. Allan, J.C. Ingle, Jr., K.A. Pisciotto (1992). Tectonic synthesis and
1011 implications of Japan Sea ODP Drilling, *Proc. Ocean Drilling Pgm, Scientific Results*, Vol. 127/128,
1012 Pt. 2, 1333-1348.

1013 Tang, Q. and Chen, L. (2008), Structure of the crust and uppermost mantle of the Yanshan Belt and
1014 adjacent regions at the northeastern boundary of the North China Craton from Rayleigh wave
1015 dispersion analysis. *Tectonophysics* 455: 43–52.

- 1016 Tatsumi, Y., Y. Otofujii, T. Matsuda, and S. Nohda (1989), Opening of the Sea of Japan back-arc basin by
1017 asthenospheric injection, *Tectonophysics*, 166: 317-329.
- 1018 Tian, A.Y., P. Han, and K.D. Xu (1992), The Mesozoic-Cenozoic east China rift system, *Tectonophysics*,
1019 208:341-363.
- 1020 Tian, Y., Zhao, D., Sun, R., Teng, J. (2009), Seismic imaging of the crust and upper mantle beneath the
1021 North China Craton, *Phys. Earth Planet. Int.*, 172: 169–182.
- 1022 Villasenor, A., M.H. Ritzwoller, A.L. Levshin, M.P. Barmin, E.R. Engdahl, W. Spakman, and J. Trampert
1023 (2001), Shear velocity structure of Central Eurasia from inversion of surface wave velocities, *Phys.*
1024 *Earth Planet. Int.*, 123(2-4), 169 - 184.
- 1025 Villaseñor, A., Y. Yang, M. H. Ritzwoller, and J. Gallart (2007), Ambient noise surface wave tomography
1026 of the Iberian Peninsula: Implications for shallow seismic structure, *Geophys. Res. Lett.*, 34,
1027 L11304, doi:10.1029/2007GL030164.
- 1028 Wu, F., J. Lin, A. Simon, X. Zhang, J. Yang (2005). Nature and significance of the Early Cretaceous giant
1029 igneous event in eastern China. *Earth and Planet. Sci. Lett.*, 233:103–119.
- 1030 Xu, Y.(2001). Thermotectonic destruction of the Archean lithospheric keel beneath eastern China:
1031 evidence, timing, and mechanism. *Physics and Chemistry of the Earth A*, 26: 747–757.
- 1032 Xu, Y. (2007), Diachronous lithospheric thinning of the North China Craton and formation of the
1033 Daxin'anling-Taihangshan gravity lineament, *Lithos*, 96: 281-298.

1034 Xu, P. and D. Zhao (2009), Upper-mantle velocity structure beneath the North China Craton: implications
1035 for lithospheric thinning, *Geophys. J. Int.*, 177: 1279-1283.

1036 Xu, Y.G., Chung, S.L., Ma, J.L., Shi, L.B. (2004). Contrasting Cenozoic lithospheric evolution and
1037 architecture in the eastern and western Sino-Korean craton: constraints from geochemistry of
1038 basalts and mantle xenoliths. *Journal of Geology*, 112: 593–605.

1039 Yang, Y., M. Ritzwoller, A. Levshin, and N. Shapiro (2007), Ambient noise Rayleigh wave tomography
1040 across Europe. *Geophys. J. Int.*, 168: 259-274.

1041 Yang, Y., and M. Ritzwoller (2008). Characteristics of ambient seismic noise as a source for surface wave
1042 tomography. *Geochem. Geophys. Geosyst.*, 9, Q02008, doi:10.1029/2007GC001814.

1043 Yang, Y., A. Li, and M. Ritzwoller (2008a). Crustal and uppermost mantle structure in southern Africa
1044 revealed from ambient noise and teleseismic tomography. *Geophys. J. Int.*, 174: 235-248.

1045 Yang, Y., M. Ritzwoller, F. Lin, M. Moschetti, and N. Shapiro (2008b), Structure of the crust and
1046 uppermost mantle beneath the western United States revealed by ambient noise and earthquake
1047 tomography, *J. Geophys. Res.*, 113, B12310, doi:10.1029/2008JB005833.

1048 Yang, Y., Y. Zheng, J. Chen, S. Shou, S. Ceylan, E. Sandvol, F. Rilmann, K. Priestley, T.M. Hearn, J.F. Ni,
1049 L.D. Brown, and M.H. Ritzwoller (2010), Rayleigh wave phase velocity maps of Tibet and the
1050 surrounding regions from ambient seismic noise tomography, *Geochem., Geophys., Geosys.*, 11(8),
1051 Q08010, doi:10.1029/2010GC003119.

- 1052 Yang, Y., M.H. Ritzwoller, Y. Zheng, A. Levshin, and Z. Xie (2011), A synoptic view of the distribution
1053 and connectivity of the mid-crustal low velocity zone beneath Tibet. Submitted to *J. Geophys. Res.*
- 1054 Yanovskaya, T.B., Kozhevnikov, V.M. (2003). 3D S-wave velocity pattern in the upper mantle beneath the
1055 continent of Asia from Rayleigh wave data. *Phys. Earth Planet. Int.* 138: 263–278.
- 1056 Yao, H., R. D. van der Hilst, and M. V. de Hoop (2006), Surface-wave array tomography in SE Tibet from
1057 ambient seismic noise and two-station analysis—I. Phase velocity maps, *Geophys. J. Int.*, 166:
1058 732–744, doi:10.1111/j.1365-246X.2006.03028.x.
- 1059 Yao, H., C. Beghein, and R. D. van der Hilst (2008), Surface wave array tomography in SE Tibet from
1060 ambient seismic noise and two-station analysis—II. Crustal and upper-mantle structure, *Geophys. J.*
1061 *Int.*, 173: 205–219, doi:10.1111/j.1365-246X.2007.03696.x.
- 1062 Yin, A. (2010), Cenozoic tectonic evolution of Asia: A preliminary synthesis, *Tectonophysics*, 488,
1063 293-325.
- 1064 Yin, A., and S. Nie (1993), An indentation model for the North and South China collision and the
1065 development of the Tan-Lu and Honam Fault Systems, eastern Asia, *Tectonics*, 12(4):801-813,
1066 doi:10.1029/93TC00313.
- 1067 Yin, A., and S. Nie (1996), A Phanerozoic palinspastic reconstruction of China and its neighboring
1068 regions, in *The Tectonic Evolution of Asia*, edited by A. Yin and T. M. Harrison, Cambridge Univ.
1069 Press, New York, pp. 442-285.

1070 Yoshizawa, K., K. Miyake, and K. Yomogida (2010), 3D upper mantle structure beneath Japan and its
1071 surrounding region from inter-station measurements of surface waves, *Phys. Earth Planet. Int.*,
1072 183:4-19.

1073 Zeng, X, and S. Ni (2010), A persistent localized microseismic source near the Kyushu Island, Japan,
1074 *Geophys. Res. Lett.*, 37, L24307, doi:10.1029/2010GL045774.

1075 Zeng, X, and S. Ni (2011), Correction to “A persistent localized microseismic source near the Kyushu
1076 Island, Japan”. *Geophys. Res. Lett.*, 38, L16320, doi:10.1029/2011GL048822.

1077 Zhang, P., Q. Deng, G. Zhang, J. Ma, W. Gan, W. Min, F. Mao, and Q. Wang (2003), Active tectonic
1078 blocks and strong earthquake in the continent of China. *Science in China D Series*, 46(s): 13-24.

1079 Zhao, D. (2009), Multiscale seismic tomography and mantle dynamics. *Gondwana Research*, 15:
1080 297–323.

1081 Zhao, D., S. Maruyama, and S. Omori (2007). Mantle dynamics of Western Pacific and East Asia: Insight
1082 from seismic tomography and mineral physics, *Gond. Res.*, 11:120-131.

1083 Zhao, G.C., Sun, M.,Wilde, S.A., Li, S.Z. (2005). Late Archean to Paleoproterozoic evolution of the
1084 North China Craton: key issues revisited. *Precambrian Res.*, 136: 177–202.

1085 Zhao, L. T. Zheng, and G. Lu (2008), Insight into craton evolution: Constraints from shear wave splitting
1086 in the North China Craton, *Phys. Earth Planet. Int.*, 168:153-162.

1087 Zheng, S., X. Sun, X. Song, Y. Yang, and M.H. Ritzwoller (2008), Surface wave tomography of China
1088 from ambient seismic noise, *Geochem. Geophys. Geosyst.*, 9, Q0502, doi:10.1029/2008GC001981.

1089 Zheng, T., L. Chen, L. Zhao, W. Xu, and R. Zhu (2006), Crust–mantle structure difference across the
1090 gravity gradient zone in North China Craton: Seismic image of the thinned continental crust, *Phys.*
1091 *Earth Planet. Int.*, 159: 43-58.

1092 Zheng, X. F., Z. X. Yao, J. H. Liang, and J. Zheng (2010a), The role played and opportunities provided by
1093 IGP DMC of China National Seismic Network in Wenchuan earthquake disaster relief and
1094 researches, *Bull. Seismol. Soc. Am.*, 100(5B): 2866-2872.

1095 Zheng, Y., Y. Yang, M.H. Ritzwoller, X. Zheng, X. Xiong, Z. Li (2010b), Crustal structure of the
1096 northeastern Tibetan Plateau, the Ordos Block, and the Sichuan Basin from ambient noise
1097 tomography, *Earthquake Science*, 3:465-476, doi:10.1007/s11589-010-0745-3.

1098 Zhou, L., J. Xie, W. Shen, Y. Zheng, Y. Yang, H. Shi, and M.H. Ritzwoller (2011), Ambient noise surface
1099 wave tomography of South China, submitted to *Geophys. J. Int.*.

1100 Zhou, R.M., B.W. Stump, R.B. Herrmann, Z. X. Yang, and Y. T. Chen (2009), Teleseismic receiver
1101 function and surface-wave study of velocity structure beneath the Yanqing-Huailai Basin Northwest
1102 of Beijing, *Bull. Seism. Soc. Am.*, 99(3):1937-1952.

1103

1104

1105 **Table 1:** Number of measurements retained after each step in data quality control.

1106

Period (s)	Step A	Step B	Step C	Step D	Step E (phase)	Step E(group)
10	20816	14563	14492	13567	11053	10180
14	31356	25770	25740	24082	22606	21593
20	33573	33573	33564	31555	29170	29515
25	28990	28990	28982	27398	25209	25161
30	25495	25495	25491	24210	22096	21623
35	21976	21976	21972	20985	18903	18247
40	18172	18172	18165	17488	15303	14688
45	14503	14503	14495	14031	11810	11352

1107

1108

1109

1110

1111 **Figure Captions**

1112 **Figure 1.** The broadband seismic stations used in this study. The blue triangles are the Chinese
1113 provincial broadband seismic stations (CEArray), the red triangles are the F-Net long
1114 period stations and the red squares are other broadband stations, mostly from the IRIS
1115 GSN. The black box defines the study region.

1116 **Figure 2.** The geological setting of this study. Solid red lines mark the boundaries of the
1117 Sino-Korean Craton (SKC), the solid white line identifies the North-South Gravity
1118 Lineament (NSGL), the dashed black line is the Tancheng-Lujiang fault (TLF), and
1119 black lines outline blocks and tectonic boundaries (Zhang, et al., 2003). The North
1120 China Craton is the part of the SKC in China, and is sub-divided by dashed red lines into
1121 western, central, and eastern parts. Feature names are abbreviated as follows: PS:
1122 Phillipine Sea Plate, OK: Okhotsk Plate, NCP: North China Platform, YB: Yangtze
1123 Block, SLB: Songliao Basin, JB: Japan Basin, TB: Yamato Basin, TB: Tsushima Basin,
1124 SB: Sichuan Basin, OR: Ordos Block, BH: Bohai Bay, GXAR: Great Xing'an Range,
1125 LXAR: Lesser Xing'an Range, CBM: Changbai Mountain Range, YSM: Yinshan
1126 Mountain Range, ESYS: East Shandong Yellow Sea Block, NEFB: Northeast Asian
1127 Fold Belt, NSGL: North-South Gravity Lineament, and HB: Huabei Basin. Red dots
1128 with letters mark locations of the dispersion curves and 1D shear velocity profiles shown
1129 in **Figs. 11** and **12**.

1130 **Figure 3.** Record sections of cross-correlations obtained from two years of waveform data (a)
1131 between Chinese provincial network stations, (b) between F-Net stations, and (c)
1132 between the Chinese stations and F-Net stations. The white dots identify the expected
1133 arrival times for the Kyushu persistent microseism.

1134 **Figure 4.** Process to locate the Kyushu microseism. (a) Top Panel: raw cross-correlation (CC)
1135 between station SSE and INCN (blue triangles in (b)). Bottom Panel: The envelope
1136 function of the CC filtered between 10 and 12 sec period. The Kyushu microseismic
1137 signal arrives at ~130 sec. (b) The migrated hyperbola from the envelope function in (a),
1138 normalized so its maximum value is 1. (c) Paths used to locate the Kyushu microseism
1139 are plotted with black lines. We use all paths associated with stations SSE and INCN
1140 (yellow triangles). (d) Stack of migrated hyperbolas to locate the Kyushu microseism.
1141 Blue circle is the location of *Zeng and Ni* [2010].

1142 **Figure 5.** Cross-correlations and corresponding frequency-time diagrams illustrating the effect of
1143 the persistent Kyushu microseism. (a) Cross-correlation between stations HXQ of
1144 CEArray and STM of F-Net, where the expected arrival time of the signal from the
1145 Kyushu microseism (marked “Kyushu”) is close to the arrival time of the surface wave
1146 (marked “Surface”) on the negative lag component. (b) Example waveform disturbed by
1147 the Kyushu microseism: symmetric component cross-correlation in which the positive
1148 and negative components in (a) are averaged. (c) Example waveform undisturbed by the

1149 Kyushu microseism: positive component of the cross-correlation in (a). (d) & (e)
1150 Frequency-time (group velocity) diagrams from (b) and (c), respectively. (f) Comparison
1151 between the group velocity curves of cross-correlations shown in (b) and (c). Red
1152 triangles and stars are the phase and the group velocity curves from disturbed signal.
1153 Blue symbols show the group and phase velocity curves of the undisturbed signal.

1154 **Figure 6.** Resolution estimates at periods of 16 and 35 sec, presented in units of km and defined
1155 as twice the standard deviation of a 2-D Gaussian fit to the resolution surface at each
1156 geographic node [Barmin *et al.*, 2001]. The black box shows the region of study.

1157 **Figure 7.** Misfit histograms at periods 14, 20, 30, and 40 sec, respectively. The top figures show
1158 the group velocity misfit and the lower figures are the phase velocity misfits. The
1159 standard deviations are shown on each panel.

1160 **Figure 8.** Group velocity maps at periods of 12, 20, 30, and 40 sec. Group velocities are plotted
1161 as perturbations relative to the average velocity (U_0) within the 400 km resolution
1162 contour and the thick white line is the 100 km resolution contour. Other lines show
1163 tectonic and geological boundaries identified in [Fig. 2](#).

1164 **Figure 9.** Same as [Fig. 8](#), but for phase velocity maps at periods of 12, 20, 30 and 40 sec.

1165 **Figure 10.** Rayleigh wave phase (solid lines) and group (dashed lines) velocity sensitivity
1166 kernels for 10 sec (red lines) and 40 sec (black lines) period. (a) Kernels are based on

1167 our 3D model in the Sea of Japan (point H, Fig. 2). (b) Kernels are based on our 3D
1168 model in the North China Craton (point B, Fig. 2). The horizontal black lines denote
1169 local Moho depth at each point.

1170 **Figure 11.** Phase and group velocity observations at the eight locations identified with letters in
1171 Fig. 2, presented with error bars intended to be 1σ . The dispersion curves are predicted
1172 by the center of the ensemble of models shown in Fig. 12 for each location, with red
1173 lined being phase velocity and blue lines group velocity. The RMS misfits are calculated
1174 by equation (1).

1175 **Figure 12.** Shear wave (V_{sv}) velocity profiles at the eight selected locations identified with
1176 letters in Fig. 2 constructed to fit the corresponding dispersion curves shown in Fig. 11.
1177 The gray corridor is the 2σ (standard deviation) uncertainty and the dashed lines indicate
1178 Moho depth.

1179 **Figure 13.** Comparison between inversions performed in the Sea of Japan (point H, Fig. 2) using
1180 data from Fig. 11h with two starting models identified with blue lines: (a) Moho at 8 km
1181 and (b) Moho at 20 km. Horizontal lines mark the median Moho depths. The resulting
1182 ensembles of models are quite similar, with differences within model uncertainties.

1183 **Figure 14.** Four horizontal depth slices through the 3-D V_{sv} model: (a) in the lower crust at a
1184 depth of 80% of Moho depth, (b) 40 km, (c) 60 km, and (d) 80 km depth. Color bars

1185 beneath each panel give the range of shear wave speeds in km/s.

1186 **Figure 15.** (a) Estimated crustal thickness and (b) 1σ uncertainty in crustal thickness, both in km.

1187 The lines A-A', B-B', etc. in (a) are the location of the vertical profiles shown in Fig. 17.

1188 (c) Shear velocity jump across Moho (km/s) and (d) 1σ uncertainty in the shear velocity

1189 jump across Moho, also in km/s.

1190 **Figure 16.** Uncertainty (1σ) in V_{sv} at the four depths shown in Fig. 14. Uncertainties are in

1191 km/s.

1192 **Figure 17.** Four vertical profiles through the 3-D model along the lines shown in Fig. 15a.

1193 Crustal velocities are presented using an absolute scale and mantle velocities are defined

1194 relative to 4.35 km/s.

1195 **Figure 18.** (a) Blow-up of part of Fig. 15a, showing crustal thickness across the Sea of Japan (in

1196 km). Contours of bathymetry are over-plotted in increments of 1 km to illustrate the

1197 anti-correlation between crustal thickness and seafloor depth. (b) Plot of seafloor depth

1198 versus solid crustal thickness (crustal thickness minus ocean depth) with values on a

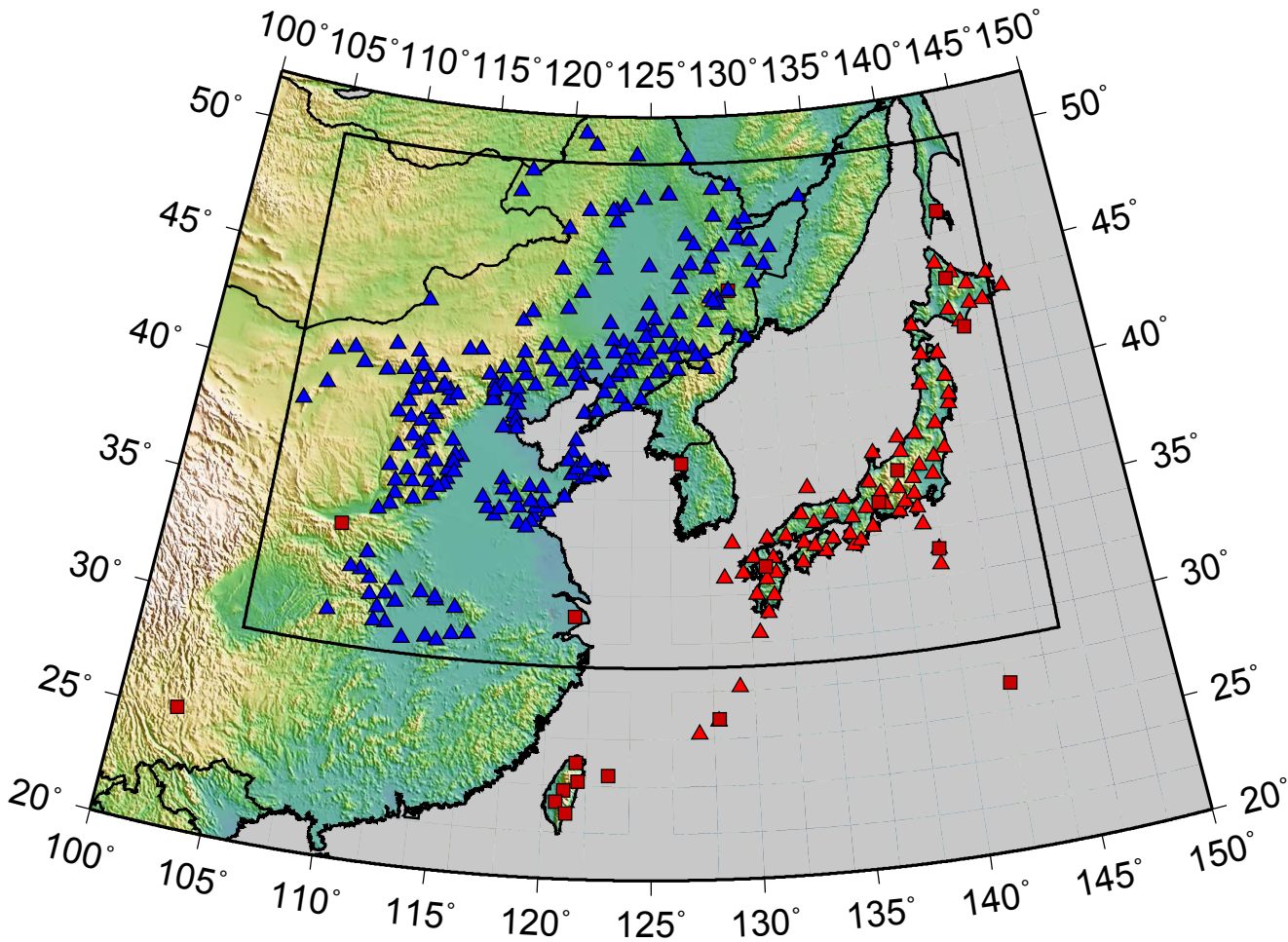
1199 $0.5^\circ \times 0.5^\circ$ grid across the Sea of Japan shown as blue dots. The solid red line is the

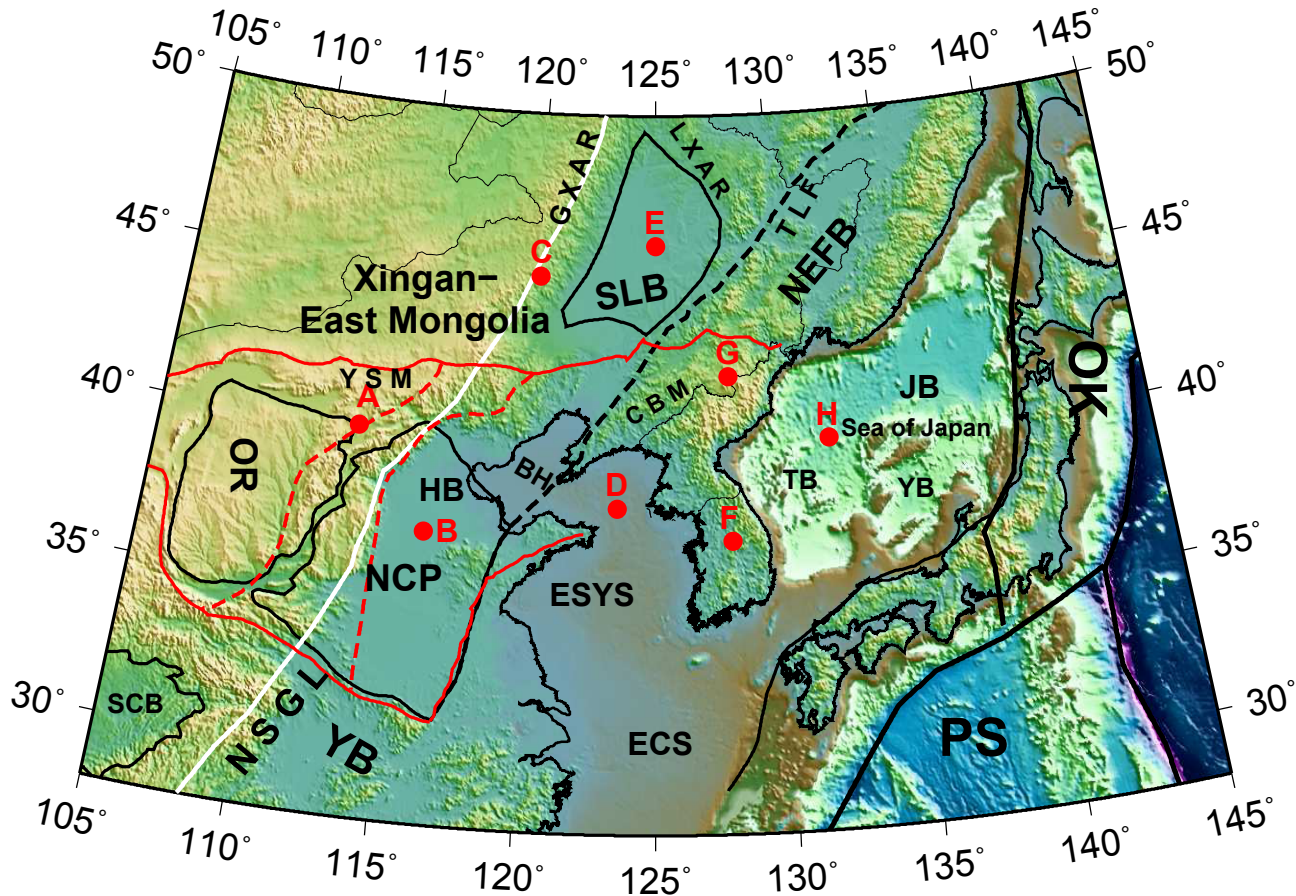
1200 least-squares fit line in which seafloor depth is the dependent variable and the dashed

1201 red line is the fit in which crustal thickness is the dependent variable.

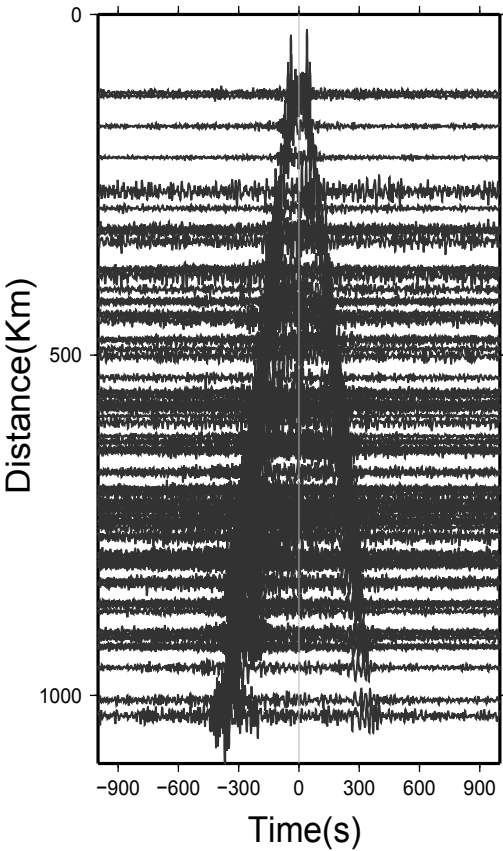
1202 **Figure 19.** Simplified representation of the 3D model in the upper mantle, showing the

1203 distribution of low velocities at 80 km depth with velocity intervals: red: $V_{sv} \leq 4.25$
1204 km/sec, blue: $4.25 < V_{sv} \leq 4.35$ km/s. The red contour identifies the “Y-shaped”
1205 anomaly that underlies the Sea of Japan and parts of northeastern Asia believed to arise
1206 from slab dehydration at several depths overlying the stagnant slab. The blue region
1207 surrounding the red contour is the large area of the uppermost mantle affected by
1208 back-arc spreading. The blue contour within the North China Craton identifies the
1209 “horseshoe” shaped anomaly that flanks the eastern North China Craton, believed to
1210 result from intense tectonothermal modification that may have reached as high as the
1211 base of the crust.

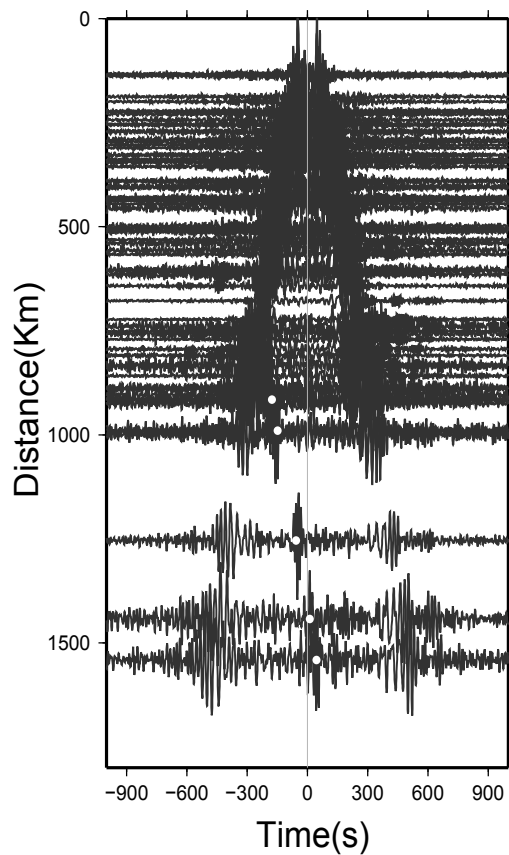




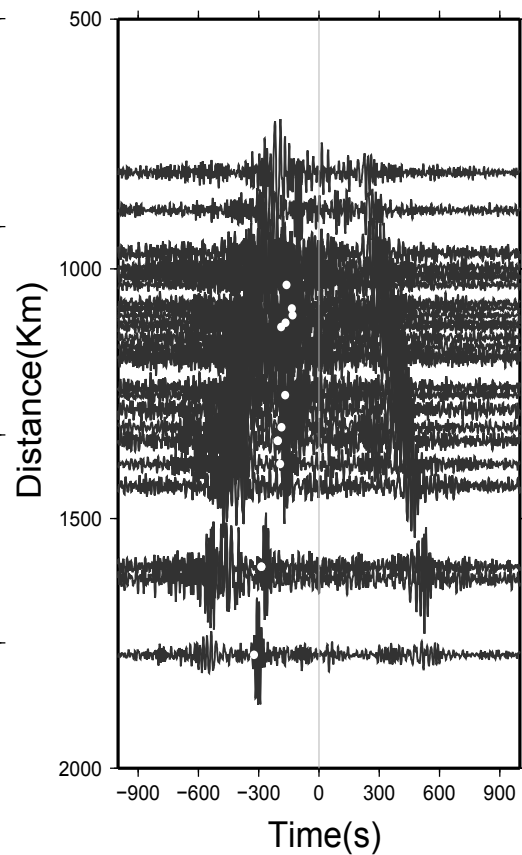
(a) NEH-CH



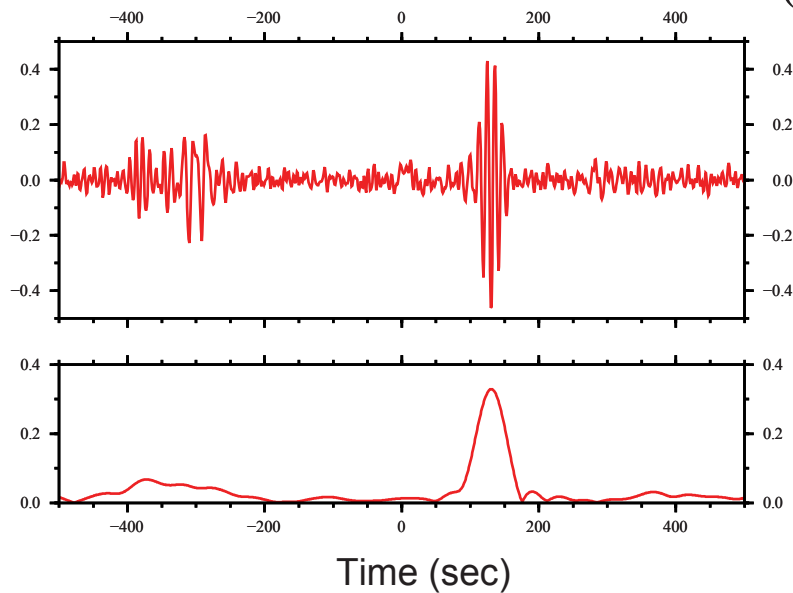
(b) WJM-FN



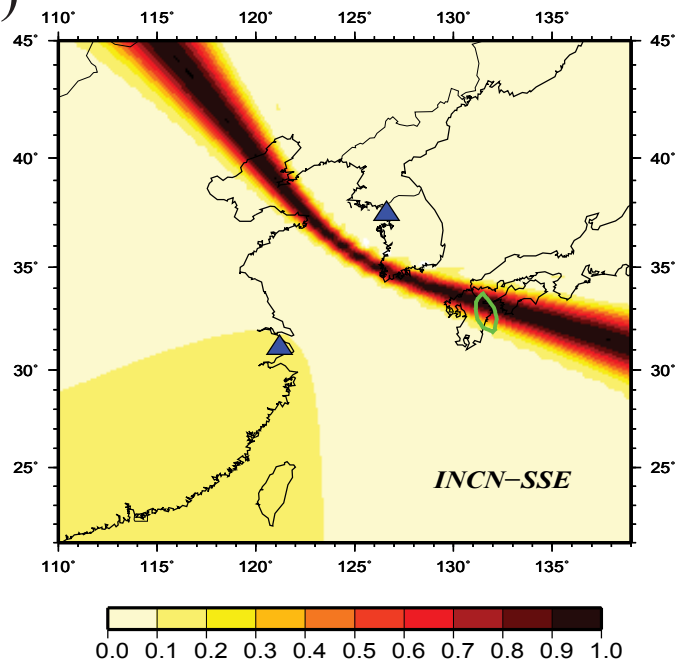
(c) WJM-CH



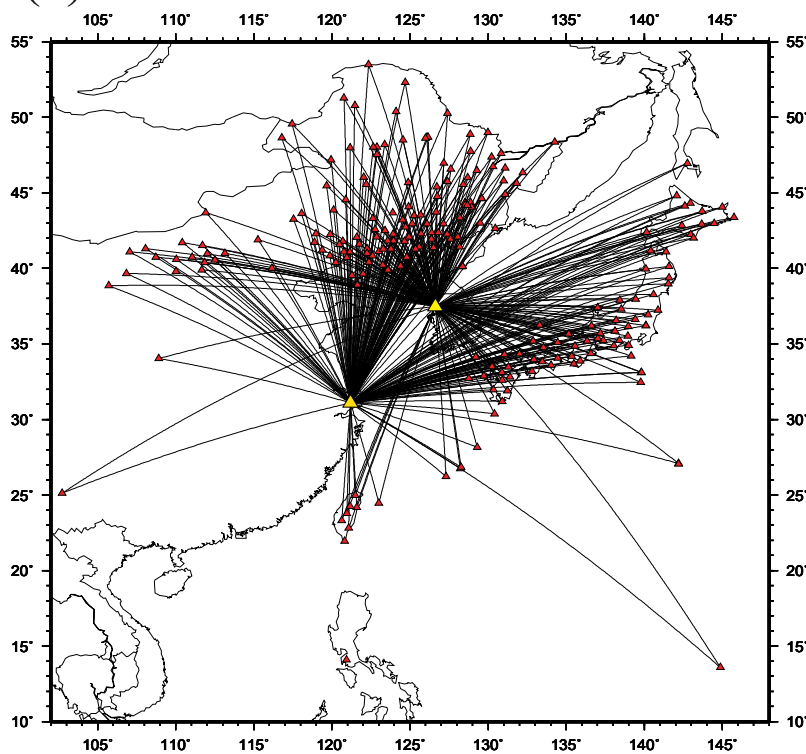
(a)



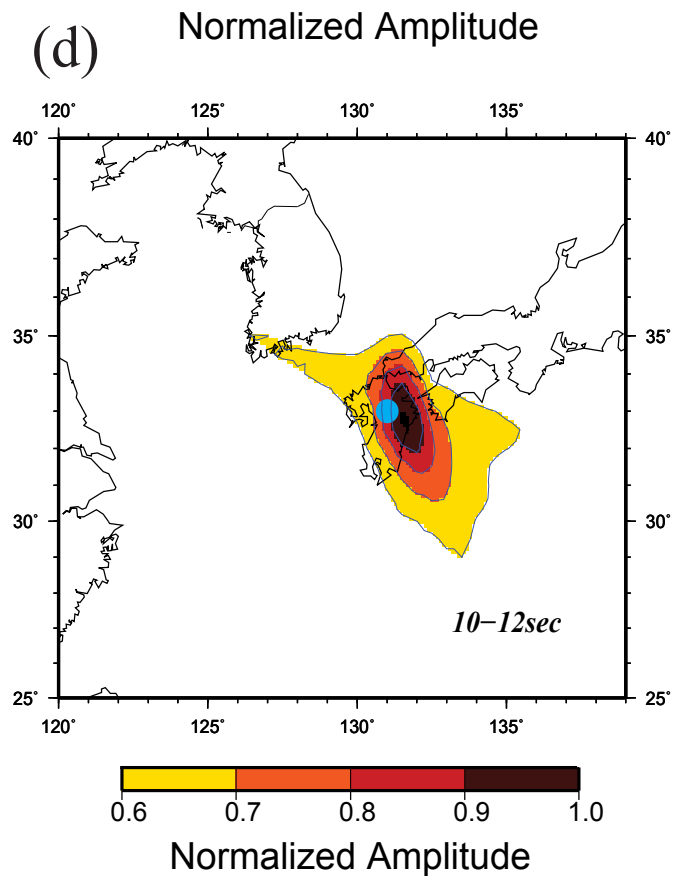
(b)

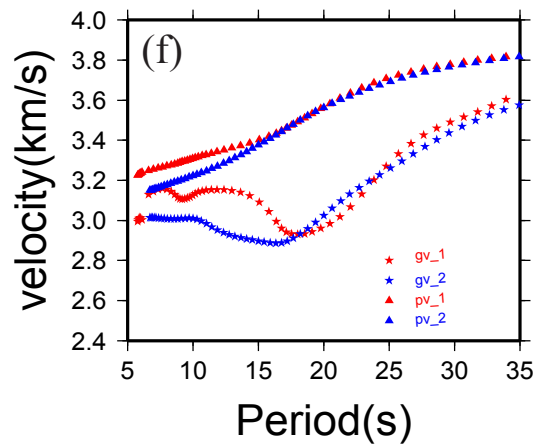
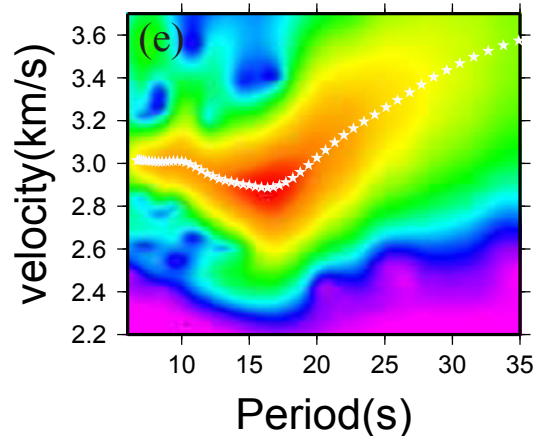
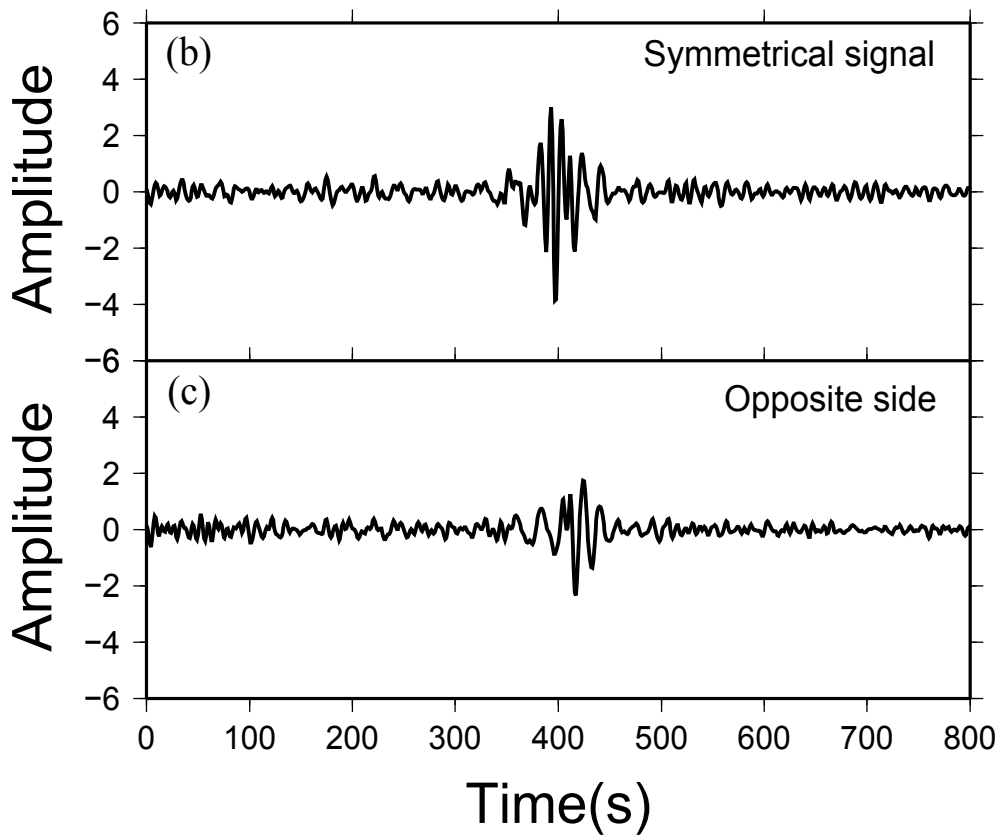
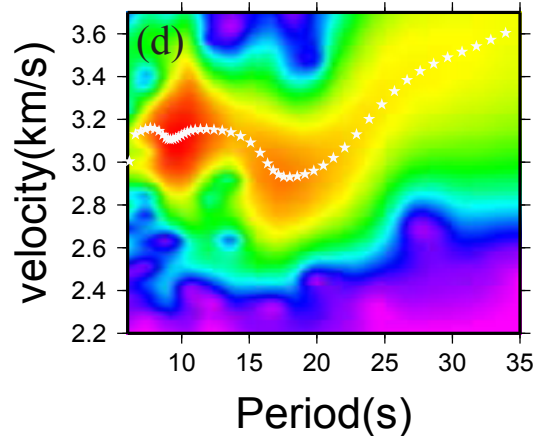
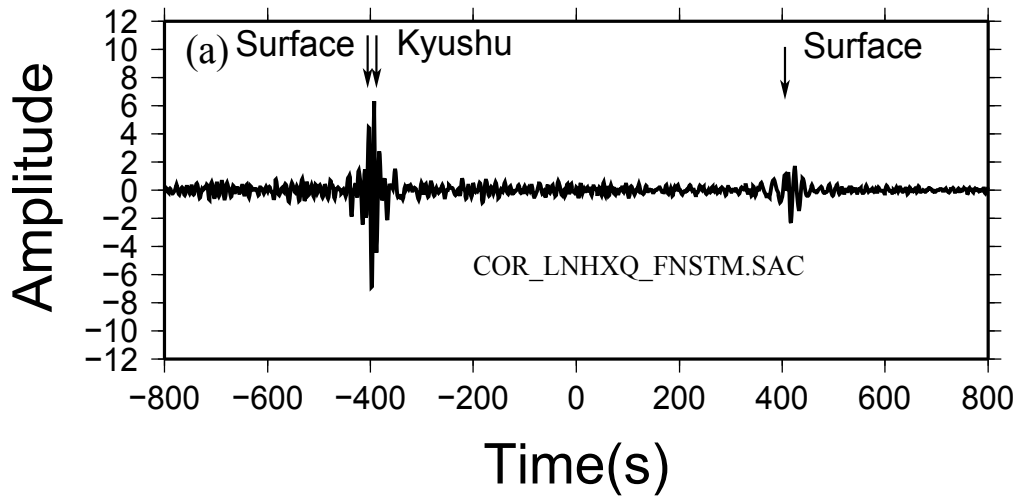


(c)

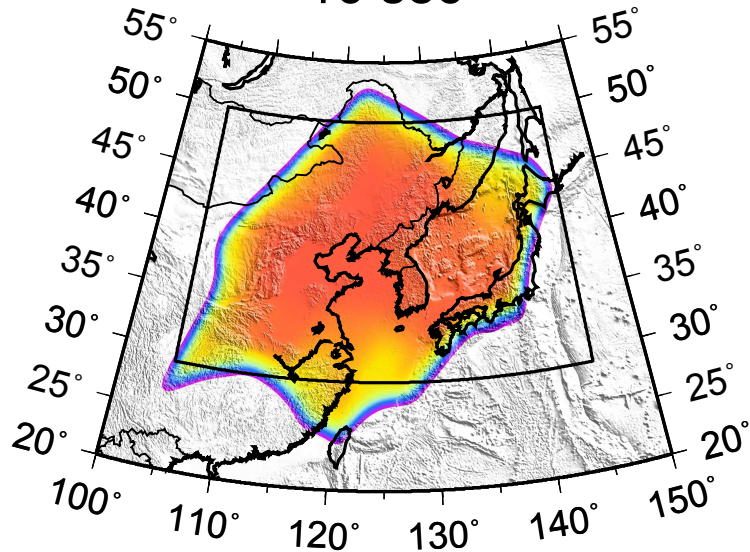


(d)

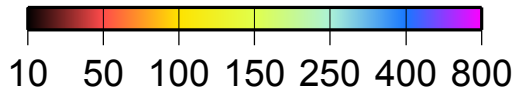
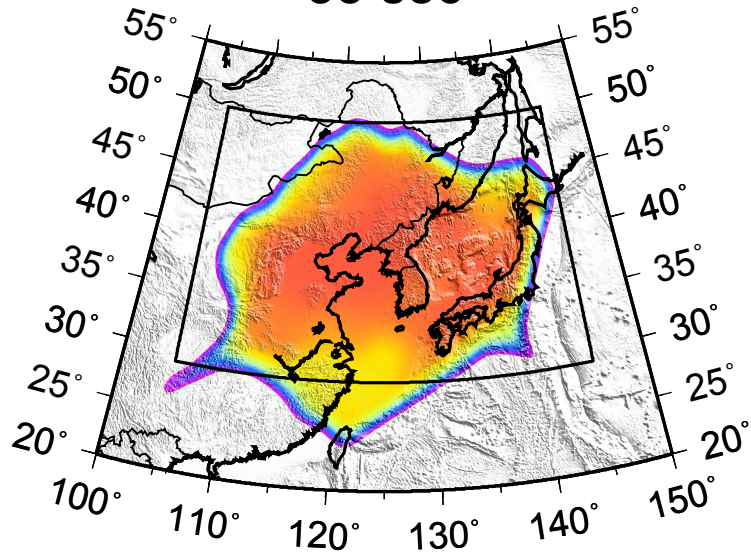




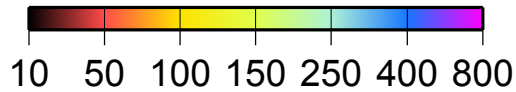
16 sec



35 sec

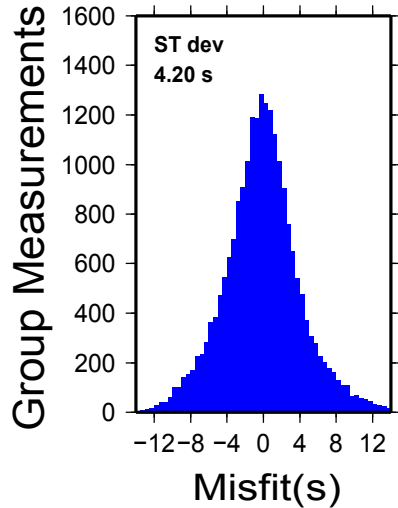


Resolution(km)

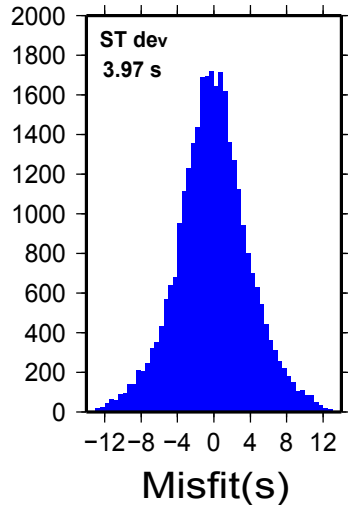


Resolution(km)

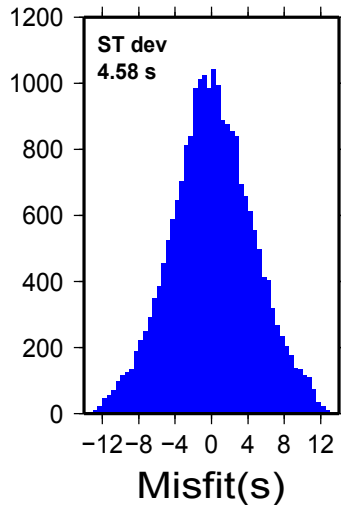
14 Sec



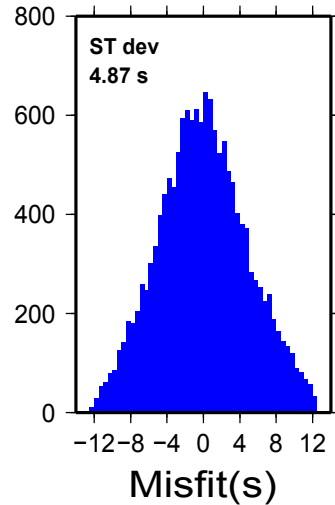
20 Sec



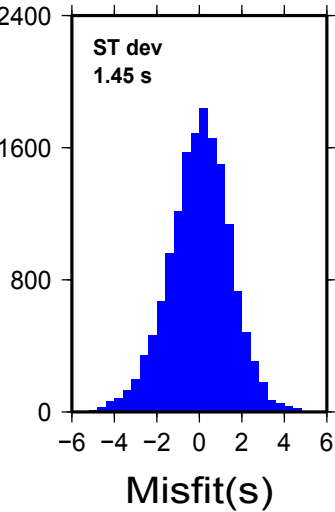
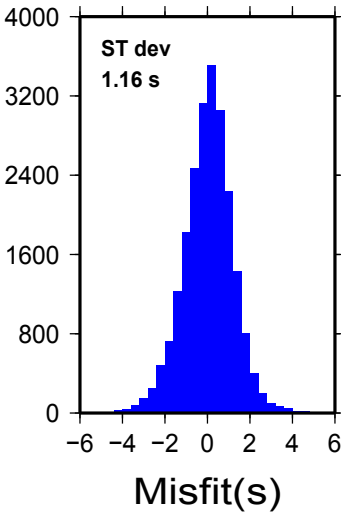
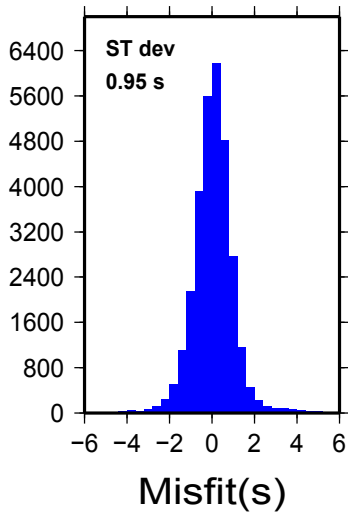
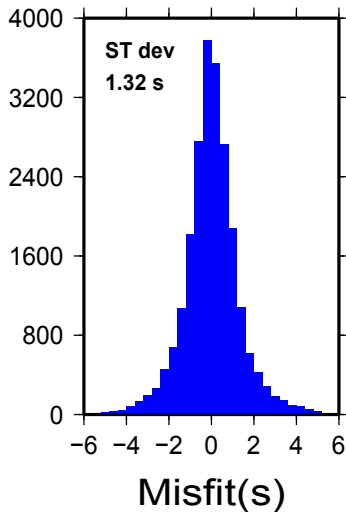
30 Sec



40 Sec

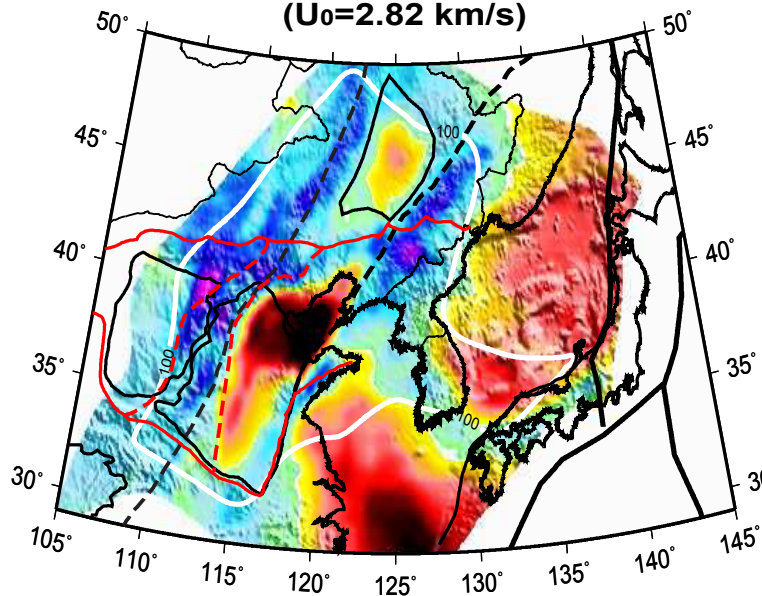


Phase Measurements



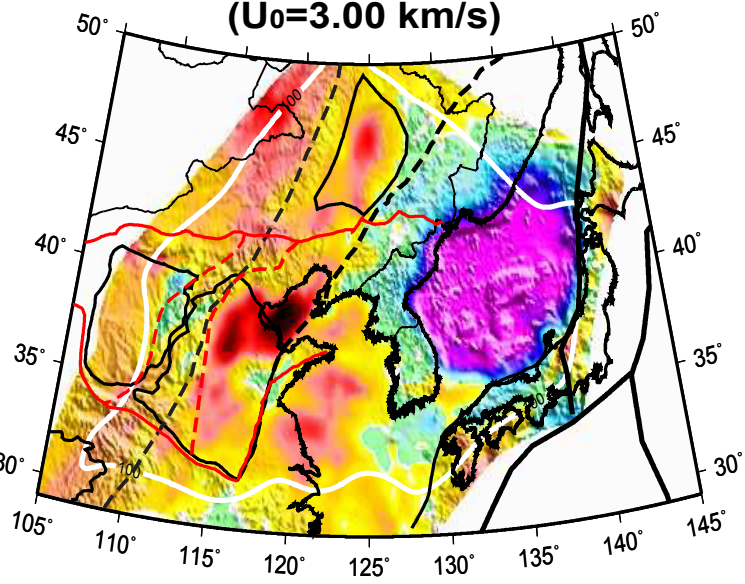
12 Sec

($U_0=2.82$ km/s)



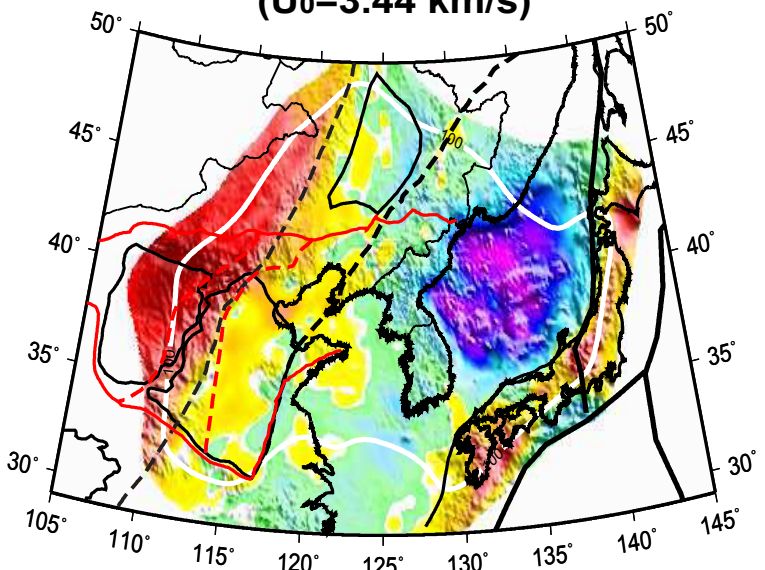
20 Sec

($U_0=3.00$ km/s)



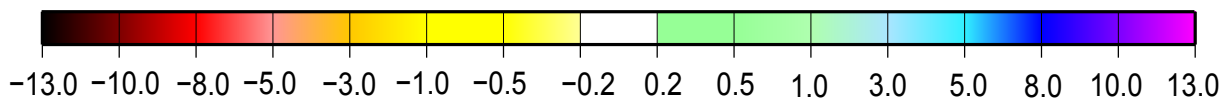
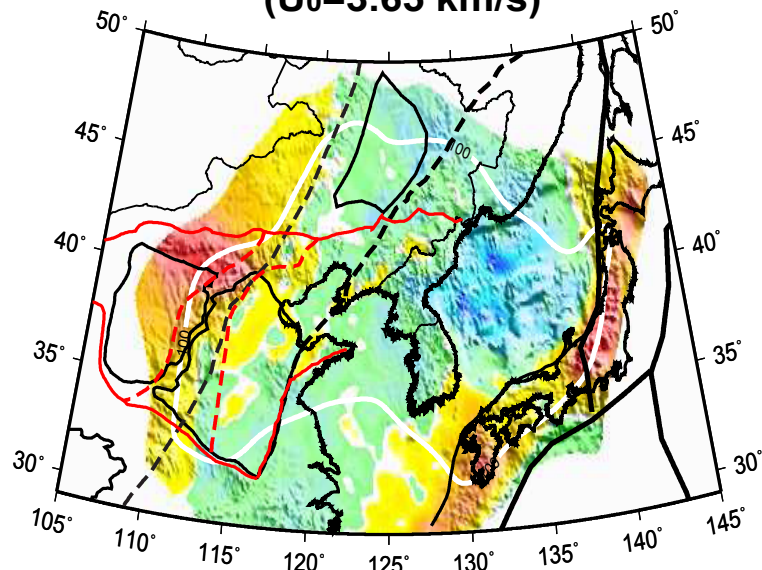
30 Sec

($U_0=3.44$ km/s)



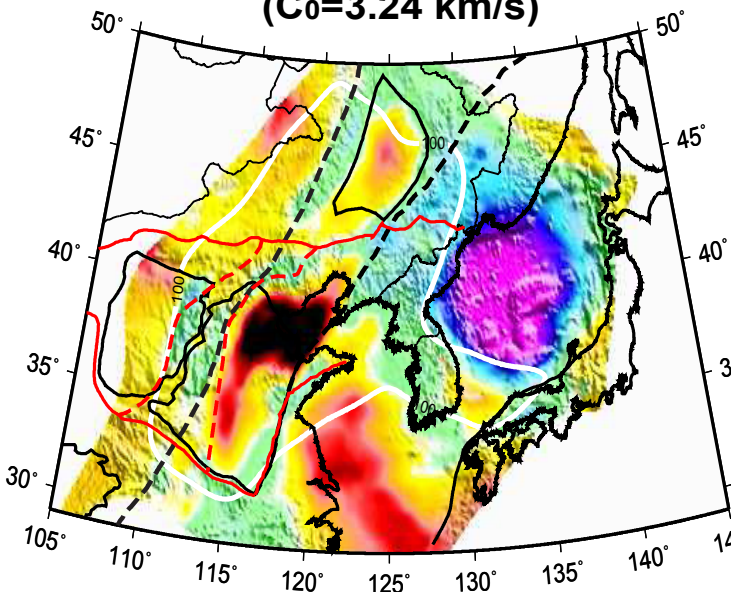
40 Sec

($U_0=3.65$ km/s)

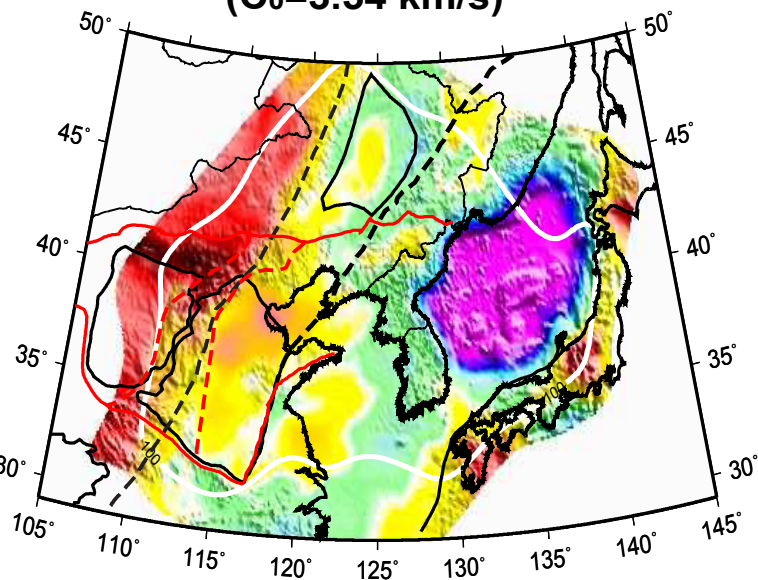


Group Velocity Perturbation (%)

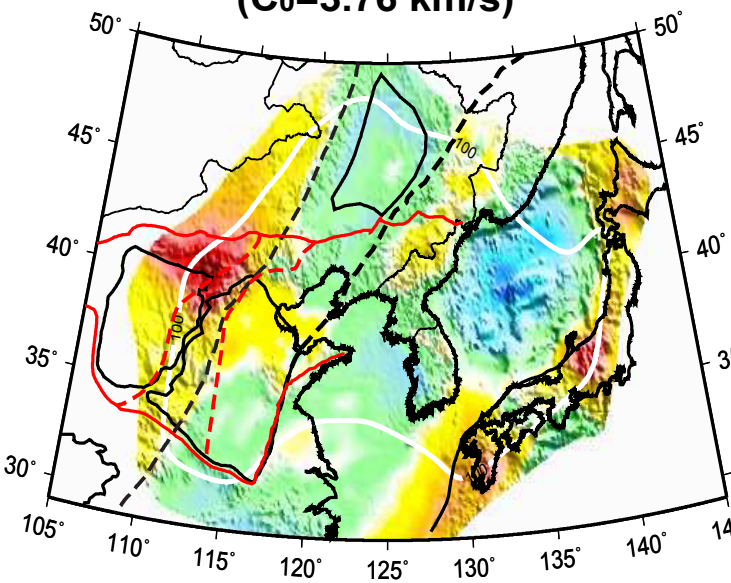
12 Sec
($C_0=3.24$ km/s)



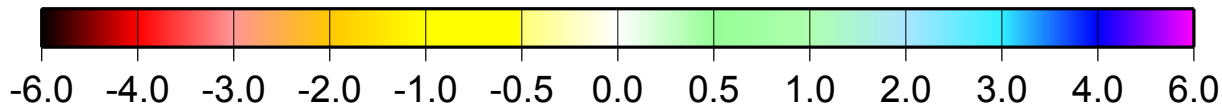
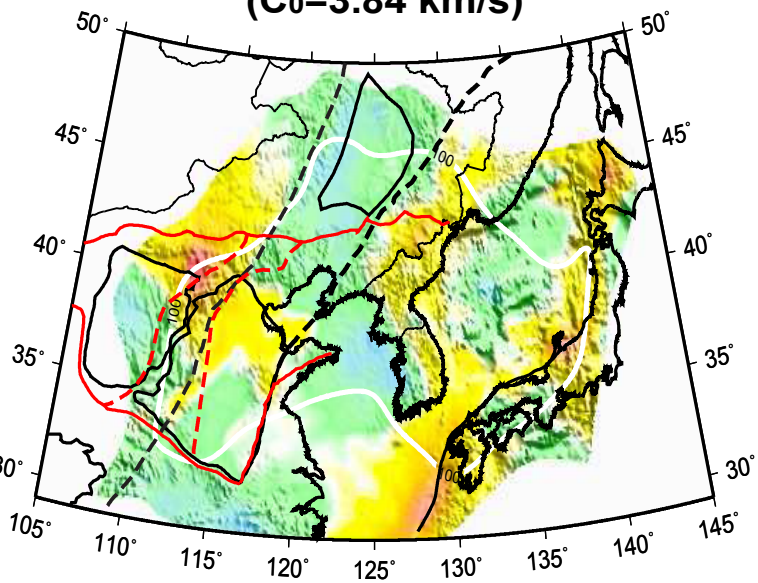
20 Sec
($C_0=3.54$ km/s)



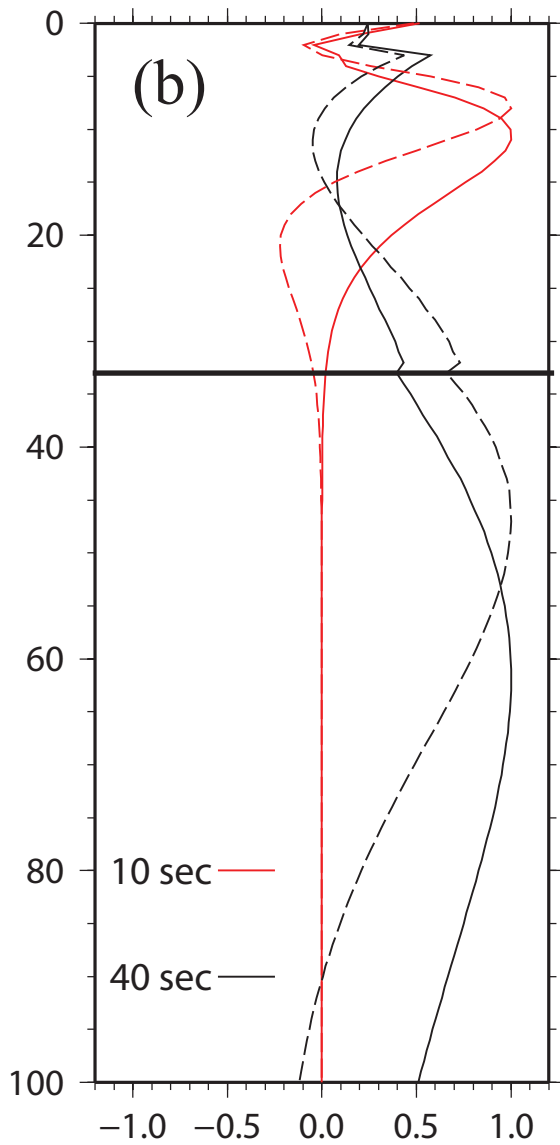
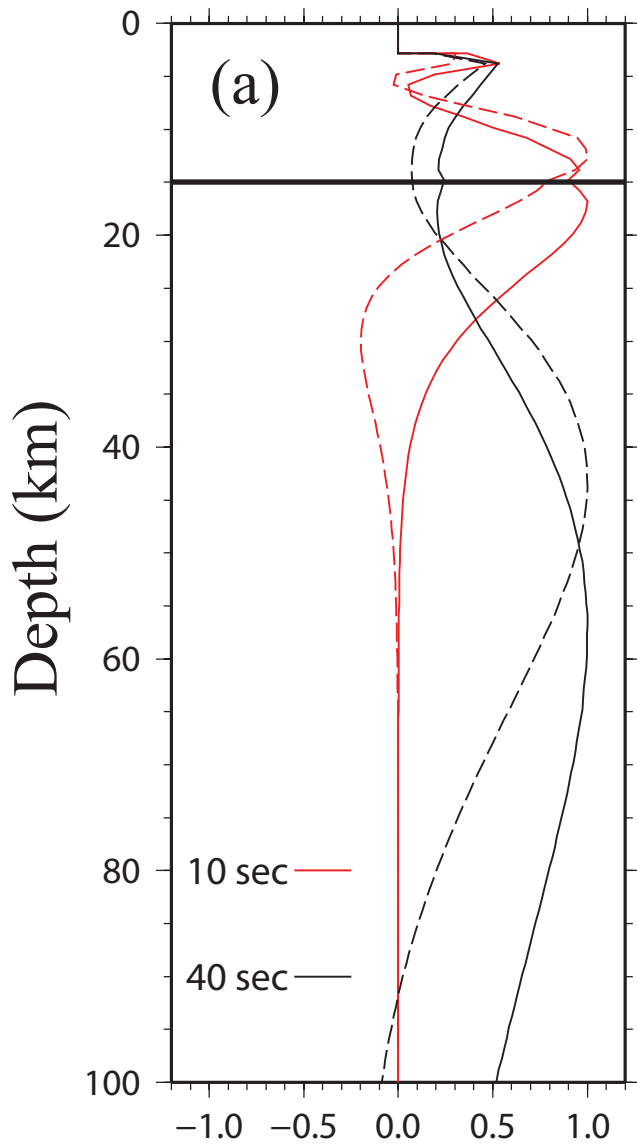
30 Sec
($C_0=3.76$ km/s)

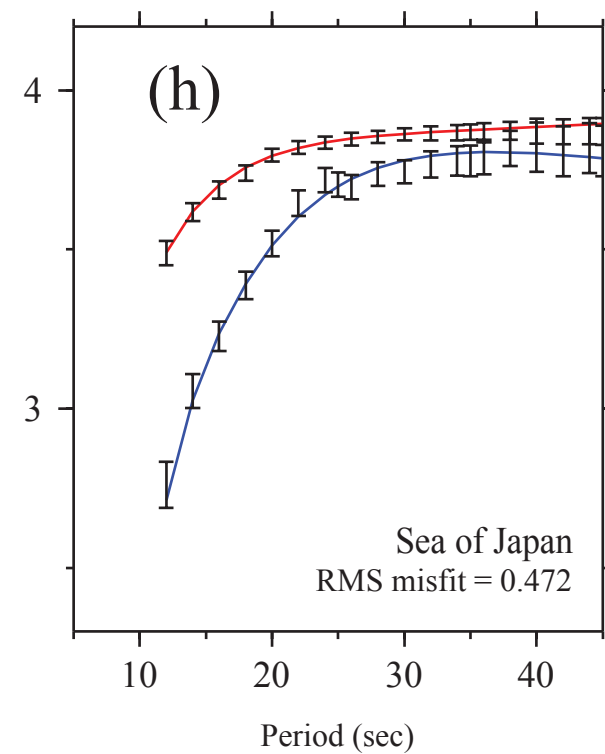
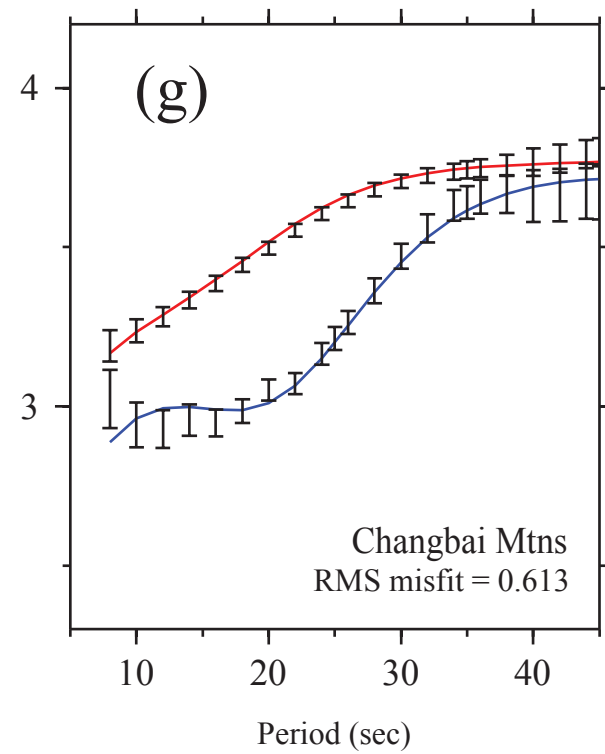
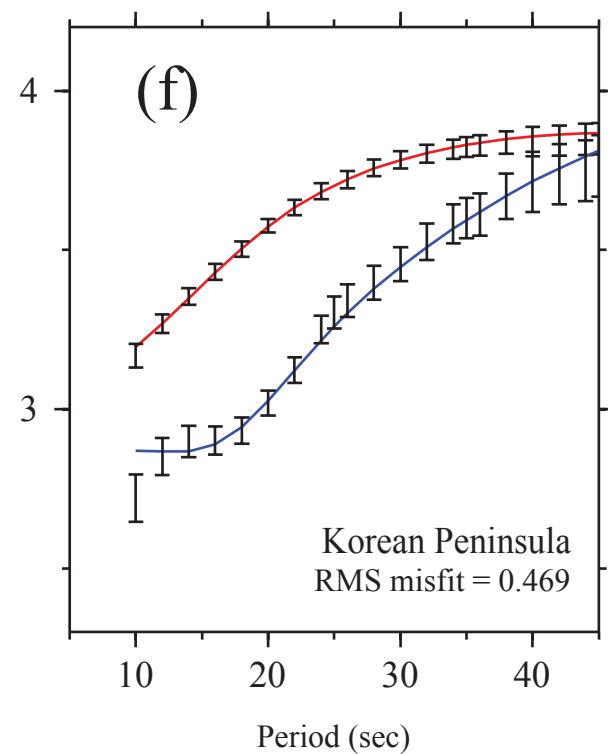
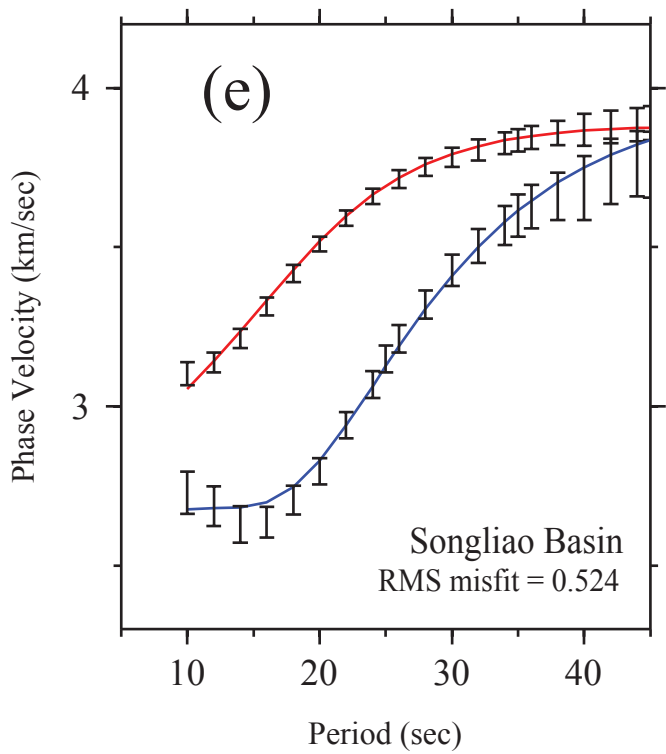
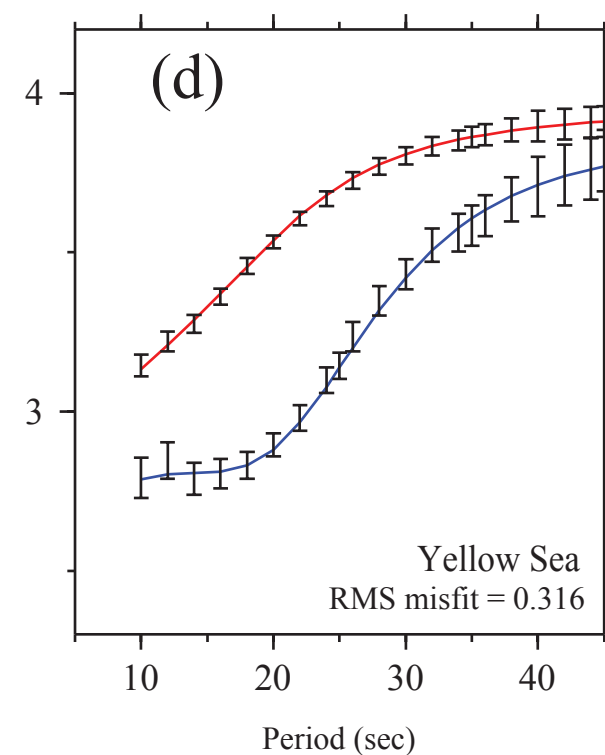
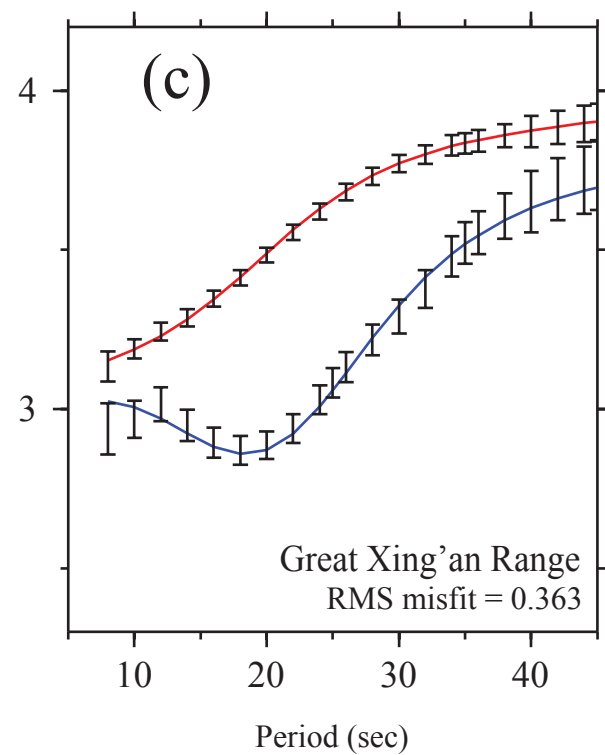
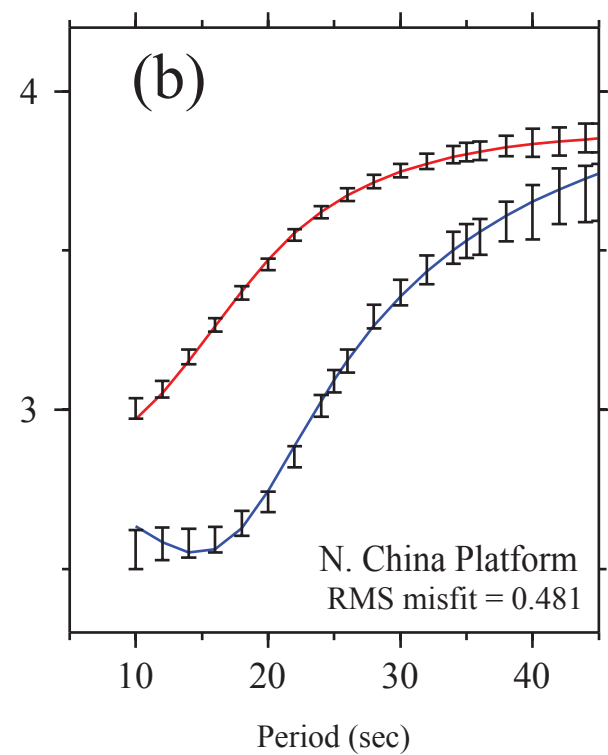
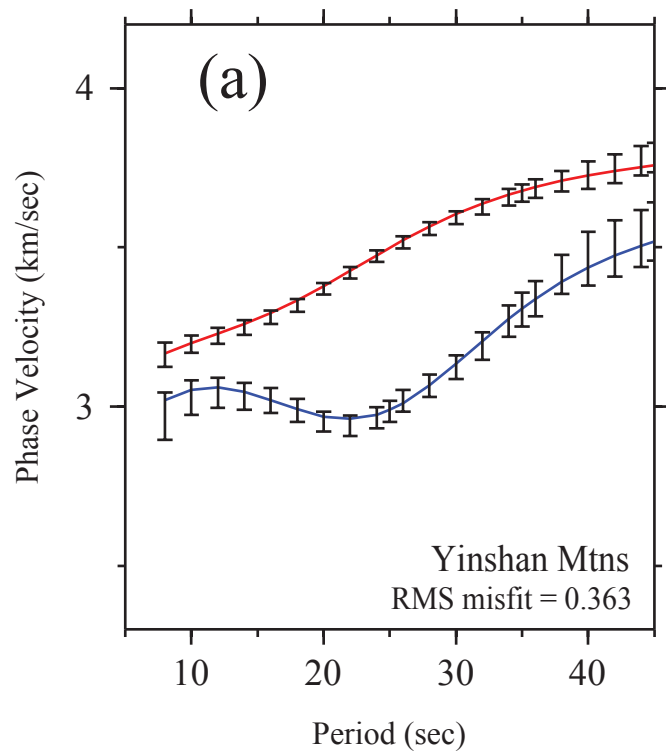


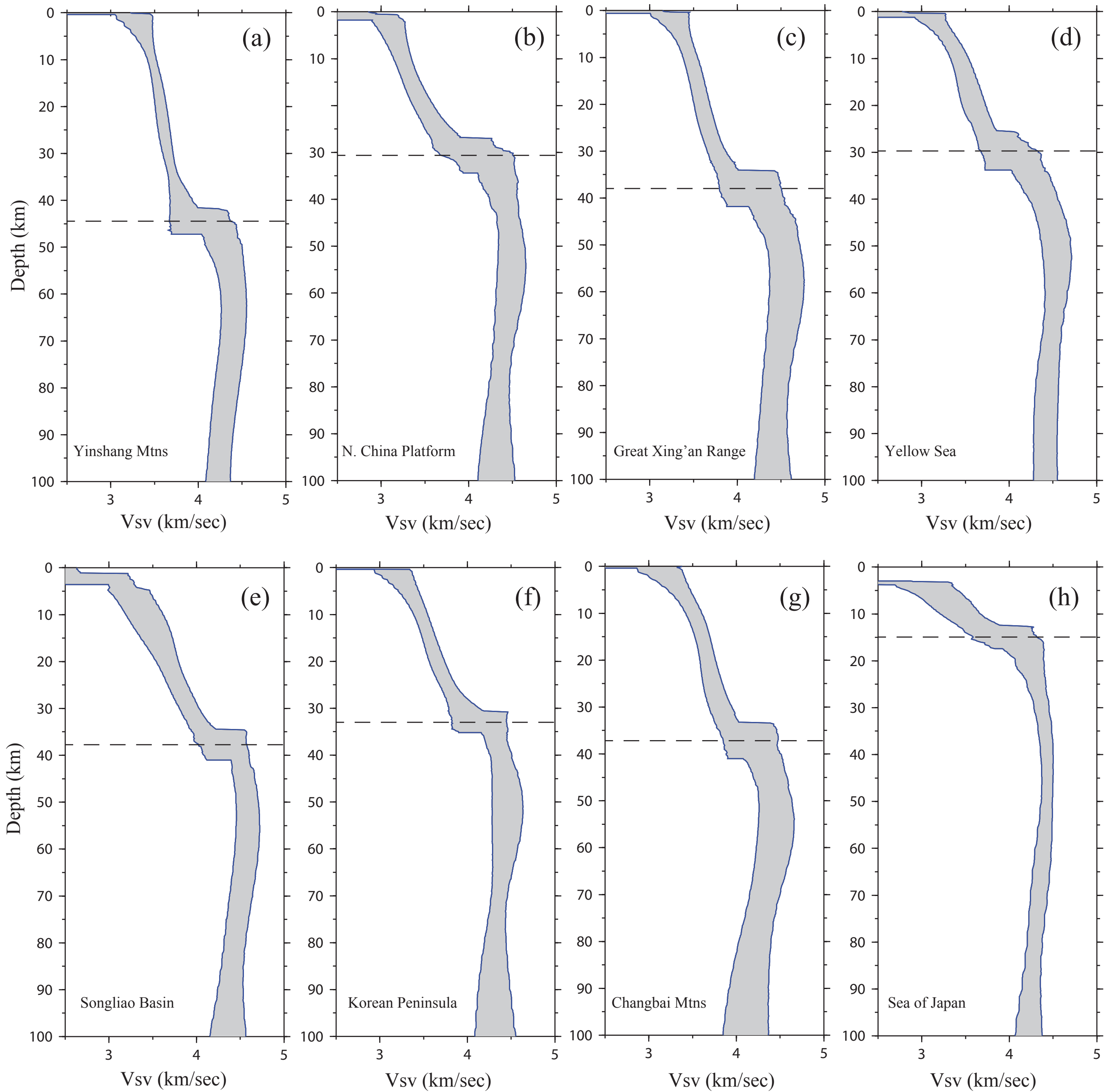
40 Sec
($C_0=3.84$ km/s)

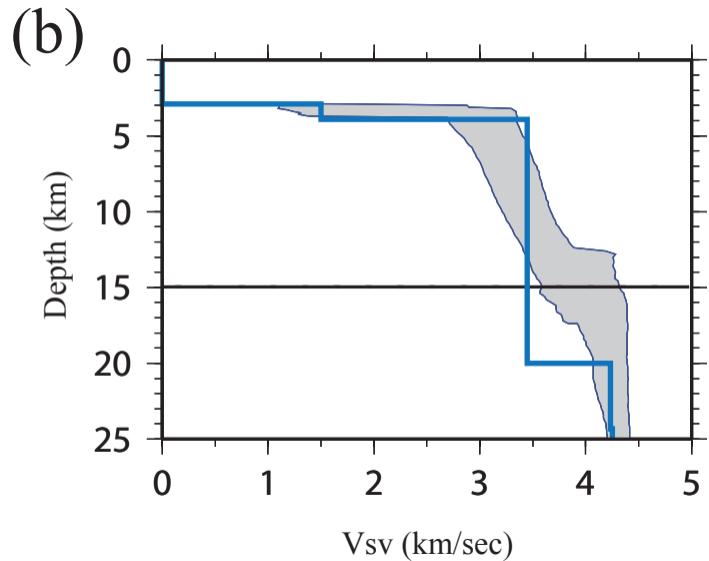
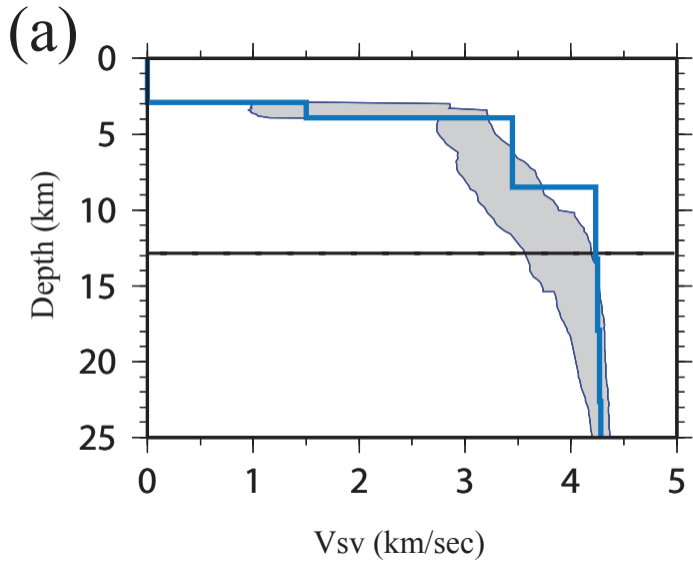


Phase Velocity Perturbation (%)

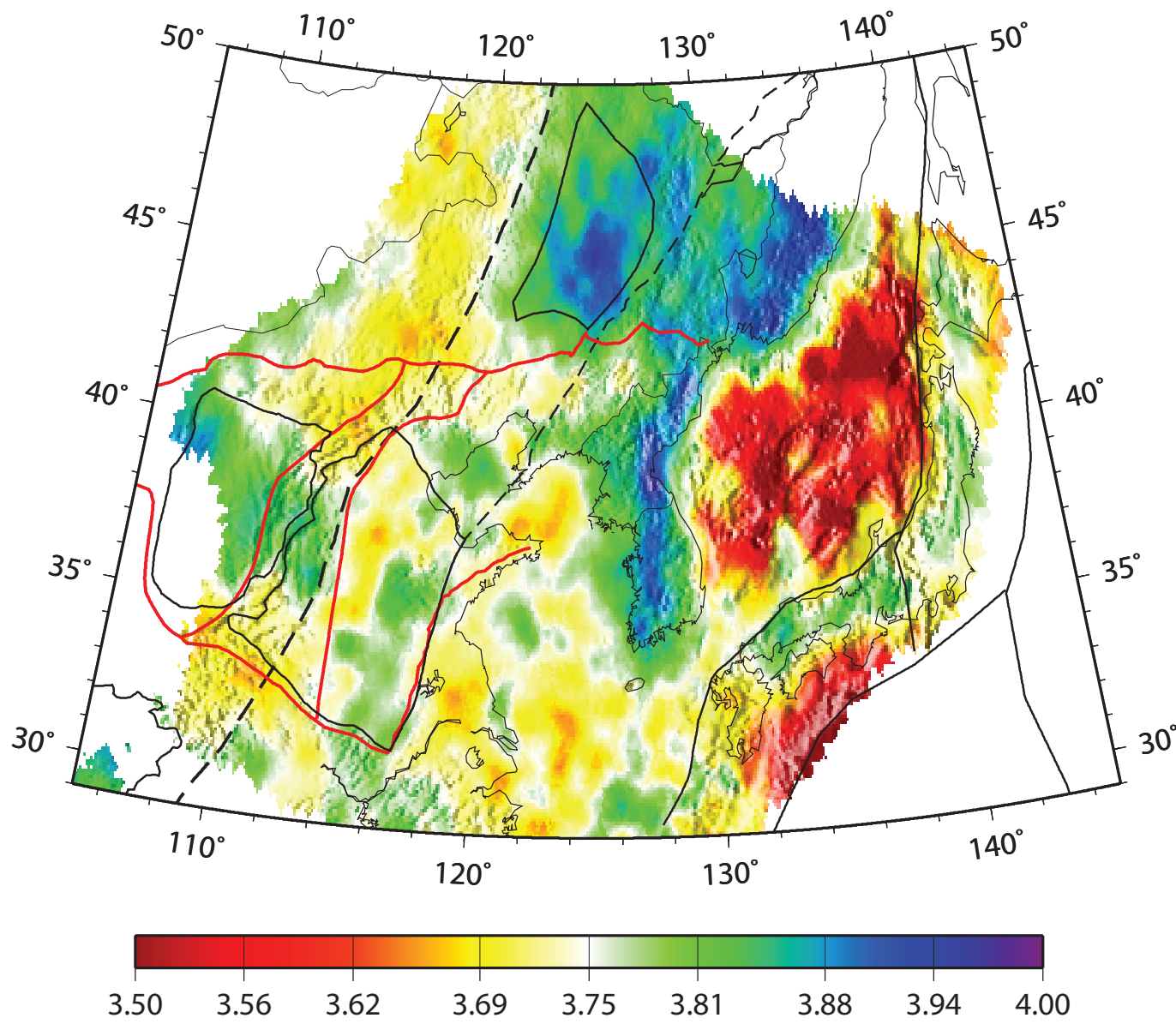




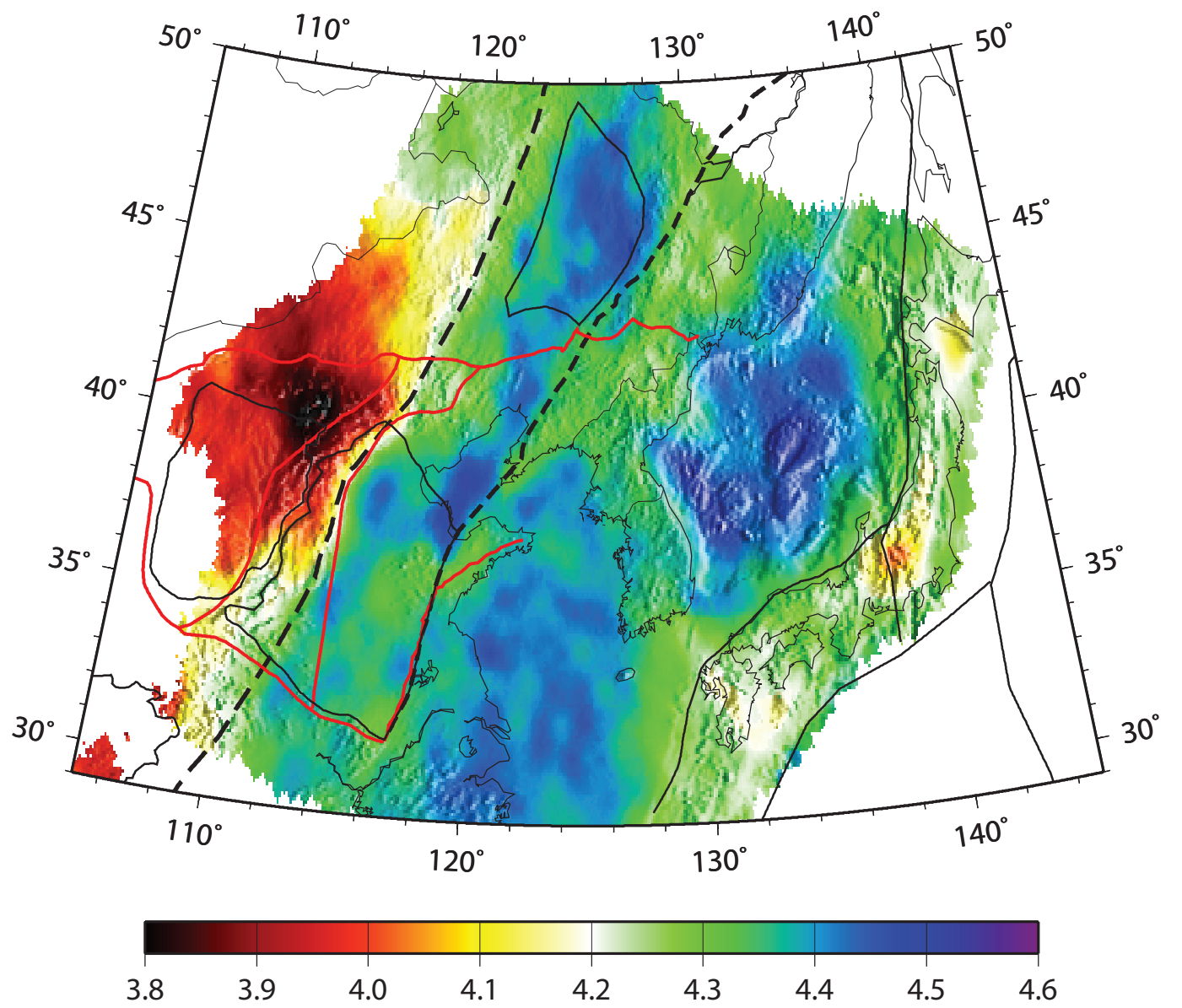




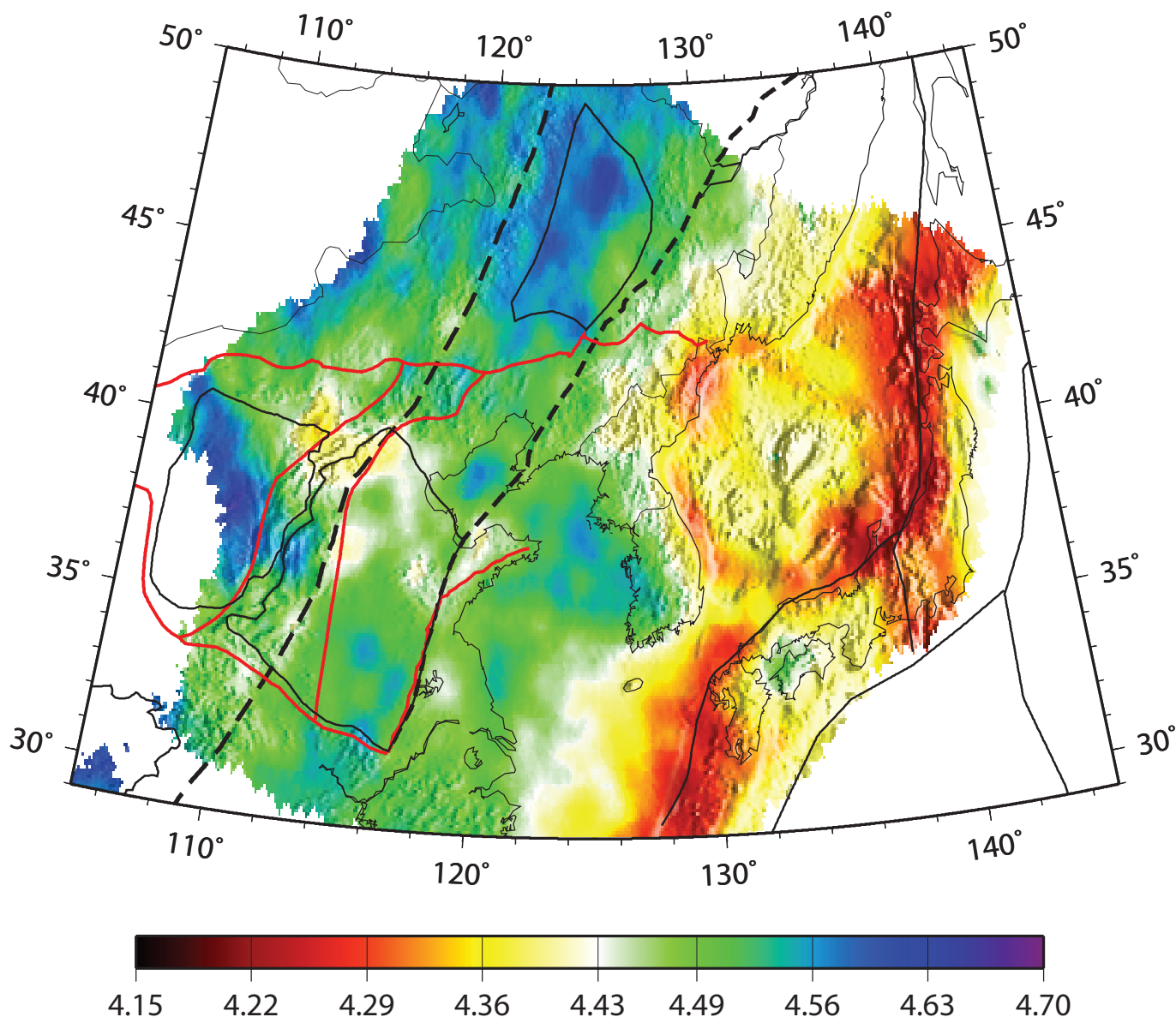
(a) Lower Crust



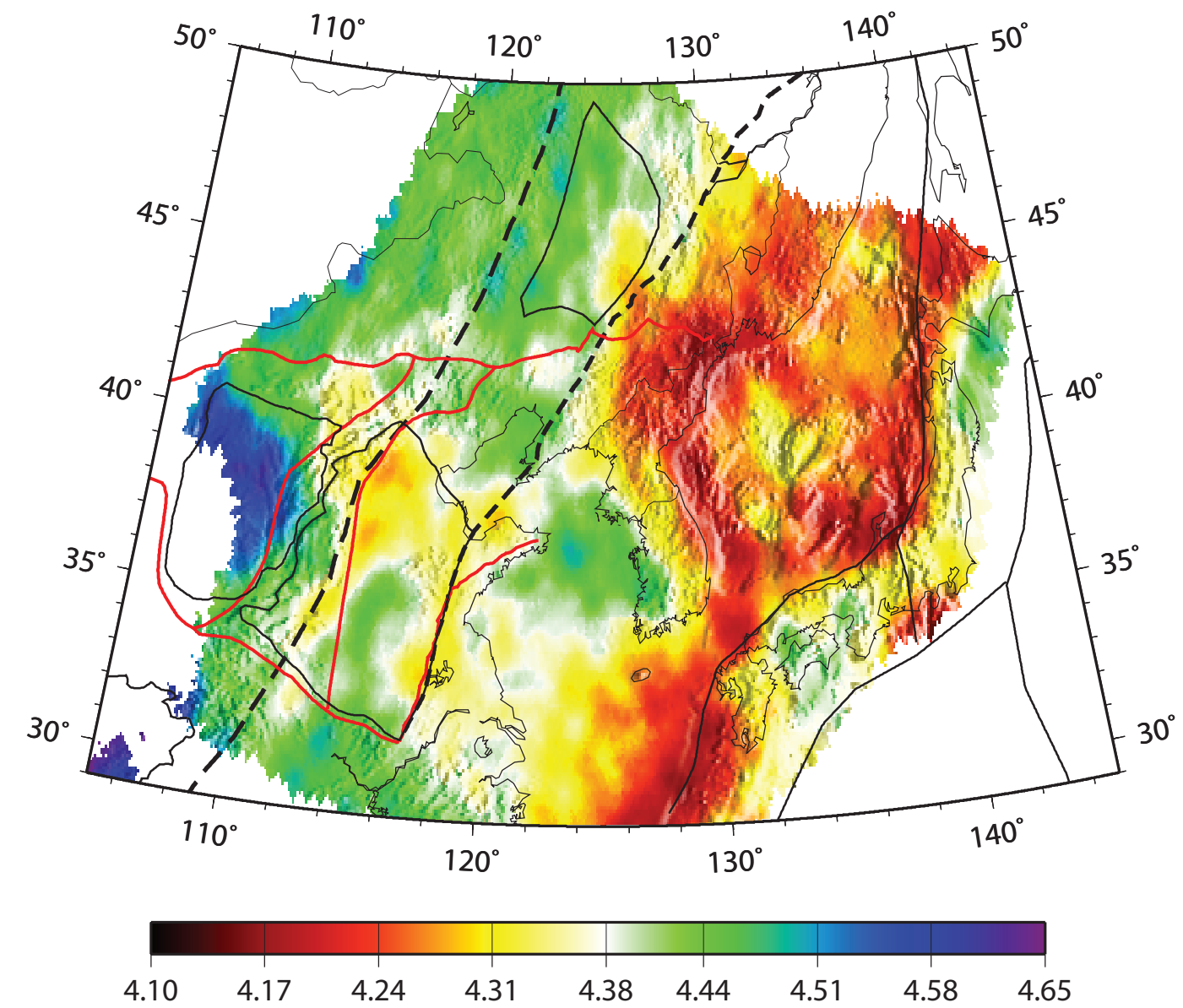
(b) Depth = 40 km

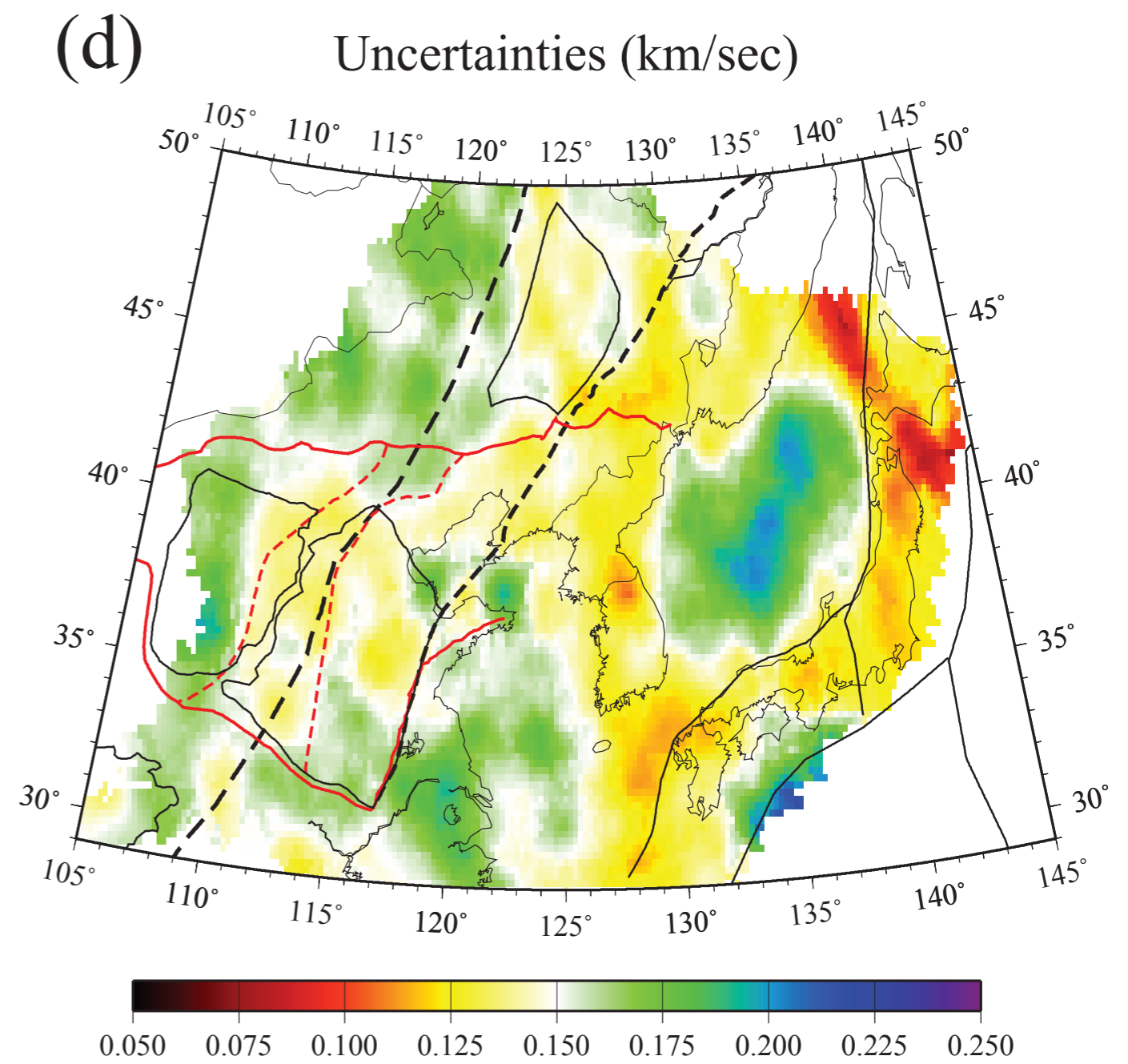
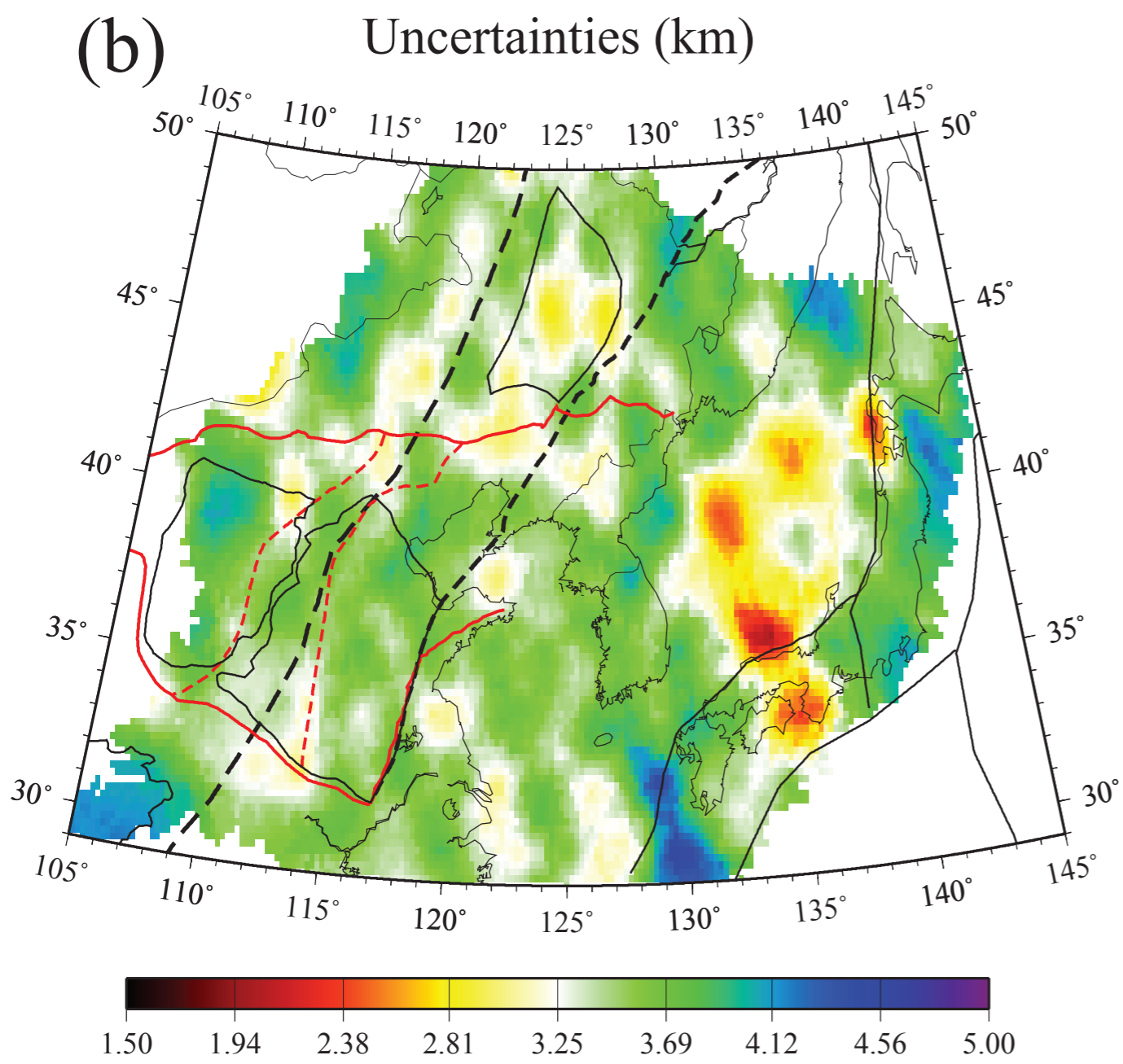
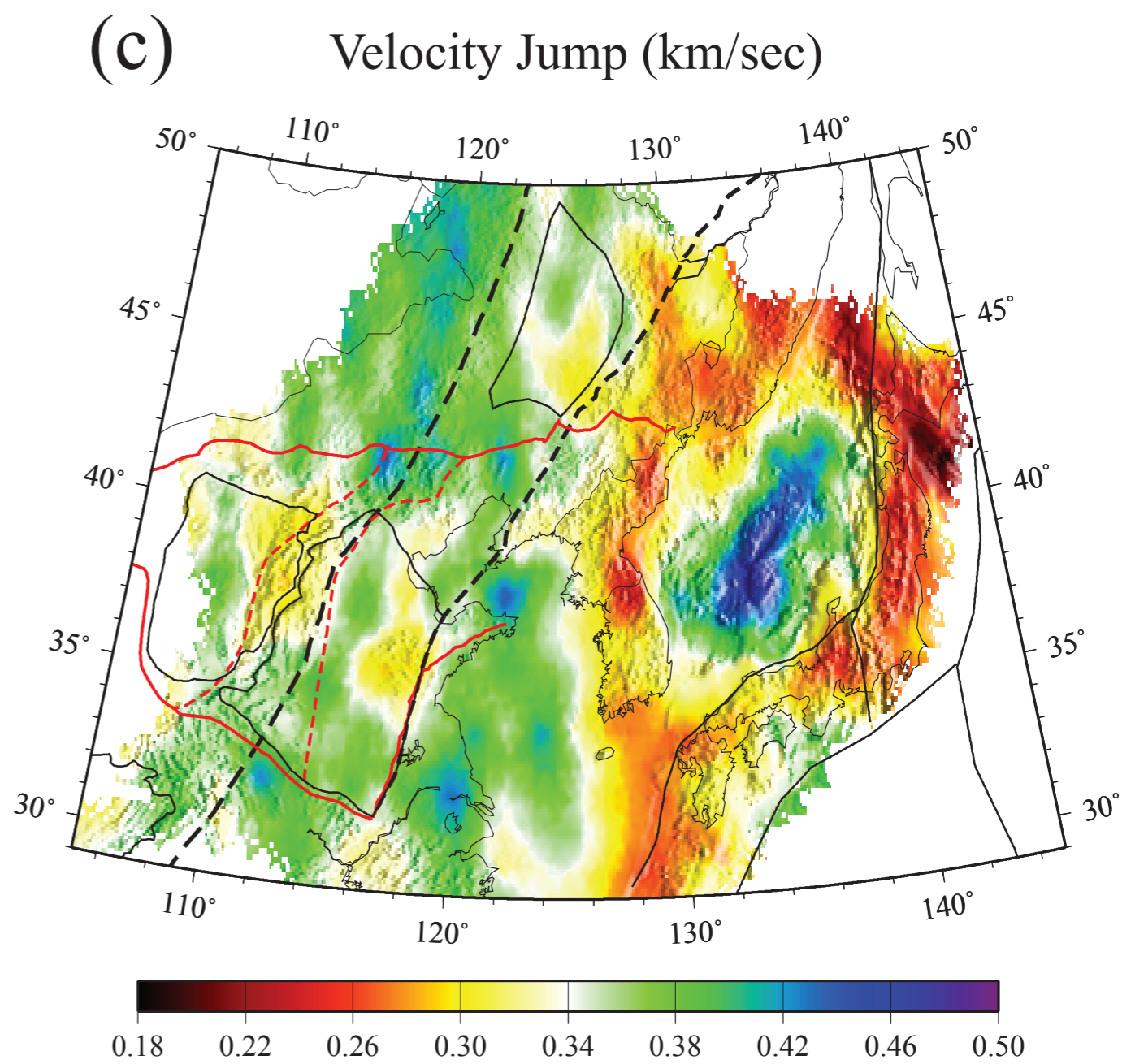
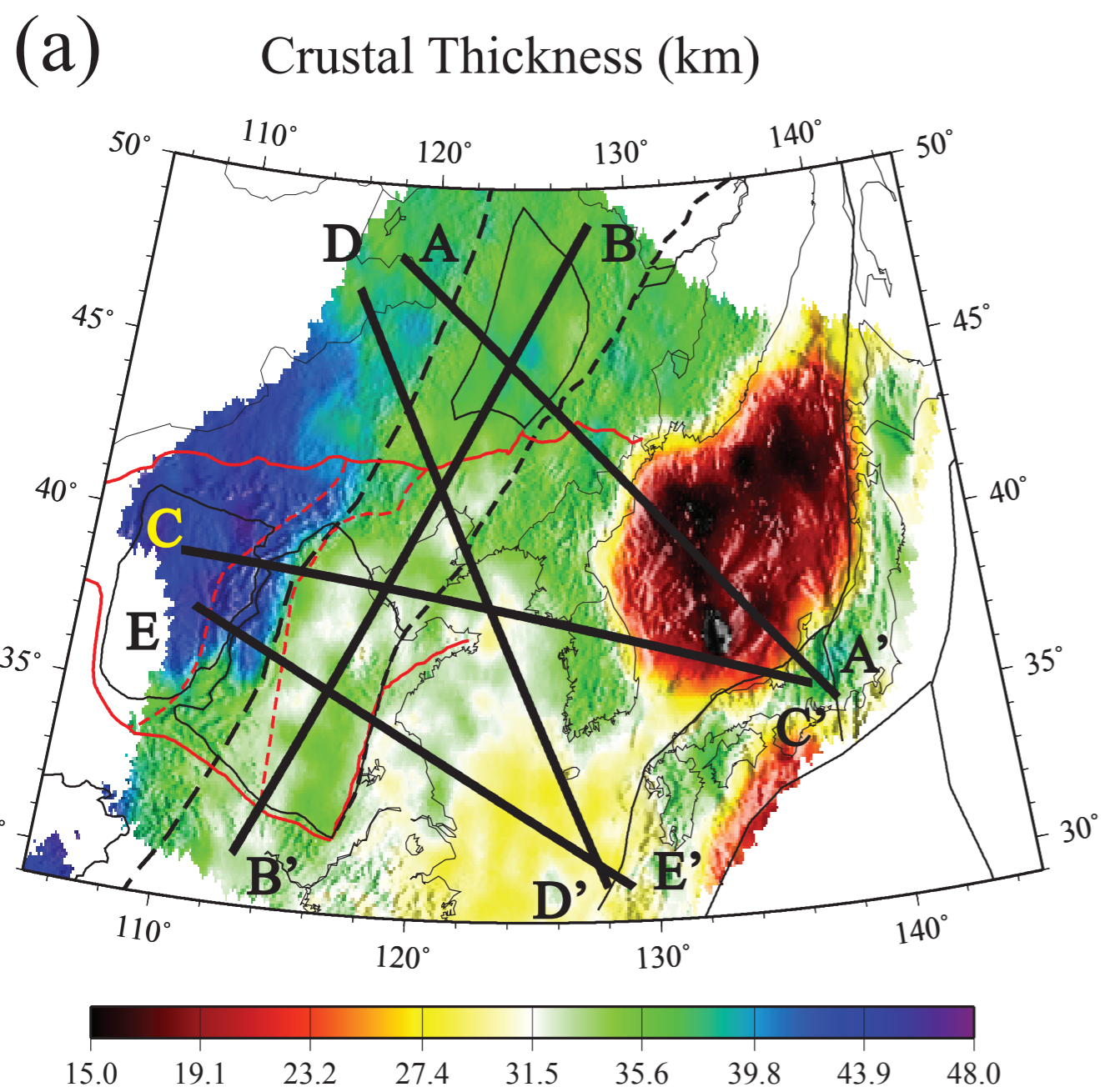


(c) Depth = 60 km

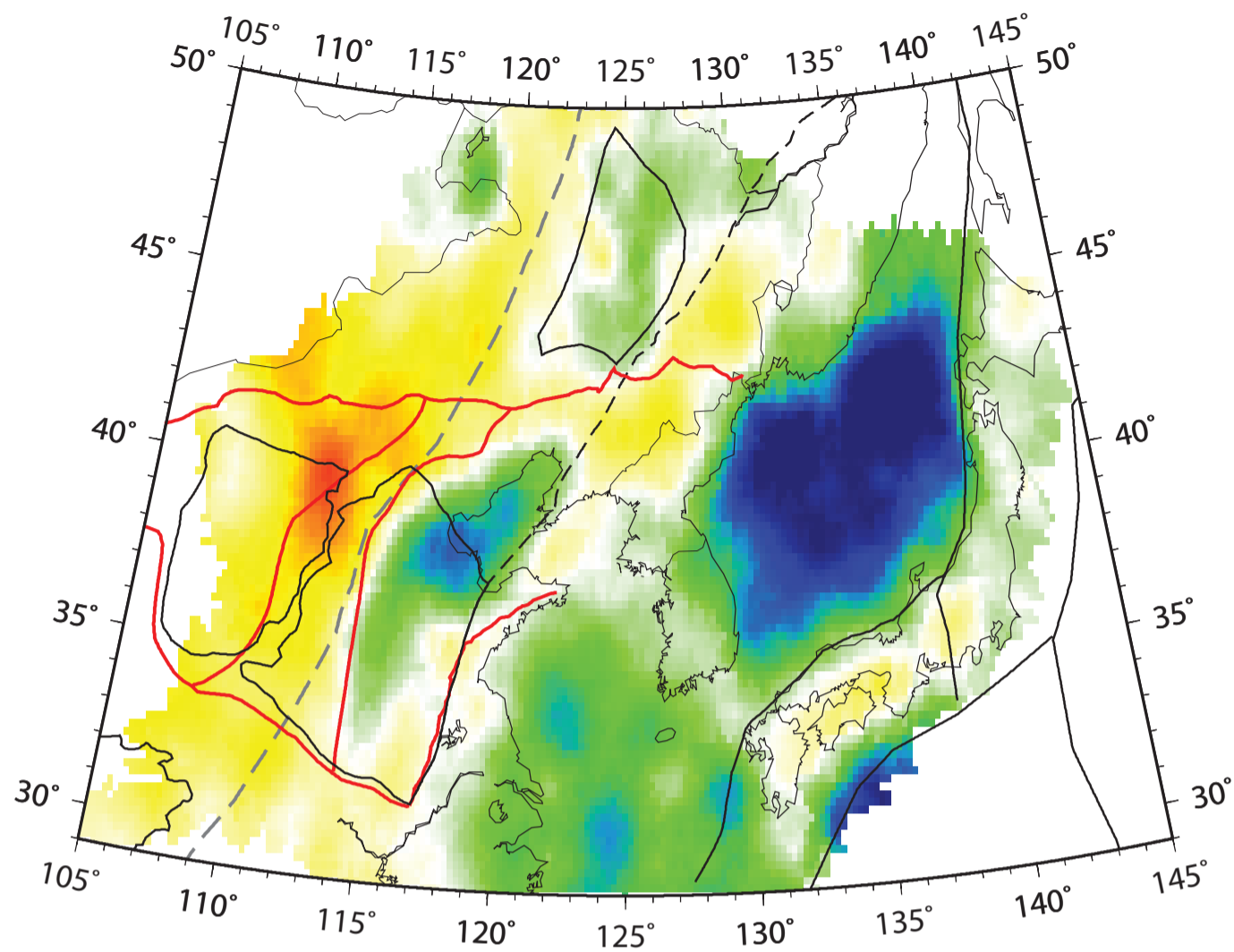


(d) Depth = 80 km

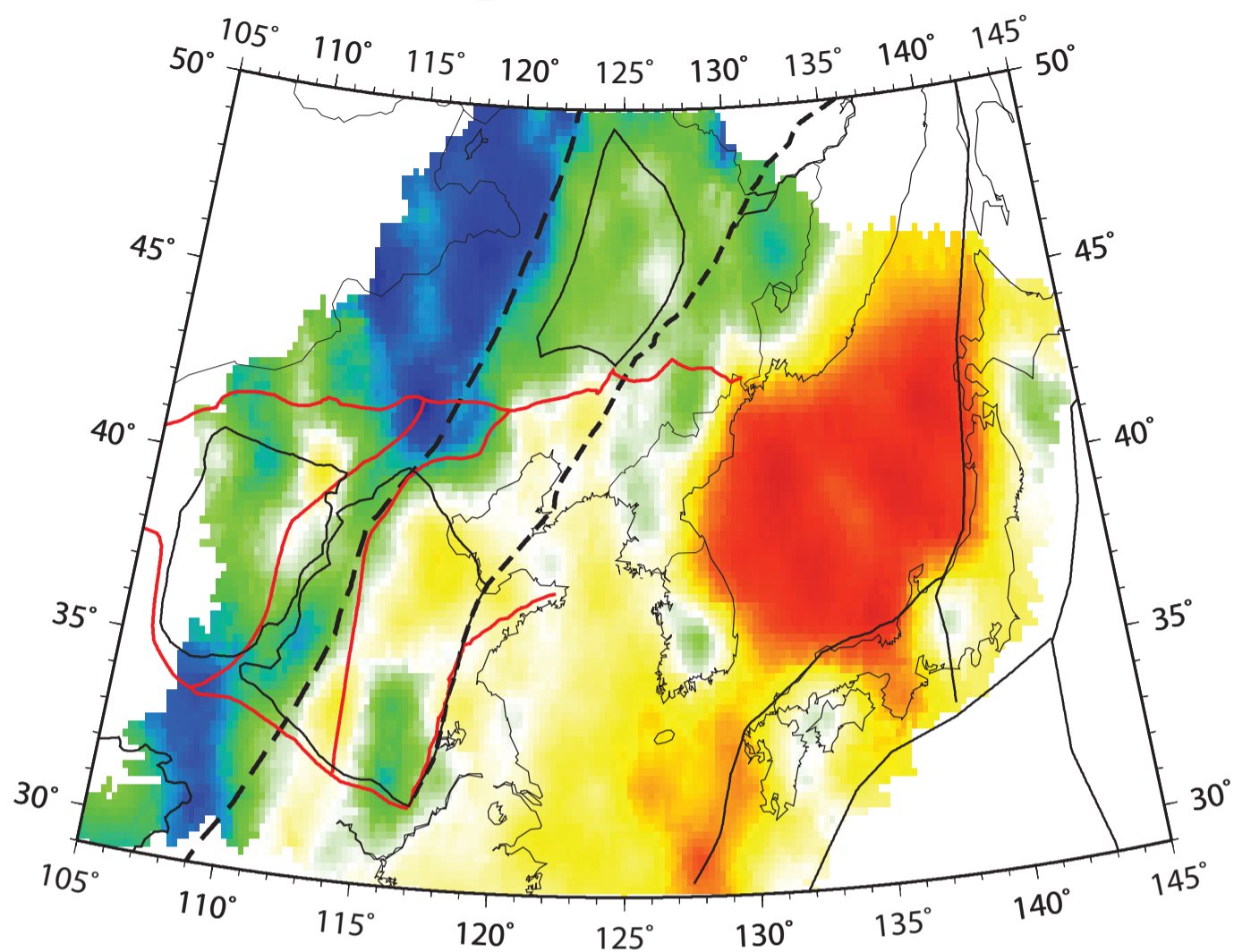




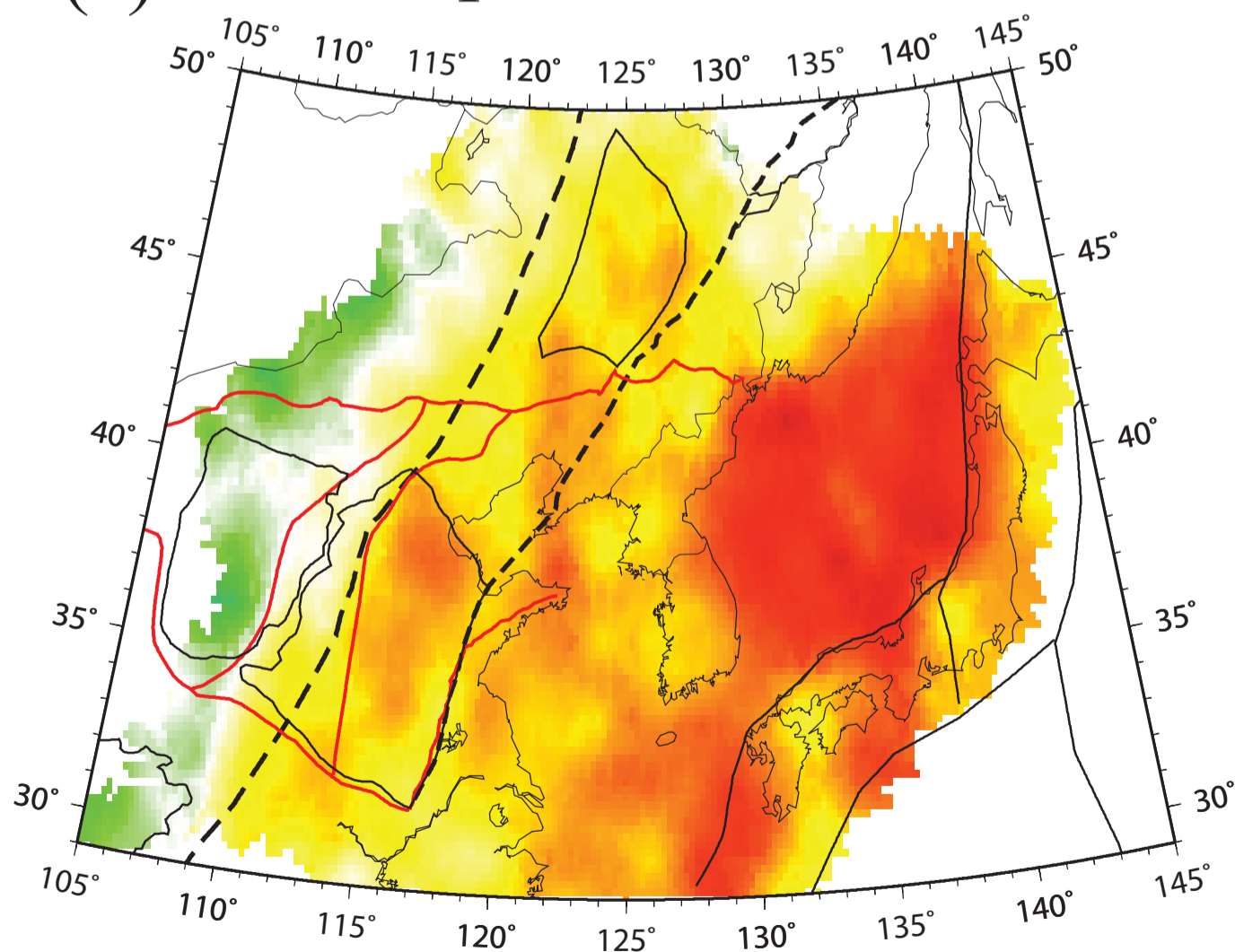
(a) Lower Crust



(b) Depth = 40km



(c) Depth = 60km



(d) Depth = 80km

